University of Regensburg

Spin Effects in High- and Low-Field Magnetotransport Experiments in Semimagnetic $Cd_{1-x}Mn_xTe$ Heterostructures

Dissertation
zur Erlangung des Doktorgrades der Naturwissenschaften
(Dr. rer. nat.)
der Fakultät für Physik
der Universität Regensburg

presented by Christian Betthausen, born in Munich
Regensburg, May 2012

Promotionsgesuch eingereicht am: 07.05.2012
Die Arbeit wurde angeleitet von: Prof. Dr. Dieter Weiss
Datum des Promotionskolloquiums: 09.07.2012

Prüfungsausschuß:

Vorsitzender:	Prof. Dr. John Schliemann
Erstgutachter:	Prof. Dr. Dieter Weiss
Zweitgutachter:	Prof. Dr. Klaus Richter
Weiterer Prüfer:	Prof. Dr. Rupert Huber

Contents

Introduction

Since the early 1960s the quest for faster information processing along with less energy consumption in semiconductor electronics has mainly been achieved by increasing the number of transistors per integrated circuit. However, with transistors becoming smaller and smaller - channel lengths are 32 nm at the moment - quantum effects and issues in heat dissipation are about to limit the ongoing miniaturization in the near future. In order to overcome these limitations entirely new concepts are required, as for instance the utilization of the electron's spin as an additional degree of freedom. Major advantages of these *spin-based* electronics devices over conventional charge-based ones would be faster switching times and lower power consumption.
The research field of spin-based electronics (spintronics) has already been triggered in 1988 by the discovery of the giant magnetoresistance effect by P. Grünberg and A. Fert, which since about the year 2000 is commercially applied in hard disk drive read heads. Though, the realization of other spintronics concepts such as the Datta-Das spin transistor (spin FET) - proposed theoretically in 1990 - remains challenging, mainly due to the following reasons: First, spin information is extremely volatile and is lost easily due to relaxation and dephasing processes within the semiconductor. This leads to attenuated signals in current spin transistor prototypes. Second, a nearly 100% spin polarization is needed for proper device operation - a situation quite hardly to achieve via common spin injection from a ferromagnet into the semiconductor due to the conductivity mismatch at the material interface.
An integral part of spintronics is the research on diluted magnetic semiconductors (DMSs), i.e. materials that incorporate magnetism by doping the semiconductor crystal with e.g. manganese ions. These substances - also referred to as semimagnetic semiconductors - can fully be integrated in standard electronic devices and allow one to overcome the conductivity mismatch problem: As they are either ferro- or paramagnetic they give rise to an intrinsic spin polarization, at least in the presence of a tiny external magnetic field. This gives hope to achieve much larger spin polarizations in future spin FET prototypes. Paramagnetic DMSs based on II-VI compounds (e.g. HgMnTe, CdMnTe, ZnMnSe) have been studied for more than 30 years, but only the successful growth of the ferromagnetic III-V compound GaMnAs by H. Ohno in 1996 has lead to an increased interest in this material class. Two-dimensional electron or hole systems formed in these semimagnetic semiconductors allow to further study the interplay between mobile

charge carriers and localized magnetic moments associated with the incorporated manganese ions (*sp-d* exchange interaction).

In order to gain a deeper insight into the characteristics of DMS systems this thesis addresses the magnetotransport properties of n-type doped $Cd_{1-x}Mn_xTe$ quantum well devices. Here, *s-d* exchange interaction gives rise to the *giant Zeeman splitting* of electronic states which in addition is in a nonlinear fashion dependent on magnetic field.
The central goal is to probe for consequences of this exchange-enhanced spin splitting on two different transport regimes in $Cd_{1-x}Mn_xTe$: On the one hand we study its impact on the fractional Quantum Hall effect (FQHE) that we demonstrated to also emerge in a DMS alloy. On the other hand we focus on the effect of *s-d* exchange on adiabatic spin transport and the control of spin backscattering in the limit of low magnetic fields.
Due to the recent significant increase in the quality of CdTe-based two-dimensional electron systems we were able to report the observation of the FQHE in yet another material system, namely in a II-VI compound semiconductor. In this context the emergence of fractional fillings in CdTe is less fundamental than their presence in the semimagnetic alloy $Cd_{1-x}Mn_xTe$, constituting the very first demonstration of the FQHE in a DMS. Our experiments hence prove that the presence of magnetic impurities in a semiconductor quantum structure does not inhibit the formation of FQH states. A simple extension of the Composite Fermion (CF) model allows us to explain the measured angular dependency of activation energy gaps at fractional fillings. Our data suggest that CFs are - similar to the case of electrons in a DMS - subject to *s-d* exchange interaction.
The control of spin backscattering, i.e. the possibility to switch between spin transmission and spin blocking in a semiconducting channel, constitutes one prerequisite for the realization of a spin transistor. We present here a novel approach to achieve spin transistor action based on a $Cd_{1-x}Mn_xTe$ quantum well structure. The essential part of our device is a grating of pre-magnetized ferromagnetic stripes on its top. This generates a helical stray field that is translated into a helical pattern of (significant) spin polarization via the giant Zeeman splitting. We show that in this setup spin information is protected against decay as spins are transported *adiabatically* from source to drain while forming the above mentioned helical spin polarization pattern. The implementation of loss-free spin information propagation has so far been an obstacle to the successful realization of spin transistor prototypes and is one of the major achievements of our approach. Transistor operation is attained by inducing tunable Landau-Zener transitions via an external magnetic field which lead to spin backscattering and consequently allow to modulate the channel conductance. In contrast to the design suggested by Datta and Das, our proof of concept device is exceptionally tolerant against disorder and gives rise to efficient spin transport over device distances of 50 μm.

1 Material Properties of CdTe and CdMnTe

Partially substituting the cations of a semiconductor host lattice by magnetic ions - such as manganese - results in the formation of a diluted magnetic semiconductor (DMS), also referred to as a semimagnetic semiconductor (SMS). Quantum structures derived from this new material system allow to study the interplay between quantum electronics and thin film magnetism, hence giving direct access to the electronic spin degree of freedom. This may be exploited in magneto-optical as well as magnetotransport experiments - the latter to be conducted within the framework of this PhD thesis.
Semimagnetic semiconductors are generally characterized by a large spin splitting due to exchange interaction between mobile carriers and localized magnetic moments; the latter brought about by the incorporated magnetic impurities. This so called *sp-d* exchange interaction and its impact on magnetotransport will be discussed in detail in chapter 2.3. The samples under investigation are quantum structures based on the II-VI compound semiconductors CdTe and $Cd_{1-x}Mn_xTe$ (commonly abbreviated to CdMnTe). Thus a review of some of their basic physical properties will be given in the introductory sections. A much more detailed survey on this topic may be found in references [1–4] with the following chapter being partially geared to reference [1].

1.1 Crystal Structure

The most extensively and thoroughly investigated II-VI DMSs are $A^{II}_{1-x}Mn_xB^{VI}$ alloys in which a fraction of the group II sublattice is randomly occupied by manganese ions. Besides $Cd_{1-x}Mn_xTe$, ternary compounds like $Hg_{1-x}Mn_xTe$ or $Zn_{1-x}Mn_xTe$ are part of this material family which completely is listed in table 1.1 along with crystal structures and corresponding ranges of composition.
$Cd_{1-x}Mn_xTe$ crystallizes in zinc-blende structure (see fig. 1.1) which can be viewed as two interpenetrating fcc sublattices, each occupied either by anion or cation atoms, respectively[1]. The anionic component of a $Cd_{1-x}Mn_xTe$ crystal

[1] Alternatively the zinc-blende structure may be considered as a fcc lattice with two basal atoms, situated relative to each lattice point at (0,0,0) and $a/4(1,1,1)$. Here, a denotes the lattice constant.

Table 1.1: Family of $A^{II}_{1-x}Mn_xB^{VI}$ type diluted magnetic semiconductors. Taken from ref. [1].

material	crystal structure	range of composition
$Zn_{1-x}Mn_xS$	zinc-blende	$0 < x \leq 0.10$
	wurzite	$0.10 < x \leq 0.45$
$Zn_{1-x}Mn_xSe$	zinc-blende	$0 < x \leq 0.30$
	wurzite	$0.30 < x \leq 0.57$
$Zn_{1-x}Mn_xTe$	zinc-blende	$0 < x \leq 0.86$
$Cd_{1-x}Mn_xS$	wurzite	$0 < x \leq 0.45$
$Cd_{1-x}Mn_xSe$	wurzite	$0 < x \leq 0.50$
$Cd_{1-x}Mn_xTe$	zinc-blende	$0 < x \leq 0.77$
$Hg_{1-x}Mn_xS$	zinc-blende	$0 < x \leq 0.37$
$Hg_{1-x}Mn_xSe$	zinc-blende	$0 < x \leq 0.38$
$Hg_{1-x}Mn_xTe$	zinc-blende	$0 < x \leq 0.75$

is the tellurium atoms whereas cadmium or manganese represent the cationic counterparts. Given the fact that MnTe naturally crystallizes in NiAs structure[2] it is remarkable to come across zinc-blende $Cd_{1-x}Mn_xTe$ alloys with manganese concentrations x of up to 77%. Higher values typically result in an inhomogeneous alloy due to the onset of MnTe cluster formation. Generally speaking, the formation of ternary alloys by substituting Mn for the group II element in a $A^{II}B^{VI}$ lattice retains the crystal structure of the parent compound - at least up to a certain composition.

Besides manganese, other transition metals such as chromium, iron or cobalt may be introduced into the CdTe host lattice as well; none of them however being as miscible with the II-VI compound as manganese. This behavior originates from the manganese atom's exactly half-filled $3d$ shell: By Hund's rule all five spins in this orbital are aligned parallel, requiring about 7 eV to add an electron with opposite spin. Hence the $3d^5$ orbital may be regarded to nearly act as a complete shell (similar to the $4d^{10}$ orbital in Cd) for which reason a manganese atom is more likely to resemble the behavior of a group II element compared to other transition metals. It consequently can much easier occupy a Cd lattice site.

The lattice parameters of all $A^{II}B^{VI}$ alloys are excellently described by *Vegard's law*. It predicts a linear variation of the lattice constant with manganese concentration:

$$a = (1 - x)\, a_{\mathrm{II-VI}} + x\, a_{\mathrm{Mn-VI}}, \tag{1.1}$$

where $a_{\mathrm{II-VI}}$ and $a_{\mathrm{Mn-VI}}$ are the lattice parameters of the binary constituents which need to be of the same crystal structure as the alloy formed. The lattice constant of $Cd_{1-x}Mn_xTe$ thus is expected to have the following form (for parameters refer

[2] The NiAs structure can be viewed as a hcp anion sublattice with cation atoms in the octahedral interstices.

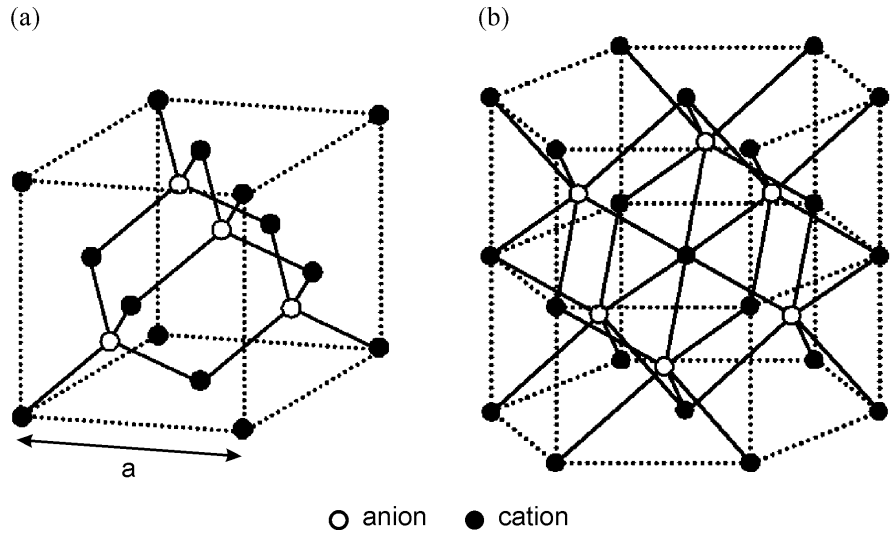

Figure 1.1: Unit cells of (a) zinc-blende and (b) NiAs structure. The lattice constant of the zinc-blende unit cell is denoted by *a*. Adjusted from ref. [5].

to table 1.2 in the next section):

$$a_{\mathrm{CdMnTe}} = (0.648 - 0.015\,x)\,\mathrm{nm}, \quad x < 0.77. \tag{1.2}$$

Fig. 1.2 depicts the above described dependence of the lattice parameter on composition for selected DMSs; an extrapolation to $x = 1$ yields the (same) lattice constant for 'hypothetical' zinc-blende MnTe. The term 'hypothetical' used in this context has historical reasons: As MnTe naturally crystallizes in the NiAs structure it took until the invention of molecular beam epitaxy to grow zinc-blende MnTe on a GaAs substrate. Contrary to predictions, zinc-blende MnTe could be grown to thicknesses of up to 8 μm thus proving not to turn to its natural NiAs form after exceeding a critical thickness.

1.2 Band Structure in Absence of a Magnetic Field

When no external magnetic field is present, the family of the $\mathrm{A}^{\mathrm{II}}_{1-x}\mathrm{Mn}_x\mathrm{B}^{\mathrm{VI}}$ alloys shares many common band structure features. Those can be summarized as follows:

- Like their parent $\mathrm{A}^{\mathrm{II}}\mathrm{B}^{\mathrm{VI}}$ compounds all $\mathrm{A}^{\mathrm{II}}_{1-x}\mathrm{Mn}_x\mathrm{B}^{\mathrm{VI}}$ ternaries are direct-gap semiconductors. Generally speaking, their band structure closely resembles that of the $\mathrm{A}^{\mathrm{II}}\mathrm{B}^{\mathrm{VI}}$ materials as displayed in fig. 1.3a using the example of CdTe.
- To a first approximation the band gap E_g is linearly dependent on manganese content x:

$$E_g(x) = (1 - x)\,E_g(0) + x\,E_g(1), \tag{1.3}$$

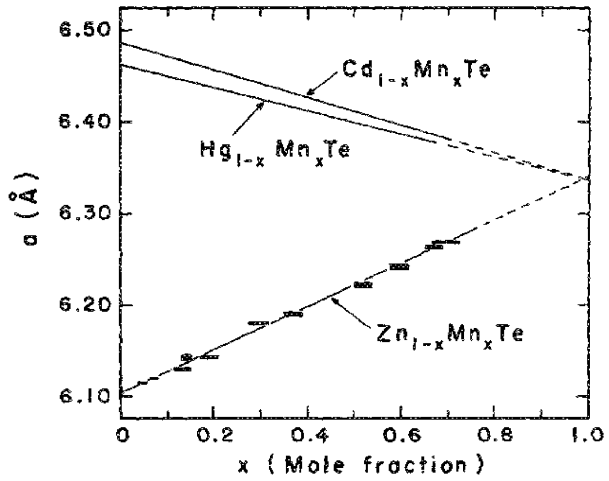

Figure 1.2: Lattice constant a as a function of manganese concentration x for telluride DMSs. The close accordance with Vegard's law additionally is reflected in the convergence of the extrapolated lines at a single point, namely the lattice constant of MnTe (6.33 Å). Taken from ref. [1].

where $E_g(0)$ and $E_g(1)$ are the energy gaps for $x = 0$ and $x = 1$, respectively.

- In the case of zero external magnetic field the electronic systems of manganese $3d^5$ shell and $A^{II}B^{VI}$ energy bands[3] may be considered independently. This is illustrated by fig. 1.3b where the presence of manganese is introduced as two energy levels superimposed on the $A^{II}B^{VI}$ band structure. Those levels marked $e_d^{+\sigma}$ and $e_d^{-\sigma}$ correspond to the occupied and unoccupied states of the Mn $3d$ orbital and are separated by an energy $U_{\text{eff}} \approx 7$ eV. In a real DMS each level will be further split by the crystal field and slightly broadened due to hybridization with the p bands (p-d hybridization).

By utilizing equation 1.3 and the data given in table 1.2 the variation of the $Cd_{1-x}Mn_xTe$ energy gap can be expressed as

$$E_g(4.2\,\text{K}) = (1.606 + 1.592\,x)\,\text{eV}. \tag{1.4}$$

The above equation applies to the allowed composition range $0 \leq x \leq 0.77$ but may be extrapolated to $x = 1$ thus yielding the energy gap for zinc-blende MnTe (see fig. 1.4).
Incorporating manganese into a $A^{II}B^{VI}$ host lattice results in a drastic modification of the optical properties of the formed ternary alloy. Those are dominated by intra-ion transitions involving a spin-flip within the half-filled manganese $3d$ orbital. According to Hund's rule the spins of the five d shell electrons are aligned parallel in the ground state, e.g. ($\uparrow\uparrow\uparrow\uparrow\uparrow$). Photons with energies higher than 2.2 eV

[3]The energy bands originate from the s and p orbitals of the constituent atoms and are referred to as sp bands.

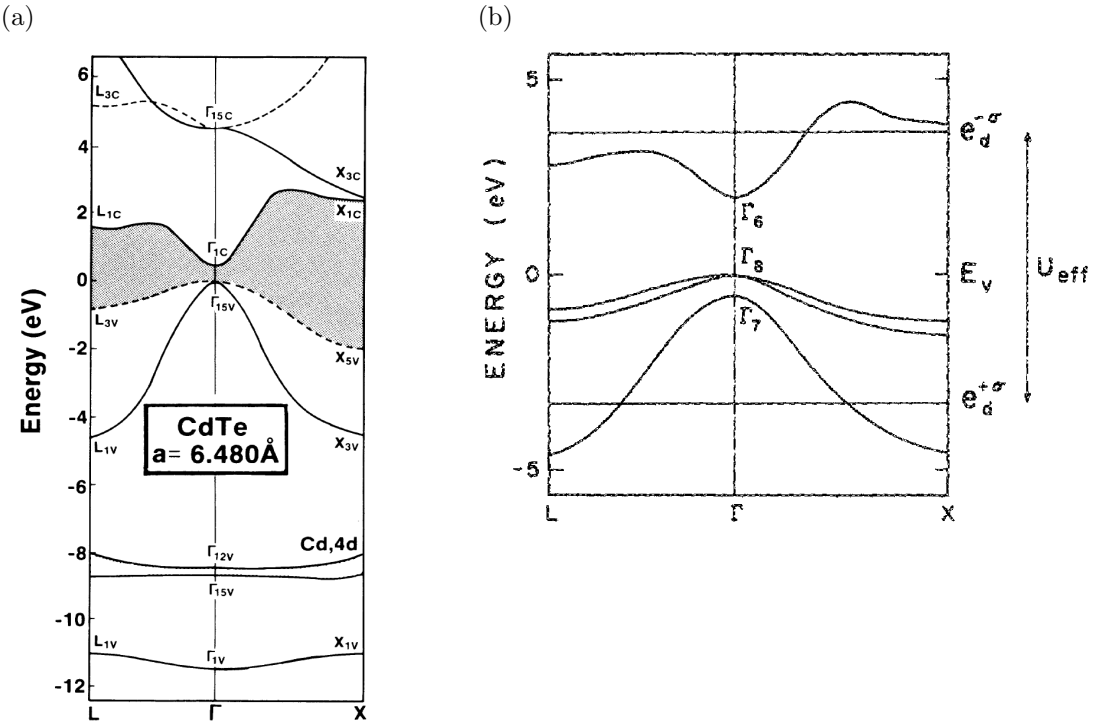

Figure 1.3: (a) Relativistic band structure of CdTe. The band gap region is shaded, dashed lines indicate doubly degenerate states. From ref. [6]. (b) Schematic band structure of a zinc-blende $A^{II}_{1-x}Mn_xB^{VI}$ alloy. In the absence of a magnetic field the Mn levels $e_d^{+\sigma}$ (occupied) and $e_d^{-\sigma}$ (unoccupied) are regarded as superimposed on the bandstructure. They are separated by an energy $U_{\text{eff}} \approx 7$ eV. Effects of p-d hybridization and crystal field splitting are neglected as they would only give small corrections on the scale of the figure. Source: Ref. [1].

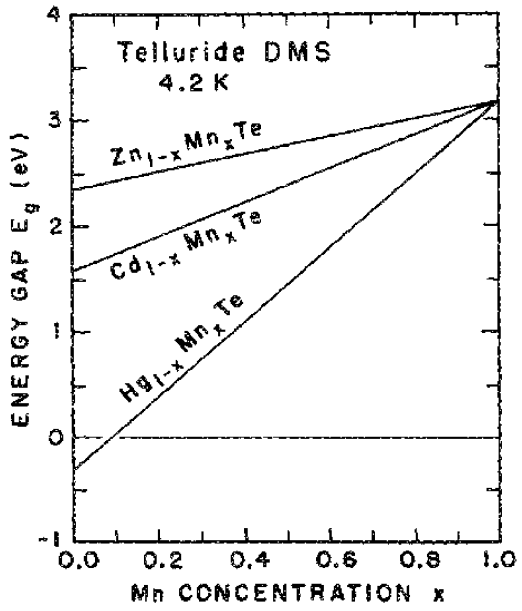

Figure 1.4: Dependence of energy gap E_g on Mn concentration x for telluride DMSs at 4.2 K. A linear extrapolation to $x = 1$ yields a value of 3.2 eV for the energy gap of zinc-blende MnTe. Taken from ref. [1].

Table 1.2: Lattice constant and band gap E_g of selected telluride compound semiconductors. Source: References [1, 7, 8].

material	lattice constant (nm)	E_g(300 K) (eV)	E_g(4.2 K) (eV)
CdTe	0.6480	1.528	1.606
$Cd_{1-x}Mn_xTe$	$0.6480 - 0.015\,x$	$1.528 + 1.316\,x$	$1.606 + 1.592\,x$
$Cd_{1-x}Mg_xTe$	$0.6480 - 0.0045\,x$	$1.528 + 1.672\,x$	$1.606 + 1.884\,x$
MnTe	0.633	2.9	3.2
MgTe	0.6435	3.2	3.49

can induce a spin-flip of type ($\uparrow\uparrow\uparrow\uparrow\downarrow$), constituting a very effective absorption mechanism; it is observed in all optical experiments on crystals with a manganese concentration exceeding 10%. In principle, intra-shell spin-flips are forbidden by selection rules but these are relaxed by spin-orbit interaction when the Mn-ion is placed into the $A^{II}B^{VI}$ crystal lattice.
In the presence of a finite magnetic field the systems of localized manganese *d* electrons and *sp* bands can no longer be considered independently. Furthermore, the so called *sp-d* exchange interaction arises having profound impact on magneto-optical and magnetotransport experiments. Details are discussed in chapter 2.3.

1.3 Magnetic Properties

The magnetic properties of CdMnTe and in general of all $A^{II}_{1-x}Mn_xB^{VI}$ alloys are governed by exchange interaction between Mn^{2+} ions. Theoretical calculations [9] reveal the so called *superexchange* mechanism to be the most dominant process, with nearest-neighbors as well as next-nearest-neighbors interacting antiferromagnetically.
Superexchange is an indirect coupling between two cations (here Mn^{2+}) mediated by a non-magnetic anion (Te^{2-} in the case of CdMnTe). Dependent on symmetry and occupancy of the overlapping ionic orbitals this interaction is found to be either ferromagnetic or antiferromagnetic. In the case of $A^{II}_{1-x}Mn_xB^{VI}$ alloys both magnetic ions exhibit half-filled orbitals and the Pauli Exclusion Principle consequently forces them to couple antiferromagnetically. II-VI DMSs exhibit nearest-neighbor Mn-Mn exchange integrals J ranging from -10 K to -20 K. For example, $J_{\mathrm{CdMnTe}} = -6.9$ K [10].
Dependent on temperature and manganese content, $A^{II}_{1-x}Mn_xB^{VI}$ alloys exist in different magnetic phases: a high-temperature paramagnetic phase and a low-temperature frozen phase. Fig. 1.5 displays the magnetic phase diagram of CdMnTe which is qualitatively characteristic of all II-VI DMSs. Upon in-

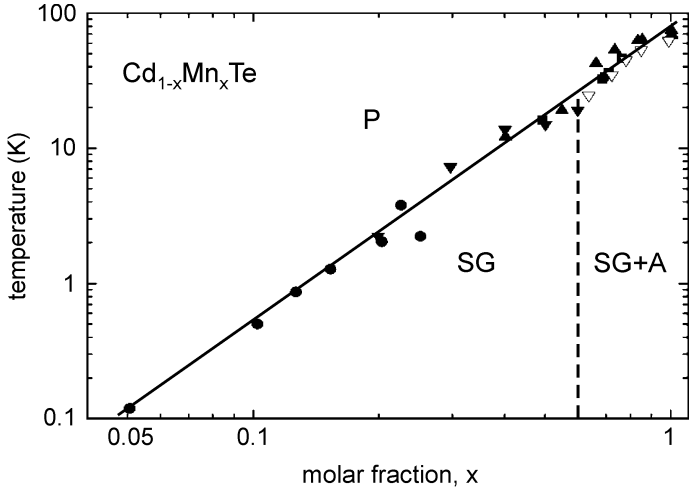

Figure 1.5: Magnetic phase diagram of CdMnTe in double logarithmic scale. Depending on temperature and Mn concentration x either the paramagnetic (P), spin-glass like (SG) or antiferromagnetic (A) phase exists. Adjusted from ref. [11].

creasing the manganese concentration x one finds a continuous transition from paramagnetic to spin-glass like ($x \geq 0.05$) and finally to antiferromagnetic ordering ($x > 0.6$). The latter phase however exhibits only a certain fraction of the magnetic ions being well ordered (e.g. $\approx 50\%$ for $Cd_{0.35}Mn_{0.65}Te$), the rest still remaining in a disordered spin-glass like phase [11].
Since the CdMnTe QW structures investigated within the framework of this PhD thesis exhibit Mn concentrations lower than 1.5%, only the *paramagnetic phase* shall be discussed in the following. In the dilute limit, when $x < 0.01$ holds, the Mn spins can be considered as isolated, i.e. independent from each other. In this case the magnetization M is given by [1]

$$M = xN_0 g\mu_B S\mathcal{B}_S\left(\frac{g\mu_B SB}{k_B T}\right), \tag{1.5}$$

where N_0 denotes the number of cations per unit volume, T the temperature, B the applied magnetic field, μ_B Bohr's magneton and k_B Boltzmann's constant. Due to the nature of the Mn ions, $S = \frac{5}{2}$ and $g = 2$. $\mathcal{B}_S$ is the standard Brillouin function which is defined by:

$$\mathcal{B}_S(\tilde{x}) = \frac{2S+1}{2S}\coth\left(\frac{2S+1}{2S}\tilde{x}\right) - \frac{1}{2S}\coth\left(\frac{1}{2S}\tilde{x}\right). \tag{1.6}$$

In the low-field or high-temperature limit ($g\mu_B SB/k_B T \ll 1$) M is linear in B and the magnetic susceptibility $\chi = \mathrm{d}M/\mathrm{d}B$ is of the Curie form

$$\chi = \frac{C_0 x}{T}, \tag{1.7}$$

with

$$C_0 = N_0(g\mu_B)^2 \frac{S(S+1)}{3k_B}. \tag{1.8}$$

Due to the onset of exchange interaction between Mn ions the magnetization M is reduced at higher values of x and can no longer be expressed by the standard Brillouin function. In order to still be able to describe experimental data, Gaj and coworkers [12] proposed an empirical expression by introducing an effective Mn concentration x_{eff} and temperature T_{eff} to equation 1.5:

$$M = x_{\mathit{eff}} N_0 g\mu_B S\mathcal{B}_S \left(\frac{g\mu_B SB}{k_B T_{\mathit{eff}}}\right). \tag{1.9}$$

Equation 1.7 is modified accordingly.
The above parameters take the antiferromagnetic superexchange interaction between Mn spins into account and satisfy the following relations: $x_{\mathit{eff}} < x$, $T_{\mathit{eff}} > T$. At temperatures of typically below 10 K the effective concentration of isolated free spins x_{eff} is smaller than the concentration of Mn ions x since nearest-neighbor Mn pairs are blocked antiparallel due to their strong antiferromagnetic interaction [13]. Only isolated spins which are not involved in nearest-neighbor pairs contribute to x_{eff} and thus to the magnetization M. The temperature T_{eff} on the other hand accounts for the residual antiferromagnetic exchange interaction between more distant isolated spins.
The effective parameters are either determined by fitting experimental data or via empirical equations. According to Gaj *et al.* [14] T_{eff} can be deduced from the Mn concentration x by:

$$T_{\mathit{eff}} = T + \frac{fE_x}{1+gE_x}, \quad \text{with} \quad E_x[\text{meV}] = 1563\,x. \tag{1.10}$$

Here, $f = 0.02263$ and $g = 0.001761$.
Various ways to estimate x_{eff} from the manganese ion concentration x are given in literature [13, 15]. Equations 1.11 and 1.12 yield very similar results and define an upper bound of x_{eff}, whereas equation 1.13 gives its lower limit value (see fig. 1.6):

$$x_{\mathit{eff}} = x\left(0.26\,\mathrm{e}^{-43.3x} + 0.73\,\mathrm{e}^{-6.2x} + 0.01\right) \tag{1.11}$$

$$x_{\mathit{eff}} = x\left(P_1 + \frac{P_3}{3} + \frac{P_4}{15} + \frac{1-P_1-P_2-P_3-P_4}{5}\right) \tag{1.12}$$

$$x_{\mathit{eff}} = x\left(P_1 + \frac{P_3}{3} + \frac{P_4}{15}\right), \tag{1.13}$$

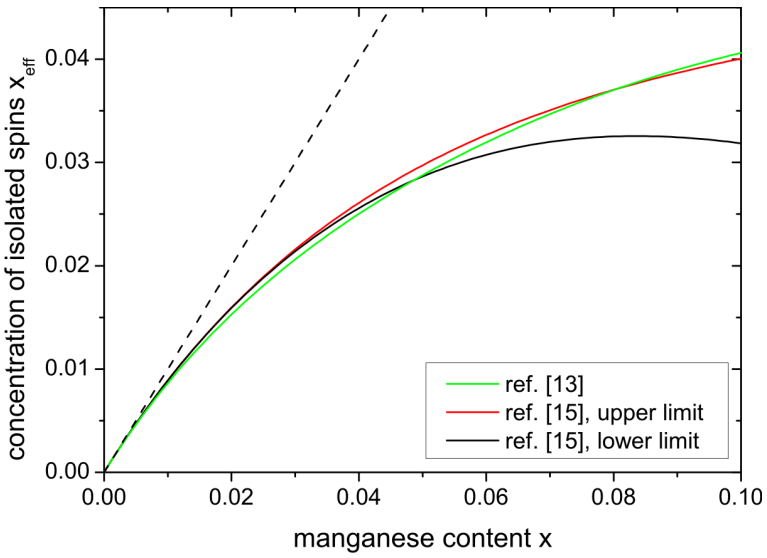

Figure 1.6: Comparison of various estimates of the concentration of isolated spins x_{eff} in II-VI DMSs as given by equations 1.11, 1.12 and 1.13, respectively. Due to superexchange interaction nearest-neighbor Mn pairs are blocked antiparallel, which reduces their contribution to the magnetization M. The dashed line represents the condition $x_{eff} = x$.

with

$$P_1 = (1-x)^{12} \tag{1.14}$$
$$P_2 = 12x(1-x)^{18} \tag{1.15}$$
$$P_3 = 18x^2(1-x)^{23}(7-5x) \tag{1.16}$$
$$P_4 = 24x^2(1-x)^{22}. \tag{1.17}$$

At least one of the three unknowns (x, x_{eff} or T_{eff}) needs to be extracted from experiments, the others can then be calculated by employing the above equations. For an example refer to section 4.2.1 which elaborates on the determination of x_{eff} from low-field magnetotransport data.

2 Theoretical Background

All experiments performed within the framework of this PhD thesis explore the so far unknown regimes of either the fractional Quantum Hall effect in a semimagnetic semiconductor (chapter 4) or of an artificial spin superstructure affecting low-field electronic transport (chapter 5). In the latter case, the giant Zeeman splitting inherent to the CdMnTe system is utilized to transform the helical stray field of a ferromagnetic stripe grating into a spatially oscillating spin polarization.
To gain a better understanding of the effects investigated, the next sections will introduce selected knowledge of magnetotransport in two dimensions: After briefly reviewing the basics of two-dimensional systems the main focus will be on exchange interaction (giant Zeeman effect) in CdMnTe as well as on the Quantum Hall Effects. Finally, transport in magnetically modulated GaAs structures shall be discussed.

2.1 Charge Carriers in Two Dimensions

Since two-dimensional electron and hole systems (2DES/2DHS) have intensively been investigated during past decades their quality - as may be measured in terms of electron or hole mobility - could steadily be increased. Among all 2D systems, GaAs based structures are by far the most frequently studied ones and feature the highest electron mobilities of up to 30 million cm^2/Vs, reported for a GaAs quantum well [16].
An introduction to basic properties of 2D systems is given in reference [17], a detailed documentation can be found in [18].
The following considerations assume the 2DES/2DHS - also referred to as 2D electron or hole gas (2DEG/2DHG) - to lie in the x-y plane, whereas the growth direction (z direction) is the plane normal.

2.1.1 Implementation

The invention of the silicon MOSFET[1] in the early 1960s marks the beginning of the research on two-dimensional structures. Upon applying a proper gate voltage

[1] Metal-Oxide-Semiconductor Field-Effect Transistor.

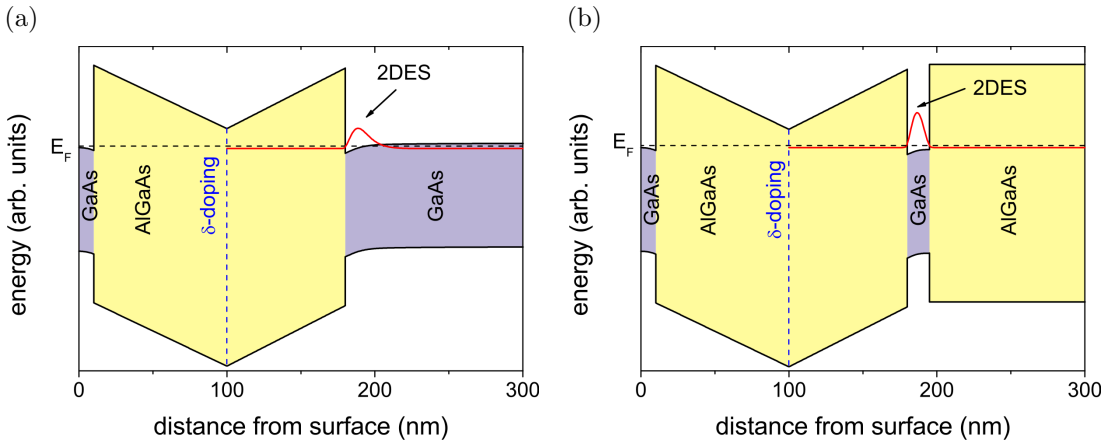

Figure 2.1: Schematic band diagrams of n-type doped GaAs/AlGaAs heterostructures. The potential well confining the electrons to two dimensions can be implemented either by (a) a MDSI structure or (b) a QW (here: single-sided doped). Electron probability distribution of the lowest subband is shown in red.

to the device, an inversion layer forms at the semiconductor-insulator interface - constituting the first 2D system studied. Despite the limited charge carrier mobilities achievable in MOSFETs, von Klitzing was able to measure the Quantum Hall Effect for the very first time in 1980 using such devices [19]. However, GaAs based semiconductor heterostructures grown by molecular beam epitaxy (MBE) allowed to reach much higher mobilities in the meantime and took over the role MOSFETs have played in research before. Heterostructures are made up of semiconducting materials of unequal band gaps and allow to tailor the band structure to one's needs simply by layering different materials with their dissimilar band gaps [20]. The confining potential necessary to restrict the motion of charge carriers to two dimensions can be generated either by a type I heterojunction (straddling gap) together with doping the wider-gap semiconductor[2] or by a Quantum Well (QW) structure (see fig. 2.1). Further enhancement of carrier mobility was brought about by the invention of *modulation remote doping* in 1978 [21]: By spatially separating the dopants from the confining potential well, scattering of charge carriers at ionized or neutral impurities - namely the donor or acceptor atoms - is drastically reduced.
Besides the most prominent heterostructures based on GaAs/AlGaAs many other 2D systems exist, like InGaAs/InAlAs or InGaAs/InP as well as the II-VI systems Hg(Mn)Te/HgCdTe and Cd(Mn)Te/CdMgTe. One advantage of the latter quantum structures over GaAs based ones is the possibility to incorporate magnetic manganese ions directly into the II-VI electron or hole gas sheet; GaMnAs on the contrary only exists as a bulk material. CdMnTe/CdMgTe structures for example thus feature 2D electrons plus additionally the huge spin splitting caused by the

[2] Also referred to as modulation doped single interface (MDSI) structure.

magnetic impurities, making them perfect candidates for spintronics applications. One drawback of II-VI structures however is the much lower achievable mobilities. The realization of a Cd(Mn)Te based 2DES will be discussed in detail in section 3.1.1.
With the successful preparation of graphene (one monolayer of graphite) in 2004 [22] this perfectly two-dimensional material has attracted growing interest due to its interesting characteristics. The charge carriers for instance may be viewed as massless Dirac fermions and a gate allows to tune from electron to hole conduction on the very same sample.

2.1.2 Quantum Mechanical Description

As it is well known from Quantum Mechanics the confinement of electrons in a potential well such as depicted in fig. 2.1 results in quantized energy eigenvalues E_i in growth direction, the so called subbands. The motion in the x-y-plane on the contrary remains unaffected and is still described by a parabolic dispersion relation, similar to the one of free electrons. To account for the periodic crystal potential the electrons are assigned with an effective mass m^*, different from their bare mass m_0; in the case of CdTe: $m^* = 0.10\, m_0$ [23]. This drastically simplifies the solution of the Schrödinger equation and yields the following energies of an electron in a 2DES:

$$E(i, k_x, k_y) = E_i + \frac{\hbar^2}{2m^*}(k_x^2 + k_y^2), \quad i = 0, 1, 2, \ldots \quad . \tag{2.1}$$

The exact locations of the subbands as well as their separation from each other are given by the particular shape of the potential well. In the case of low temperatures and moderate doping only the lowest subband is occupied and it therefore is often defined as energy zero.
Since the density of states of a two-dimensional system is independent of energy, it is constant for each 2DES subband:

$$D_i(E) = \frac{m^*}{\pi\hbar^2} = \text{const.} \quad . \tag{2.2}$$

A relation between carrier density n_s and Fermi wave vector k_F may be established by counting all occupied states in k space. Considering periodic boundary conditions and the fact that only states with $k < k_F$ are occupied at zero temperature one obtains:

$$k_F = \sqrt{2\pi n_s}. \tag{2.3}$$

2.1.3 Scattering Mechanisms

The mobility of electrons and holes in semiconductors is limited by various scattering processes. These can be divided into two subgroups, namely scattering

at impurities and scattering at phonons. The latter processes significantly limit mobilities at temperatures above 80 K but are negligible in transport experiments which are typically performed at liquid helium temperature. In this temperature range the following scattering mechanisms prevail [24, 25]:

- *Ionized impurity scattering*
  One of the major scattering mechanisms which mainly arises from ionized dopants. Their Coulomb potential accounts for small angle scattering of charge carriers. This process still is dominant in modulation doped structures, despite dopants and charge carriers being separated by a spacer layer from each other. Increasing the spacer thickness reduces the influence of ionized impurity scattering, however at the cost of a rapid decrease in carrier density.
- *Interface roughness scattering*
  Brought about by the roughness of the interface constituting the confining potential. It results in potential fluctuations along the path of the carriers causing them to scatter. This effect greatly limits mobilities in MOSFET devices but is of minor importance in MBE grown structures where the heterojunction is smooth on an atomic scale.
- *Alloy disorder scattering*
  The potential barriers in MDSI and QW structures are typically implemented by using wider-gap ternaries like AlGaAs or CdMgTe. Alloys do not have a microscopic periodicity as the atom on the anion sublattice for instance always is Te but the cation sublattice sites are randomly occupied by Mg or Cd. The fact that the electronic wave function extends into the barriers causes charge carriers to be scattered by the random alloy potential. Since the penetration depth is small, the contribution to the total scattering rate will be small, too.
- *Neutral/background impurity scattering*
  Due to limitations in vacuum and in the purity of the source materials every MBE grown sample exhibits so called background impurities - typically neutral foreign atoms. If located within the potential well they constitute scattering centers to the charge carriers. Another source of impurities are dopant atoms which have not been ionized (neutral impurities).

In summary, the main contributions to the total scattering rate of nowadays MBE samples arise on the one hand from background impurities in the electron or hole gas sheet and on the other hand from ionized impurity scattering at remote donor atoms. Those two mechanisms differ strongly in their scattering angle characteristics. Whereas background impurities exhibit an isotropic distribution of scattering angles, the weak potential fluctuations caused by remote ionized dopants only lead to scattering at small angles. For this reason the quality of a 2DES is characterized by two scattering times [26]:

The quantum lifetime (also: single particle lifetime) τ_q accounting for all scattering events, independent of angle

$$\frac{1}{\tau_q} = \int_0^\pi Q(\phi)\,\mathrm{d}\phi, \tag{2.4}$$

and the transport lifetime τ attributing more significance to large-angle scattering

$$\frac{1}{\tau} = \int_0^\pi Q(\phi)(1-\cos(\phi))\,\mathrm{d}\phi. \tag{2.5}$$

Here, $Q(\phi)$ denotes the probability of scattering through an angle ϕ, the latter being defined as the angle enclosed by the k vectors of incoming and outgoing particle. The transport lifetime τ usually is associated with the scattering time $\tilde{\tau}$ defined in the Drude model (see section 2.1.4).
In the case of very clean GaAs heterostructures small-angle scattering at remote donors is the dominant process leading to a ratio of $\tau/\tau_q > 100$ [27].

2.1.4 Low-Field Magnetotransport

Transport in a weak magnetic field may be described within the framework of the classical Drude model [28]. It assumes the semiconductor to be formed of positively charged ions from which the electrons are detached. Both are treated as solid spheres with collisions between them as the only type of interaction. An applied electric field $\vec{E} = (E_x, 0, 0)$ accelerates the electrons but due to collisions with the ions they move with a mean drift velocity

$$\vec{v_D} = -\frac{e\tilde{\tau}}{m^*}\vec{E} = -\mu\vec{E}, \tag{2.6}$$

where $\tilde{\tau}$ is the scattering time, m^* the effective mass, e the electronic charge and μ the electron mobility.
A magnetic field perpendicular to the 2DES plane induces an additional electric field E_y to compensate the Lorentz force. The components of the resistivity tensor $\boldsymbol{\rho}$ defined by Ohm's law

$$\vec{E} = \begin{pmatrix} \rho_{xx} & \rho_{xy} \\ \rho_{yx} & \rho_{yy} \end{pmatrix} \vec{j} = \boldsymbol{\rho}\vec{j} \tag{2.7}$$

then read

$$\rho_{xx} = \rho_{yy} = \frac{m^*}{n_s e^2 \tilde{\tau}} = \frac{1}{e n_s \mu} = \text{const.} \quad , \tag{2.8}$$

$$\rho_{xy} = -\rho_{yx} = \frac{B}{e n_s} \propto B. \tag{2.9}$$

Consequently, the Hall resistivity ρ_{xy} is linear in B and allows to determine the charge carrier density n_s. As the Drude model predicts the longitudinal resistivity ρ_{xx} to be independent of magnetic field, mobility μ is extracted from equation 2.8 for the case of zero magnetic field.
The components of the resistivity tensor are typically obtained from transport experiments on Hallbar devices and are related to the measured resistances via

$$\rho_{xx} = \frac{U_{xx}}{I} \cdot \frac{W}{L} = R_{xx} \cdot \frac{W}{L} \tag{2.10}$$

$$\rho_{xy} = \frac{U_{xy}}{I} = R_{xy}. \tag{2.11}$$

Here, L and W denote the Hallbar's length and width, respectively.

2.2 Quantum Hall Effects: Integer and Fractional

As it cannot account for Shubnikov-de Haas oscillations and Quantum Hall plateaus, the Drude model fails to describe electronic transport in strong magnetic fields. In this regime a quantum mechanical treatment is required. Again, let us consider a magnetic field in z direction.

2.2.1 Landau Quantization

Classically, electrons in a magnetic field move on cyclotron orbits. If their mean free path is much longer than the cyclotron radius they can perform several cycles and interfere with themselves before being scattered. As a consequence of Bohr Sommerfeld quantization the constant density of states of the 2DES splits into discrete energy levels, the so called *Landau levels* (LLs).
The fully quantum mechanical treatment starts with the following Hamiltonian [17]

$$H_0 = \frac{1}{2m^*}(\vec{p} - e\vec{A})^2 + V(z) + U(y). \tag{2.12}$$

Here, $V(z)$ is the quantization potential describing the confinement of the electrons caused by the potential well whereas $U(y)$ accounts for the restriction of the system to the width of the Hallbar. Calculating the eigenenergies of the system by initially setting $U(y) = 0$ and using a product ansatz yields:

$$E = E_i + \left(n + \frac{1}{2}\right)\hbar\omega_c \cos\theta + sg^*\mu_B B, \tag{2.13}$$

with LL index $n = 0, 1, 2, \dots$, cyclotron frequency $\omega_c = \frac{eB}{m^*}$ and spin quantum number $s = \pm\frac{1}{2}$. Further, μ_B denotes Bohr's magneton and g^* the Landé

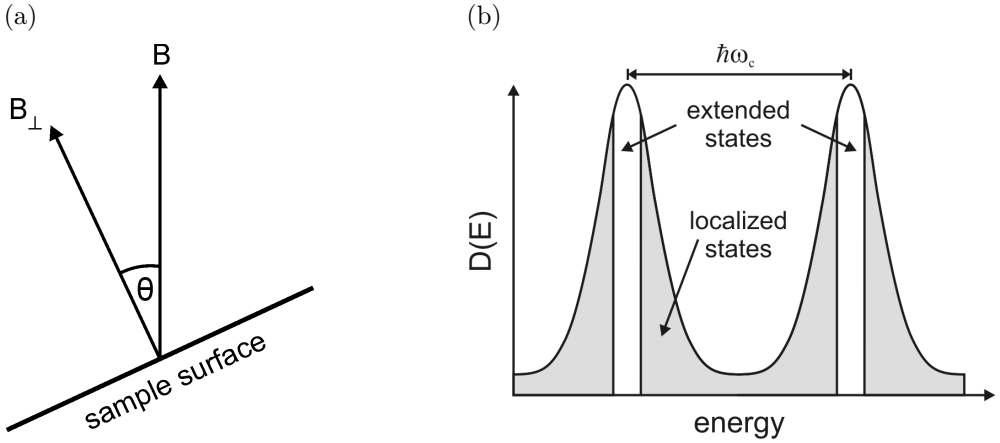

Figure 2.2: (a) Definition of the tilt angle θ. The perpendicular magnetic field is given by $B_\perp = B \cdot \cos\theta$. (b) Impurities and lattice defects lead to a broadening of Landau levels into extended and localized states. The latter do not contribute to transport but allow the Fermi energy to reside in between two levels.

g-factor of electrons including Zeeman effect and spin-orbit interaction. The term $\cos\theta$ accounts for the fact that spin splitting depends on the total magnetic field B but cyclotron splitting only on its component perpendicular to the sample plane $B_\perp = B \cdot \cos\theta$ (see fig. 2.2a for the definition of the angle θ).
Assuming that only the lowest subband ($i = 0$) is occupied, the presence of a magnetic field splits the constant density of states into a sequence of equidistant δ-peaks separated by an energy $\hbar\omega_c$. However, Landau levels in a real system are broadened by impurity effects giving rise to extended and localized states (see fig. 2.2b). The latter are located in the levels' tails and do not contribute to transport. LLs are highly degenerate, the field dependent carrier density n_L is given by

$$n_L(B) = g_s D_0 \hbar\omega_c = g_s \frac{eB}{h}, \tag{2.14}$$

where g_s is the spin degeneracy and D_0 the density of states of the lowest subband. The filling factor ν specifies the number of filled and spin split LLs:

$$\nu = \frac{n_s}{n_L} = \frac{n_s h}{eB}. \tag{2.15}$$

2.2.2 Integer Quantum Hall Effect

Fig. 2.3 depicts the consequences of LL formation on transport experiments at higher magnetic fields: The longitudinal resistance of a 2D system features Shubnikov-de Haas (SdH) oscillations accompanied by plateaus in the Hall resistance. The latter observation is known as the integer Quantum Hall effect (IQHE)

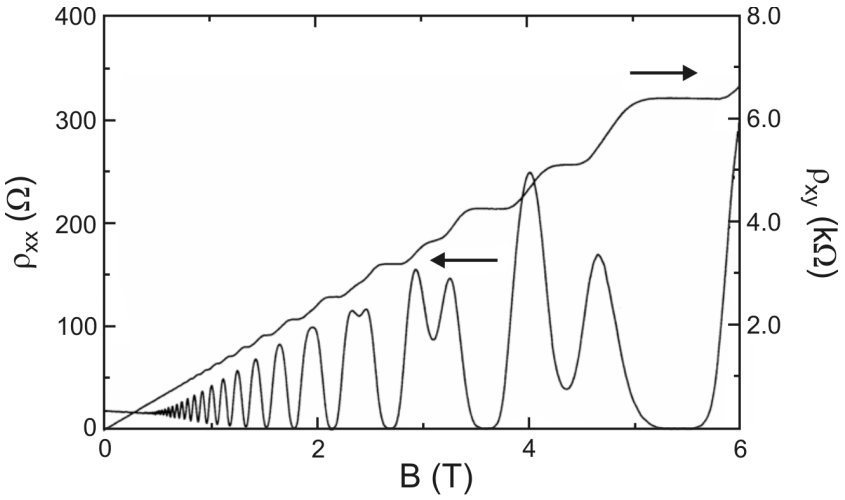

Figure 2.3: Typical transport data of a 2D electron gas. At magnetic fields higher than about 0.4 T quantum effects become visible which can no longer be explained within the Drude model: Shubnikov-de Haas oscillations in ρ_{xx} and plateaus in the Hall resistance ρ_{xy}. Source: Ref. [29].

exhibiting quantized resistances R_H independent of sample geometry and choice of material [19]:

$$R_H = \frac{1}{\nu}\frac{h}{e^2}, \quad \nu = 1, 2, \ldots \quad . \tag{2.16}$$

Since the von Klitzing constant $R_K = h/e^2 = 25812.807\ \Omega$ is solely given by natural constants it is used in metrology for the definition of a new standard for electrical resistance. The SdH oscillations are periodic in $1/B$ with their minima occurring at exactly the same magnetic field as the ρ_{xy} plateaus.
Both quantum transport phenomena can be understood within the edge channel picture and the Landauer-Buttiker formalism (for details refer to reference [17]). When discussing the magnetotransport properties of a 2DES we have so far considered the case $U(y) = 0$, i.e. neglected the width W of the Hallbar. The eigenenergies of the full Hamiltonian H_0 (see eq. 2.12) may be calculated in first order perturbation theory leading to the following results: States in the interior of the sample are unaffected by $U(y)$ but LLs bend towards higher energies at its edges (see fig. 2.4). At the points of intersection with the Fermi level E_F they give rise to the one-dimensional edge channels.
When ramping up the magnetic field both, LL spacing $\hbar\omega_c$ and degeneracy n_L increase such that E_F itself becomes field dependent and is shifted through the LL spectrum. Due to the presence of localized states, E_F cannot only lie within a LL but also reside in between two levels. In the latter case the entire current flows through the edge channels as they are the only states present at the Fermi energy. On either side of the Hallbar they carry current in opposite directions. Scattering between them is impossible due to their spatial separation, thus longitudinal resistance ρ_{xx} drops to zero. In contrast to this, ρ_{xx} becomes maximal when E_F

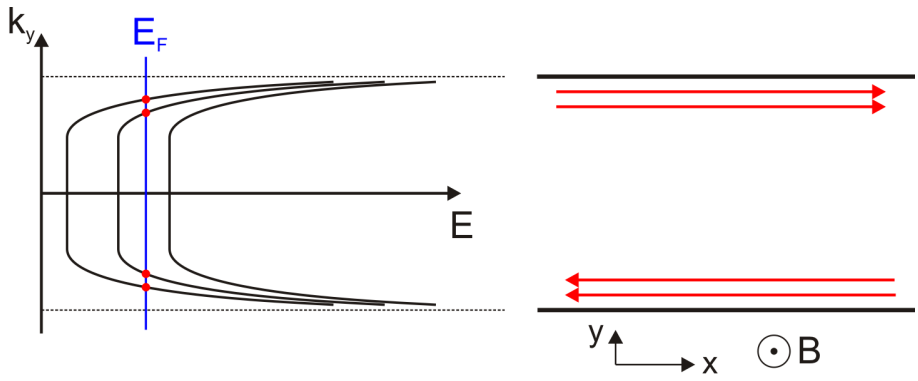

Figure 2.4: The finite width of the Hallbar causes the Landau levels at its edges to bend towards higher energies (left). This creates one-dimensional edge channels (red) at the Fermi energy E_F, featuring ballistic charge transport. On opposite sides of the Hallbar the edge channels carry current in different directions (right).

lies within a LL and charge carries can be scattered into lots of available states. Subsequent minima are separated on a $1/B$ scale by

$$\Delta\left(\frac{1}{B}\right) = \frac{g_s e}{n_s h}, \tag{2.17}$$

allowing to experimentally determine the charge carrier density n_s.
In a similar fashion the formation of plateaus in ρ_{xy} is related to the presence of edge channels (E_F residing between two LLs). According to the Landauer-Buttiker formalism the conductance of one edge channel is quantized and independent of its length:

$$G = \frac{e^2}{h}. \tag{2.18}$$

Furthermore, this transport theory relates the resistance R_H of a Quantum Hall plateau to the edge channel conductance via

$$R_H = G_{tot}^{-1}, \quad \text{with} \quad G_{tot} = \nu\frac{e^2}{h}. \tag{2.19}$$

2.2.3 Fractional Quantum Hall Effect

According to the previous considerations no more features in Hall and longitudinal resistance are expected, once filling factor $\nu = 1$ has been reached. Nevertheless, in 1982 Tsui *et al.* [30] observed a quantized Hall plateau at filling factor $\nu = 1/3$, i.e. for a partially filled lowest LL. In following years many more fractional states were discovered, first solely in GaAs-based systems (see fig. 2.5) later also in Si/SiGe [31] and in 2009/10 in graphene [32, 33] and in the oxide MgZnO/ZnO [34]. Within the framework of this PhD thesis the fractional Quantum Hall effect (FQHE) was

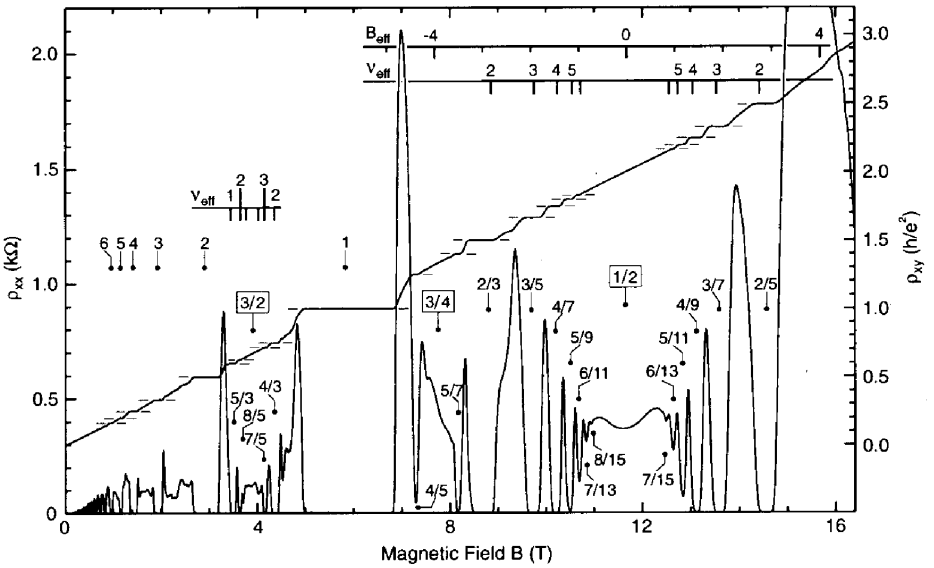

Figure 2.5: The fractional Quantum Hall effect in a high mobility GaAs/AlGaAs sample at $T = 30$ mK. Fractional states group in sequences around even denominator filling factors. Additional scales indicate CF filling factors and effective magnetic field B_{eff}, emphasizing the correspondence between IQHE of CFs and FQHE of electrons. Adopted from ref. [35].

demonstrated in two more new material systems: in the II-VI alloy CdTe [36] and for the very first time ever in a diluted magnetic semiconductor [37] (details are to be discussed in chapter 4).
The term FQHE refers to the emergence of quantized values of the Hall resistance associated with minima in ρ_{xx} at filling factors[3]

$$\nu = \frac{p}{q}, \quad \text{with} \quad p = 1, 2, 3, \ldots \quad q = 1, 3, 5, \ldots \quad . \tag{2.20}$$

The fractions occur in certain sequences, in case of the lowest LL ($\nu < 1$) given by

$$\nu = \frac{\nu_{CF}}{2\tilde{\phi}\nu_{CF} \pm 1} \quad \text{and} \quad \nu = 1 - \frac{\nu_{CF}}{2\tilde{\phi}\nu_{CF} \pm 1}, \tag{2.21}$$

where for now ν_{CF} and $\tilde{\phi}$ may be regarded as integers; both equations are related by electron-hole symmetry. The most prominent sequence ($\tilde{\phi} = 1$) features fractional states which group around $\nu = 1/2$, other weaker pronounced ones are found in the vicinity of filling factors 1/4, 3/4 and 3/2.
From a general point of view a vanishing longitudinal resistance implies a gap in the particles' excitation spectrum. Thus, the IQHE can be understood in terms of non-interacting electrons where the SdH oscillations are a result of cyclotron gaps in the single-particle density of states, i.e. the LL spectrum. In contrast, the

[3]The only known exception is the $\nu = 5/2$ state [38], whose properties are yet not entirely clear [39–42].

FQHE is a many-body effect due to Coulomb interaction between the electrons. This defines an energy scale relevant for FQHE, given by

$$E_C = \frac{e^2}{4\pi\varepsilon\varepsilon_0 l_B} \propto \sqrt{B}, \tag{2.22}$$

with the magnetic length $l_B = \sqrt{\hbar/eB}$. It is due to Coulomb interaction that at higher magnetic fields gaps in the excitation spectrum of the correlated many-electron ground state arise, causing Hall plateaus and ρ_{xx} minima at fractional fillings. Laughlin [43] was the first to propose a wave function allowing to describe the ground states at $\nu = 1/(2\tilde{\phi} + 1)$, soon followed by a hierarchy scheme [44, 45] to account for other fillings, too. A conclusive picture however did not emerge until 1989 when Jain presented the *Composite Fermion* model of the FQHE [46]. In his theory the FQHE is mapped onto the IQHE of fermionic quasiparticles - so called Composite Fermions (CFs) - consisting of an electron and an even number of magnetic flux quanta.
In detail this can be understood by a *Chern-Simons* field theoretical approach [47, 48] which transforms the system of interacting electrons to an equivalent one by adding the Chern-Simons vector potential $\vec{a}$ to the Hamiltonian of the problem. It is defined by [35]

$$\vec{a}(\vec{r}_i) = -2\tilde{\phi}\frac{\phi_0}{2\pi}\sum_{i\neq j}\frac{\vec{e}_z \times (\vec{r}_i - \vec{r}_j)}{|\vec{r}_i - \vec{r}_j|^2}, \tag{2.23}$$

where $\vec{r}_i$ is the position of the i^{th} electron, $\phi_0 = h/2e$ the magnetic flux quantum and $\vec{e}_z$ the unit vector in z direction. The magnetic field $\vec{b}$ associated with the above vector potential is located at the position of each electron and reads

$$\vec{b}(\vec{r}_i) = \nabla \times \vec{a}(\vec{r}_i) = -2\tilde{\phi}\phi_0 \sum_{i\neq j}\delta(\vec{r}_i - \vec{r}_j), \tag{2.24}$$

with the Dirac delta function $\delta(\vec{r})$. In a nutshell, the Chern-Simons transformation adds $2\tilde{\phi}$ magnetic flux quanta to each electron, pointing opposite to the external field. These composite particles carry an elementary charge e and obey Fermi statistics; their density equals the one of the electrons, n_s. In order to analyze the consequences of the Chern-Simons transformation, it is common practice to make a mean field approximation. The singular gauge field $\vec{b}$ (eq. 2.24) is considered to be smeared out to a uniform magnetic field, opposite to the external one:

$$\langle b \rangle = -2\tilde{\phi}\phi_0 n_s. \tag{2.25}$$

Thus, Composite Fermions see a residual field

$$B_{\mathit{eff}} = B + \langle b \rangle = B - 2\tilde{\phi}\phi_0 n_s. \tag{2.26}$$

Within this approximation the initial Coulomb interaction between the electrons is compensated such that the composite particles become *non-interacting*. B_{eff} cancels exactly for even denominator fillings $\nu = 1/2\tilde{\phi}$ and CFs behave similar to electrons around $B = 0$ T.
In summary the basic ideas of the CF model are [35]:

- Electrons capture $2\tilde{\phi}$ flux quanta to become fermionic composite particles.
- The addition of virtual flux quanta compensates the Coulomb interaction. Hence, CFs can in a fist approximation be treated as non-interacting. This allows a standard single-particle description of the FQHE.
- Composite Fermions experience a reduced effective magnetic field given by eq. 2.26. Similar to electrons they form CF-LLs in this reduced field, resulting in Hall plateaus and ρ_{xx} minima at fractional fillings.
- The filling factor ν_{CF} of a CF-LL is defined by the effective field via: $\nu_{CF} = n_s\phi_0/B$. It is related to the fractional filling factor ν of electrons by eq. 2.21.

Further details on the theory of the FQHE can be found in various textbooks [35, 49–51].
So far we have not considered the effect of Zeeman splitting on the Composite Fermion model. Due to the small g-factor of GaAs ($g^*_{\mathrm{GaAs}} = -0.46$) its influence has been neglected in early theoretical approaches, but becomes evident in experiments performed in tilted magnetic fields [52]. The observed angular dependence (see fig. 2.6) of energy gaps Δ_ν associated with fractional fillings - i.e. their opening and closing - can easily be understood by assigning each CF with a spin [53]. In the vicinity of $\nu = 1/2$ for instance, CFs are quantized into CF-LLs by the perpendicular component of the residual field [48]

$$B_{\mathit{eff}} = B_\perp - B_{1/2}, \tag{2.27}$$

where $B_{1/2}$ is the perpendicular magnetic field at $\nu = 1/2$ and $B_\perp = B \cdot \cos\theta$ with tilt angle θ. Zeeman splitting on the other hand depends on total field B, hence leading to crossings of spin-up and down CF-LLs of different level index (see fig. 2.7). Tilting the sample causes all fractional states to shift to a larger total field for an unchanged B_{eff}. To account for the consequences, let us for example focus on a FQH state in a non-magnetic material (e.g. GaAs) corresponding to filling factor $\nu_{CF} = 2$: At $B = 0$ T this state would occupy both degenerate spin states of the lowest CF-LL with the Fermi energy E_F^{CF} consequently residing in a gap of size $\Delta_\nu = \hbar e|B_{\mathit{eff}}|/m_{CF}$ [54]. Here, m_{CF} denotes the CF mass. When B is increased (which is equivalent to tilting the sample) the upper spin branch of the lowest CF-LL and the lower spin branch of the next level approach each other until they cross at a specific field value. This corresponds to a closing of the gap Δ_ν. With further increasing tilt the gap will open again and finally stay constant due to no more level crossings. The fan chart depicted in fig. 2.7

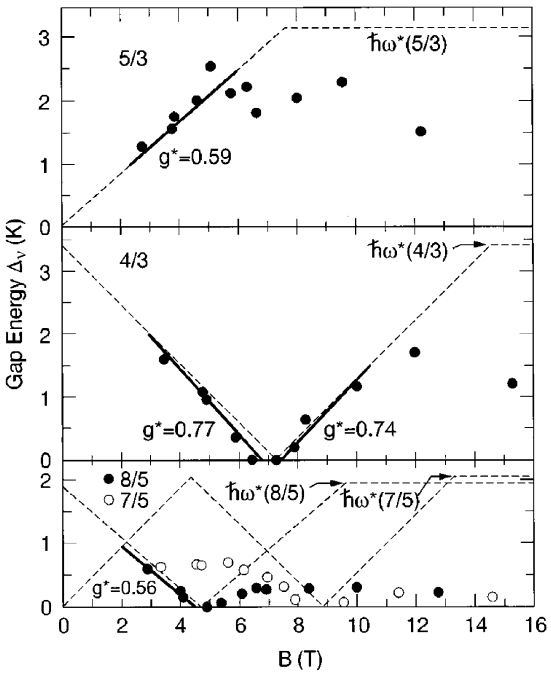

Figure 2.6: Gap energies Δ_ν as function of total magnetic field B for various FQH states in GaAs. Dashed lines indicate the theoretically expected angular gap dependence. Solid lines are fits to the data allowing to determine the CF g-factor to the values given in the graphs. Adjusted from ref. [54].

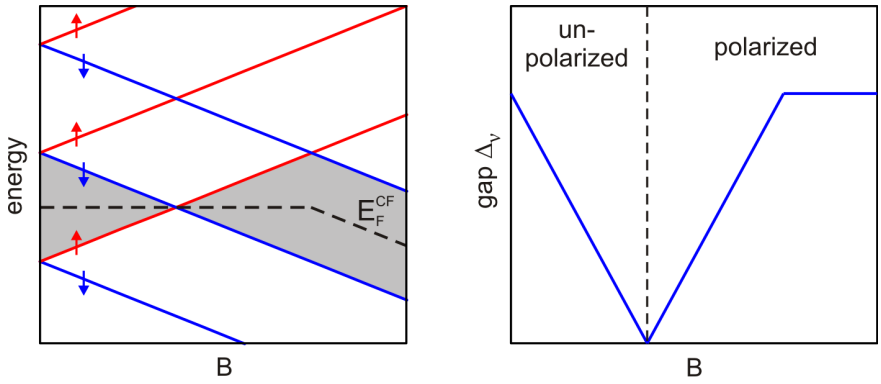

Figure 2.7: Schematic representation of a CF-LL fan diagram of a non-magnetic semiconductor for fixed B_{eff} and varying total field B (left). The dashed line indicates the position of the CF Fermi energy E_F^{CF} in the case of $\nu_{CF} = 2$. When the total magnetic field is increased by tilting the sample, the gap Δ_ν of the corresponding fractional state (shaded region) starts to close first before reopening at higher tilt (right). The ground state spin polarization is given by the number of spin-up vs. spin-down levels below E_F^{CF} and changes from unpolarized to fully polarized.

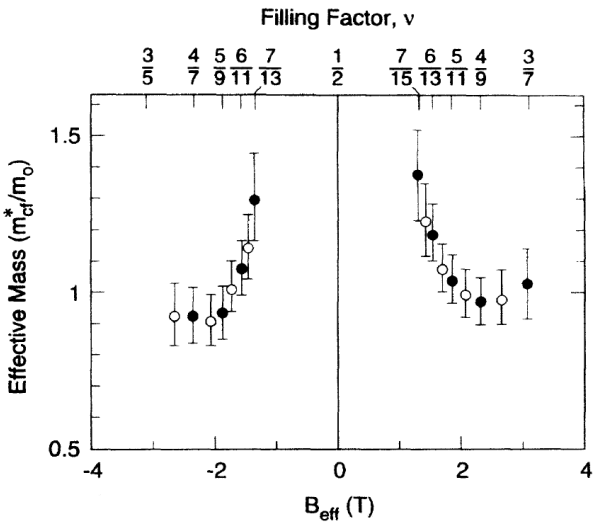

Figure 2.8: Experimentally determined filling factor dependency of Composite Fermion mass m_{CF} in GaAs. A rapid mass increase is observed as the filling factor approaches $\nu = 1/2$, i.e. $B_{eff} \to 0$ T. Adjusted from ref. [55].

additionally allows to determine the spin polarization of the CF system at any filling factor ν_{CF} and Zeeman energy: It is simply given by the number of spin-up vs. spin-down branches below E_F^{CF}.
In GaAs-based systems the Composite Fermion g-factor has experimentally been determined to be similar to the one of electrons [53]. Their mass m_{CF} was found to be about ten times the electron mass $m^*_{\mathrm{GaAs}} = 0.066\ m_0$ with an additional drastic enhancement as the filling factor approaches $\nu = 1/2$ [55] (see fig. 2.8).

2.3 sp-d Exchange Interaction

When manganese ions are incorporated into a $\mathrm{A^{II}B^{VI}}$ host lattice they give rise to a spin-dependent interaction between electrons localized in their $3d^5$ shell and those of the semiconductor's conduction and valence bands (*sp* bands). This so called '*sp-d* exchange interaction' leads to a strong and magnetic field dependent enhancement of the spin splitting, characteristic of semimagnetic $\mathrm{A^{II}_{1-x}Mn_xB^{VI}}$ alloys. It influences all effects involving conduction or valence band electrons, such as magneto-optical as well as transport properties which strikingly differ from those of their nonmagnetic counterparts.
This chapter partially is adopted from reference [1] and will focus mainly on the interaction between conduction band and Mn $3d^5$ electrons (*s-d* exchange) since the heterostructures under investigation are n-type doped.

2.3.1 Exchange Hamiltonian

Starting point for the following considerations is a 2D charge carrier system in a nonmagnetic semiconductor such as CdTe, subjected to an external magnetic field.

The Landau level structure shall be described by an appropriate Hamiltonian H_0 which contains all necessary information apart from the *sp-d* exchange contribution. The corresponding eigenenergies of, for example a 2DES, are given by (see eq. 2.13)

$$E = E_i + \left(n + \frac{1}{2}\right)\hbar\omega_c \cos\theta + sg^*\mu_B B, \tag{2.28}$$

where g^* is the Landé g-factor of electrons in the $A^{II}B^{VI}$ crystal.
Once the semiconductor contains localized magnetic moments, the above energy spectrum will be modified by the exchange interaction of band electrons with those moments (namely the $3d^5$ electrons). This may be expressed by adding an exchange term H_{ex} to the original Hamiltonian H_0; the total Hamiltonian then reads

$$H = H_0 + H_{ex} = H_0 + \sum_{\vec{R}_i} J^{sp-d}(\vec{r} - \vec{R}_i)\vec{S}_i \cdot \vec{\sigma}. \tag{2.29}$$

$\vec{S}_i$ and $\vec{\sigma}$ denote the spin operators of Mn^{2+} ion and band electron, respectively, J^{sp-d} the *sp-d* exchange coupling constant. The vectors $\vec{r}$ and $\vec{R}_i$ define the positions of band electron and magnetic impurity, the summation is only carried out over lattice sites occupied by Mn^{2+} ions.
In order to simplify H_{ex} two convenient approximations can be made:

- *Mean-field approximation*
  Due to the large extension of its wave function the electron 'sees' lots of manganese ions at the same time. Therefore the spin operators $\vec{S}_i$ may be replaced by the average spin $\langle\vec{S}\rangle$ per Mn site. In the case of a paramagnetic system (low Mn content x) and an external magnetic field in z direction, $\langle\vec{S}\rangle = \langle S_z\rangle$ holds, with $\langle S_z\rangle$ being related to the magnetization M of the system via (see eq. 1.5)

$$\langle S_z\rangle = -\frac{M}{xN_0 g\mu_B} = -S\mathcal{B}_S\left(\frac{g\mu_B SB}{k_B T}\right). \tag{2.30}$$

- *Virtual crystal approximation*
  As a further consequence of the fact that the electronic wave function spans many lattice sites, one can make the following substitution:

$$J^{sp-d}(\vec{r} - \vec{R}_i) \;\rightarrow\; xJ^{sp-d}(\vec{r} - \vec{R}). \tag{2.31}$$

  Here, $\vec{R}$ now represents the coordinate of every site of the cation sublattice.

As a result of above assumptions H_{ex} reduces to a lattice periodic function

$$H_{ex} = \sigma_z\langle S_z\rangle x\sum_{\vec{R}} J^{sp-d}(\vec{r} - \vec{R}), \tag{2.32}$$

with the summation extending over all cation sites.
At elevated manganese concentrations x equations 2.30 to 2.32 need to be modified by introducing the effective parameters x_{eff} and T_{eff} as discussed in section 1.3.

2.3.2 Eigenenergies of a Parabolic Conduction Band

In order to study the consequences of magnetic impurities (and hence of H_{ex}) on the Landau level spectrum of a 2DES we will from now on consider conduction band electrons with a parabolic energy dispersion. Only the lowest subband shall be occupied. In the paramagnetic limit the corresponding eigenenergies of the total Hamiltonian (see eq. 2.29) are given by [56]

$$\begin{aligned} E_{n,\uparrow\downarrow} &= \left(n+\frac{1}{2}\right)\hbar eB\cos\theta/m^* \pm \\ &\pm \frac{1}{2}\left[g^*\mu_B B + \alpha N_0 x_{\mathit{eff}} S\mathcal{B}_S\left(\frac{g\mu_B SB}{k_B T_{\mathit{eff}}}\right)\right]. \end{aligned} \tag{2.33}$$

Here, the energy of the lowest subband $E_{i=0}$ is chosen as the zero energy point and $\alpha N_0 = 220$ meV denotes the *s-d* exchange constant of CdMnTe. Both parameters, x_{eff} and T_{eff} account for the reduction of magnetization due to antiferromagnetic exchange interaction between Mn spins (see section 1.3).
Introducing an effective *g*-factor g_{eff} allows to rewrite the above equation in the following form:

$$E_{n,\uparrow\downarrow} = \left(n+\frac{1}{2}\right)\hbar eB\cos\theta/m^* \pm \frac{1}{2}g_{\mathit{eff}}\mu_B B, \tag{2.34}$$

with

$$g_{\mathit{eff}} = g^* + \alpha\frac{M(B, x_{\mathit{eff}}, T_{\mathit{eff}})}{g\mu_B^2 B}. \tag{2.35}$$

Hence, DMSs may be treated as nonmagnetic materials except for the fact that the Zeeman splitting now is dependent on magnetic field, temperature and Mn concentration. It is important to note that for II-VI alloys the exchange contribution to the spin splitting only is present when an external magnetic field is applied. This is due to the fact that - depending on temperature and manganese concentration - these substances are either paramagnetic or exist in a spin-glassy or antiferromagnetic state. In all three cases the macroscopic magnetization vanishes in the absence of an external field and $g_{\mathit{eff}} = g^*$ holds. Despite the presence of a magnetic field, low temperatures are additionally necessary to observe an exchange enhancement of the *g*-factor since the magnetization at elevated temperatures is negligibly small. On the contrary, III-V based DMSs are ferromagnetic even at higher temperatures with the exchange splitting consequently prevailing at $B = 0$ T. The Curie temperature of GaMnAs for instance has been reported to be as high as 185 K [57].
Due to *sp-d* exchange interaction $\mathrm{A}^{\mathrm{II}}_{1-x}\mathrm{Mn}_x\mathrm{B}^{\mathrm{VI}}$ alloys differ in the following properties from their nonmagnetic counterparts:

- Since Zeeman and exchange term in eq. 2.35 are of opposite sign, spin splitting E_Z is in a nonlinear fashion dependent on magnetic field (see

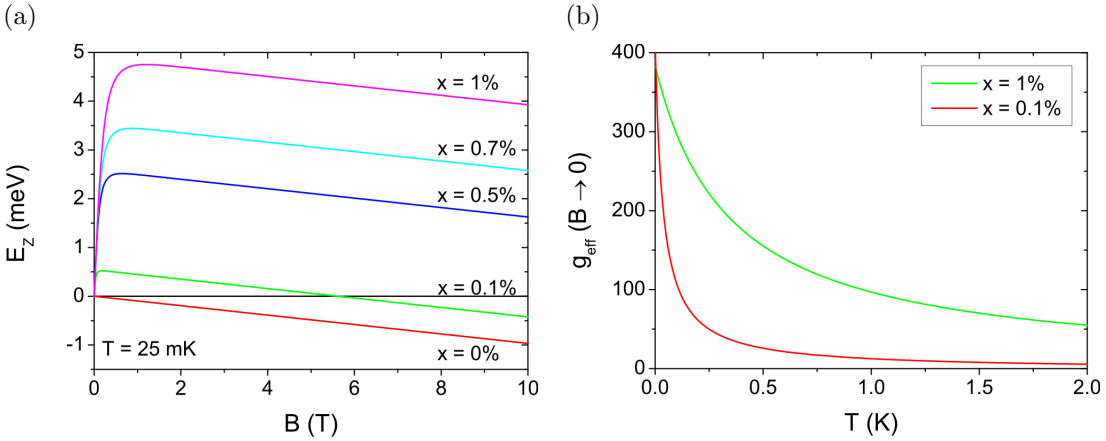

Figure 2.9: (a) Zeeman splitting E_Z of CdMnTe for various manganese contents x at $T = 25$ mK. The steep rise of E_Z at low fields is caused by the second term in equation 2.35, except for the case of nonmagnetic CdTe, where $g_{eff} = g^* = -1.67$ holds. (b) Temperature dependence of the effective g-factor g_{eff} in the limit $B \to 0$ T.

fig. 2.9a). At low B the exchange contribution to the spin splitting is dominant and the latter may easily exceed cyclotron splitting $\hbar\omega_c$. As soon as the Brillouin function contained in the exchange term saturates at higher fields, the negative sign of g^* accounts for the slow decrease of E_Z. Dependent on manganese concentration and temperature a complete cancelation of both contributions occurs at a specific magnetic field value.

- As a result of the dependence of E_Z on the magnetic field the entire Landau level spectrum is modified and crossings of LLs of different level index and spin orientation become possible (see fig. 2.10).
- The magnitude of g_{eff} is tunable via temperature T and manganese concentration x (compare figs. 2.9a and b). In the limit $B \to 0$ T values of the effective g-factor ranging from -1.67 to $+350$ can easily be obtained at mK temperatures.

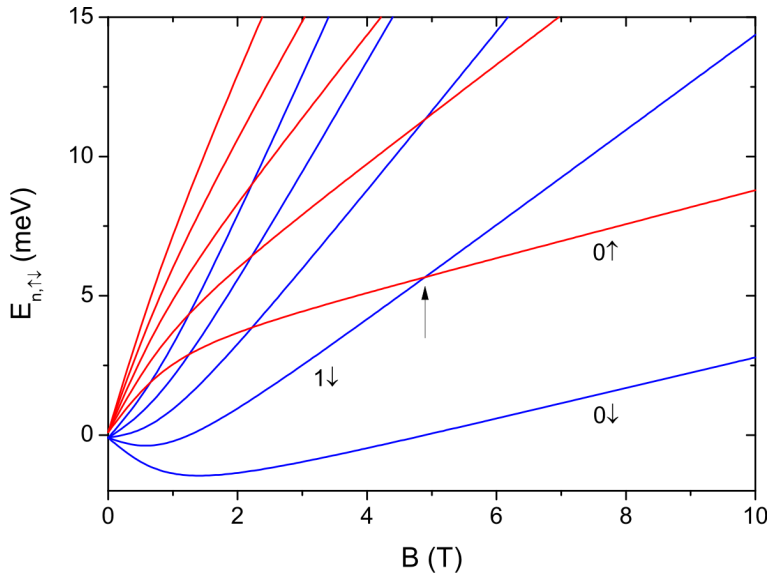

Figure 2.10: Landau level fan chart of CdMnTe at 1.4 K. Due to *s-d* exchange interaction the entire spectrum is in a nonlinear fashion dependent on magnetic field and levels of opposite spin orientation may cross at the Fermi energy (arrow). Here, $x_{eff} = 0.0095$, $\theta = 0°$ and $T_{eff} = (1.4 + 0.25)$ K.

2.3.3 Impact on Magnetotransport

As already discussed above, the nonlinear magnetic field dependence of spin splitting E_Z strongly modifies the LL spectrum of a DMS. As a consequence magnetotransport anomalies in ρ_{xx} arise, such as the Quantum Hall Ferromagnet spike or a beating pattern at low fields:

- *Quantum Hall Ferromagnetism*
  If LLs corresponding to opposite spin orientations and level index cross at the Fermi energy a spontaneous spin order may appear at low temperatures - known as the Quantum Hall Ferromagnet (QHF) [23, 56]. At the points of LL coincidence (see fig. 2.10 as an example) electrons orient their spins parallel and fill up only one of the two levels, while the other one remains empty. This is energetically favorable since electrons are furthest apart in this configuration and Coulomb energy consequently is lowest. Due to a locally varying potential landscape either the spin-up or -down LL is occupied in a certain region of the sample. Edge-like channels form at the domain boundaries and give rise to sharp and hysteretic spikes in ρ_{xx}. Similar observations have been made in GaAs-based systems [58], but LL coincidence needs to be induced by tilting the sample here.

- *Beating pattern*
  Due to *s-d* exchange the spin splitting of a DMS may greatly exceed the cyclotron gap $\hbar\omega_c$ in the case of low magnetic fields and low temperatures.

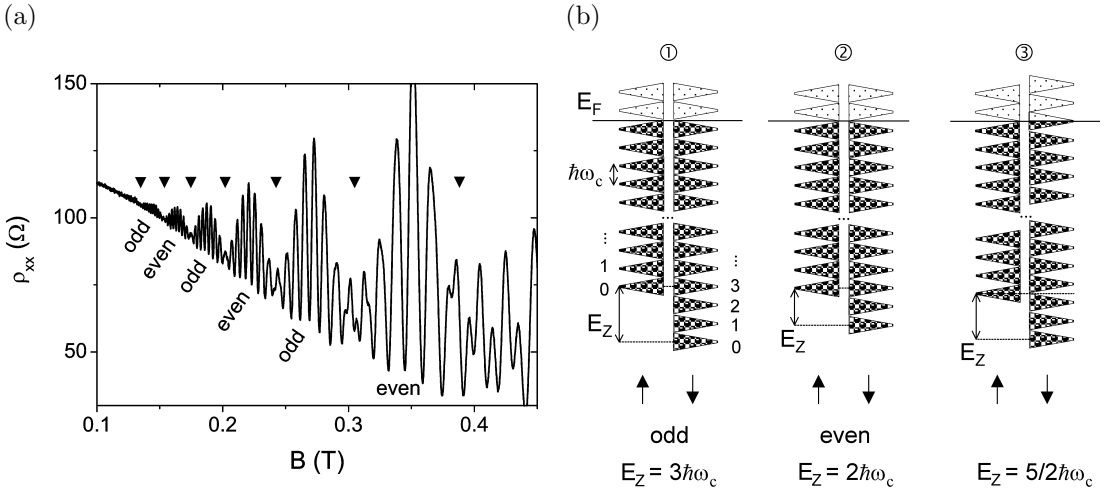

Figure 2.11: (a) Low-field magnetoresistance ρ_{xx} of a CdMnTe sample with $x = 0.0024$. The beating pattern with nodes (filled triangles) is clearly observable down to fields of roughly 0.1 T. The parity of the filling factor is indicated. (b) Arrangement of spin-up and -down LLs for specific values of Zeeman energy E_Z with respect to cyclotron splitting $\hbar\omega_c$. In cases 1+2 a well defined gap in the density of states exists, giving rise to SdH oscillations. The filling factor parity is simply given by the number of split-off lowest LLs. When no gap in the density of states (case 3) is present the amplitude of the SdHs is suppressed. Adjusted from ref. [59].

In this regime the amplitude of the SdH oscillations exhibits a distinct beating pattern with nodes (see fig. 2.11a) [59, 60]. The latter separate regions of even and odd filling factor parity and their position shifts to lower magnetic fields as T is increased. This observation can easily be understood with the help of fig. 2.11b depicting the arrangement of spin-up and -down LLs at characteristic field values. Each time the Zeeman energy equals an integer multiple of $\hbar\omega_c$ the Fermi energy can reside in well defined gaps in the density of states. In such situation the filling factor parity of the (well pronounced) SdH minima only depends on the number of split-off lowest LLs. On the contrary, when $E_Z = (\tilde{n} + 1/2)\hbar\omega_c$, with $\tilde{n} = 0, 1, 2, \ldots$, holds and LLs are sufficiently broad, the density of states features no gaps. Hence, the amplitude of the SdH oscillations is suppressed (nodes).

Both, the QHF spike and the beating pattern allow to extract the manganese concentration x from magnetotransport data. Details are discussed in section 4.2.

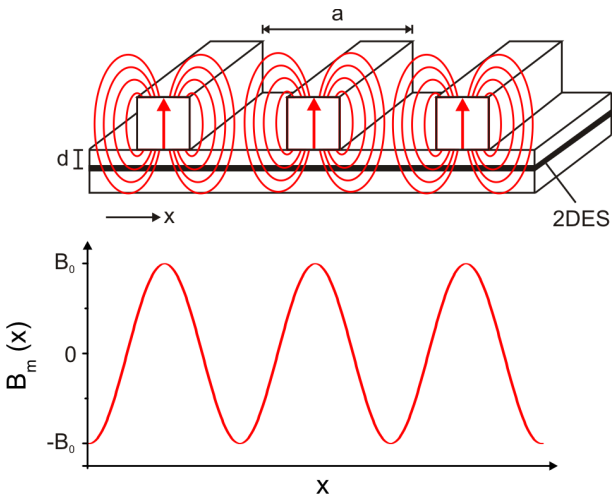

Figure 2.12: Basic concept of magnetic modulation (top). A grating of ferromagnetic stripes on the sample surface gives rise to a stray field B_m in the underlying 2DES. Here, the stripes of period a are magnetized perpendicular to the 2DES plane. In first approximation $B_m(x)$ is of sinusoidal profile at 2DES depth d (bottom).

2.4 Modulated Structures

A two-dimensional electron system subjected to a weak and spatially periodic modulation potential features *commensurability oscillations* of $1/B$ periodicity in the low-field longitudinal magnetoresistance. These are distinct from the usual SdH oscillations and reflect an interplay between the modulation period a and the cyclotron radius $R_c = k_F l_B^2 = \hbar\sqrt{2\pi n_s}/eB$ at the Fermi energy. The magnitude of R_c is tuned by the external magnetic field. Indeed, magnetotransport is strongly affected by commensurability effects at a ratio of $a/R_c \approx 1$, provided the modulation period is shorter than the electron mean free path $l_{mfp} = \hbar\mu\sqrt{2\pi n_s}/e$. The following sections will briefly discuss the case of an unidirectional modulation potential (1D modulation) whose amplitude is low in comparison with Fermi energy or external field.

2.4.1 Experimental Findings

Commensurability effects are basically classified by the nature of the modulating potential, i.e. magnetic vs. electrostatic modulation. The latter is easily achieved either by a periodically patterned top gate [61] or by in-situ illumination of the sample with a laser interference pattern and making use of the persistent photoeffect (e.g. GaAs) [62, 63]. Accordingly, a grating of ferromagnetic stripes (e.g. iron, dysprosium) induces an alternating magnetic stray field B_m in the plane of the 2DES [64] (see fig. 2.12). Parts of experiments performed within the framework of this PhD utilize exactly this method to create periodic magnetic fields (see chapter 5), even though not exploring magnetically driven commensurability effects. In piezoelectric materials - such as GaAs and CdTe - the magnetic potential typically is accompanied by a strain induced electrostatic one, caused by the different thermal expansion coefficients of ferromagnet and semiconductor.

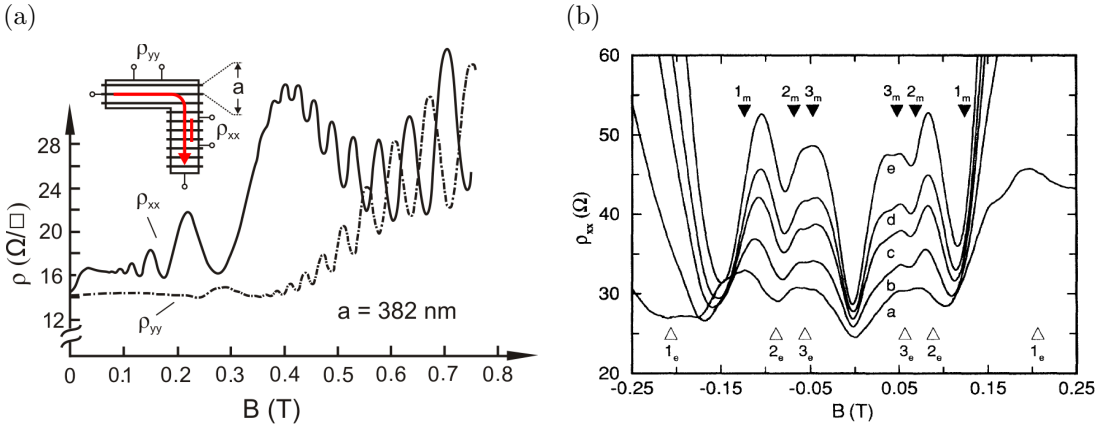

Figure 2.13: (a) Commensurability oscillations caused by a (weak) one-dimensional electrostatic modulation of period $a = 382$ nm. The resistance component ρ_{xx} (current flow perpendicular to the modulation) features well developed oscillations and a positive magnetoresistance around $B = 0$ T. Oscillations in ρ_{yy} are less distinct and opposite in phase. SdH oscillations become visible at about 0.4 T. Inset: Sample geometry and definition of magnetoresistivity components ρ_{xx} and ρ_{yy}. Adopted from ref. [62]. (b) Magnetic modulation perpendicular to the current flow. Traces a) to e) show the resistance ρ_{xx} for increasing magnetization of the ferromagnetic stripes. Full triangles mark the magnetic flatband condition, open triangles the electric one. Adjusted from ref. [64].

Fig. 2.13 depicts the influence of both, a one-dimensional weak electrostatic modulation and a magnetic modulation on magnetotransport. Commonly, the following notation is used: the longitudinal resistance is referred to as ρ_{xx} when the current flows perpendicular to the modulation and referred to as ρ_{yy} in case of parallel current flow (see inset of fig. 2.13). Experimental observations are:

- At low magnetic fields and when $l_{mfp} > a$ holds, $1/B$ periodic commensurability oscillations (COs) emerge in ρ_{xx} for magnetic as well as for electrostatic modulation. They are distinct from the usual SdH oscillations due to their larger periodicity. Similar features in ρ_{yy} could only be observed in the case of an electrostatic modulation potential.
- The ρ_{xx} minima positions are given by the *flatband condition*

$$2R_c = \left(\lambda \pm \frac{1}{4}\right) a, \quad \text{with} \quad \lambda = 1, 2, 3, \ldots \quad . \tag{2.36}$$

  Here, the (+) sign refers to magnetic and the (-) sign to electrostatic COs, respectively. Oscillations in ρ_{yy} are less distinct and opposite in phase with those observed in ρ_{xx}.
- Around $B = 0$ T a positive magnetoresistance (MR) arises in ρ_{xx}, however not in ρ_{yy}.
- Unlike SdHs, commensurability oscillations sustain temperatures as high as 40 K [65].

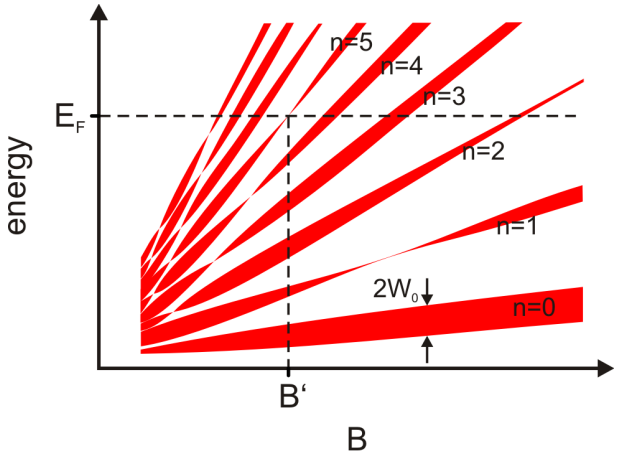

Figure 2.14: Landau level spectrum in the presence of a weak unidirectional modulation. The levels are broadened into bands of oscillatory bandwidth $2W_n$. For the sketched position of the Fermi energy E_F the flatband condition is met at $B = B'$ in the $n = 5$ LL and a minimum is expected to form in ρ_{xx}. Adopted from ref. [70].

2.4.2 Theory - at a Glance

Commensurability oscillations can either be explained semiclassically [66] or by a quantum mechanical model [67–69] which shall briefly be discussed. Its basic idea is a modulation-induced modification of the Landau level spectrum.
Starting point is the Hamiltonian of a 2DES subject to a magnetic field B, whose eigenenergies (eq. 2.13) are perturbed by either electrostatic or magnetic modulation in x direction

$$V(x) = V_0 \cos(qx) \tag{2.37}$$
$$B_m(x) = B_0 \cos(qx), \tag{2.38}$$

with $q = 2\pi/a$. In the limit of weak modulation ($V_0 \ll E_F$ or $B_0 \ll B$) the impact on the LL spectrum can be calculated in first order perturbation theory. The LLs are found to be broadened into bands with a magnetic field dependent bandwidth $2W_n$ (see fig. 2.14). At finite width the dispersion of the Landau bands becomes k_y dependent thus leading to a group velocity in y direction. This is associated with an additional conductivity contribution $\Delta\sigma_{yy}$ (band conductivity) which directly is linked to an increased resistance ρ_{xx} via the relation $\rho_{xx} \approx \sigma_{yy}/\sigma_{xy}^2$. Each time the Landau bands at the Fermi energy become flat ($W_n = 0$) $\Delta\sigma_{yy}$ vanishes and the COs therefore exhibit a minimum as expressed by eq. 2.36. In contrast, band conductivity has no impact on the resistance ρ_{yy} (current flow parallel to the modulation).
Additionally, the modulation potential causes an altered dependence of transport lifetime τ on the density of states at the Fermi energy. This so called collision broadening contribution is isotropic and leads to resistance maxima both in ρ_{xx} and ρ_{yy} whenever the flatband condition is met ($W_n = 0$). This mechanism however is weak compared to contributions stemming from band conductivity. Consequently, the conductivity contribution of collision broadening is not observed in ρ_{xx} but accounts for the antiphase resistance oscillations in ρ_{yy}.

The emergence of a positive magnetoresistance (MR) in samples with current flow perpendicular to the modulation can be understood within the semiclassical model of *magnetic breakdown* [71]. Typically, due to Lorentz force $F_L = ev_F B$, electrons move on (closed) cyclotron orbits in a magnetic field, where $v_F = \hbar\sqrt{2\pi n_s}/m^*$ is the Fermi velocity. Additional open trajectories may however exist in modulated structures at low fields, where the electrostatic force due to the modulation potential $F_{el} = -\mathrm{d}V(x)/\mathrm{d}x$ exceeds F_L. Those trajectories run along the equipotential minima of the modulation in y direction and account for the increase in ρ_{xx} until they are quenched at a critical field $\tilde{B}$. At this specific field value - given by condition $F_L = F_{el}$ - the magnetoresistance saturates and allows to estimate the magnitude of V_0. Similar arguments apply for the case of magnetic modulation: Here, the positive MR saturates when the external field exceeds the stray field amplitude B_0 of the stripe grating.

3 Sample Preparation and Experimental Setup

Starting from the bare wafer material the following sections describe the fabrication of both, the fractional Quantum Hall effect (FQHE) samples and the spin transistor devices. In the latter case a grating of ferromagnetic stripes is defined by means of electron beam lithography (EBL) on the sample surface. The important task in this context is to deposit a ferromagnet with sufficiently large magnetic stray field. We use either dysprosium (Dy) or iron (Fe), with the first material requiring very good vacuum conditions during deposition due to its fast oxidation in air.
One of the biggest challenges when dealing with CdTe and CdMnTe 2DESs is making ohmic contacts. This step crucial for any later magnetotransport experiment shall be discussed in detail in chapter 3.1.4.

The FQHE in the CdTe/CdMnTe material system as well as magnetoresistance effects stemming from the artificial spin superstructure could only be observed at temperatures below 1 K. Thus, all experiments were carried out in a dilution refrigerator at temperatures down to 15 mK. This cryostat system and the measurement electronics employed are introduced in chapter 3.2.

3.1 Sample Preparation

3.1.1 Wafer Material

All investigations were carried out on modulation doped CdTe or CdMnTe quantum well structures grown by MBE (molecular beam epitaxy) in the lab of Prof. Wojtowicz in Warsaw [72]. Fig. 3.1 depicts the typical structure of such a wafer: Starting point is an undoped (001)-GaAs substrate on which $2-3$ μm CdTe and $1-2$ μm $Cd_{1-y}Mg_yTe$ ($y = 0.135 - 0.29$) buffer layers are grown, followed by a CdTe/CdMgTe superlattice (SL). Those first three layers allow the strain caused by the mismatch between the lattice constants of GaAs ($a = 0.5653$ nm) and CdTe ($a = 0.6480$ nm) to relax. Upon the SL the first CdMgTe barrier confining the $10-30$ nm wide QW is grown, the latter consisting either of CdTe

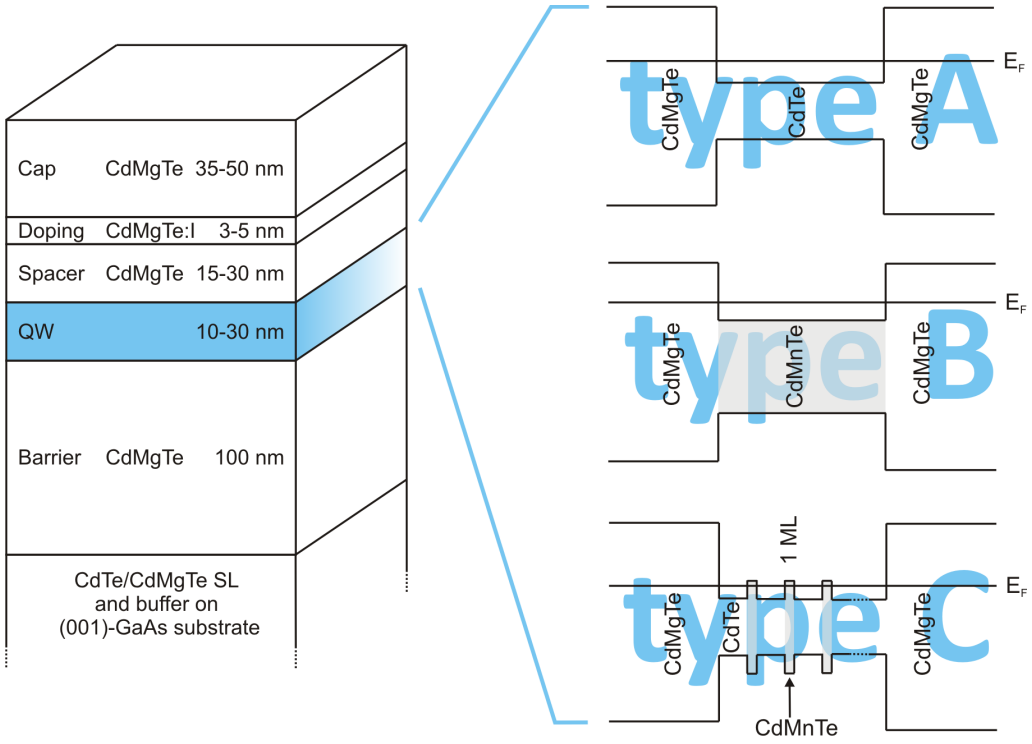

Figure 3.1: Left: Schematic structure of the wafers employed in this work. Barriers of CdMgTe confine the CdTe/CdMnTe QW to which electrons are supplied by iodine donors placed in the top barrier. Right: Prototypes for different QW designs. A nonmagnetic well simply is made of CdTe, magnetic manganese ions can be incorporated either homogeneously (type B) or by the digital alloy technique (type C). For details refer to the text.

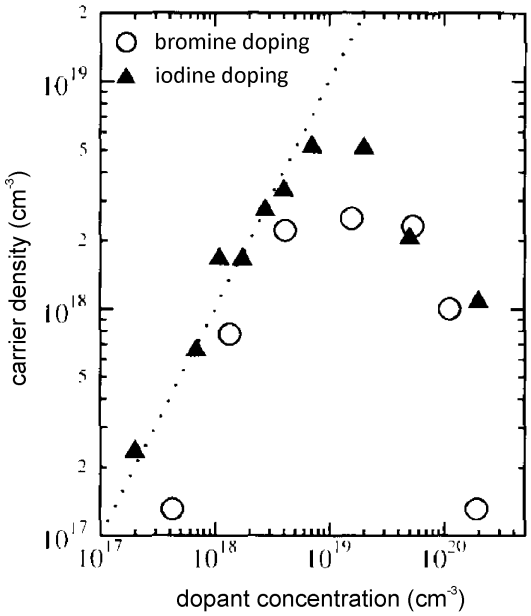

Figure 3.2: Carrier density of iodine or bromine doped CdTe layers as a function of dopant concentration ($T = 300$ K). The dotted line represents the ratio ionized/incorporated dopant concentration of one. For dopant concentrations exceeding $1 \cdot 10^{19}$ cm^{-3} the carrier density decreases due to the onset of selfcompensation. Adjusted from [74].

or CdMnTe. Details on the exact structure of the QW are described below. The QW is limited by a second CdMgTe barrier which additionally serves as a spacer, separating the n-type doped region (typically 5 nm) from the 2D electrons. The advantage of this so called *modulation remote doping* - invented in 1978 [21] - is an enhancement of electron mobility due to a reduced influence of ionized and neutral impurity scattering at donor atoms. A CdMgTe cap finishes the heterostructure; the magnesium content of barriers and cap is equal to the one of the buffer layers. $Cd_{1-y}Mg_yTe$ is ideally suited as a barrier and cap material for CdTe QWs, due to its wide and tunable bandgap (via Mg concentration y) and the small lattice mismatch between zincblende MgTe and CdTe of about 1% [7].
Commonly, indium has been used as a n-type dopant for CdTe and CdTe-based ternaries [73], but the success in In doping is depending critically on the growth parameters. For instance Cd-rich growth conditions have to be used to overcome the selfcompensation of the In dopants. Since the mid 1990s halogens like chlorine, bromine and iodine have been studied as an alternative way for n-type doping of CdTe [74,75], mainly because they require less strict growth conditions. Iodine has been proven to be the best halogen n-type dopant with the highest carrier density to be reached (see fig. 3.2). In a nowadays MBE process iodine is evaporated from a source containing solid ZnI_2 and forms hydrogen-like donors on Te sites with a donor ionization energy E_D of $15 - 50$ meV [75,76].
In contrast, holes can be introduced into a CdTe-based quantum structure by using nitrogen as a dopant [2,77].

The specific structure of each QW is based on one of the following three prototypes depicted on the right hand side of fig. 3.1; details on the different wafers employed

in this work are summarized in the appendix. In the case of nonmagnetic samples the QW simply is made of CdTe, embedded between CdMgTe barriers (type A, fig. 3.1).
The incorporation of manganese into the QW can be achieved in two different ways: On the one hand by growing a QW homogeneously of $Cd_{1-x}Mn_xTe$ (type B) where the concentration x can be adjusted via the temperature of the Mn cell in the MBE process. As the Mn ions - randomly distributed over Cd sites of the crystal lattice - constitute impurity atoms they introduce additional scattering centers to the electrons, thus degrading mobility [78]. In state of the art $Cd_{1-x}Mn_xTe$ samples the mobility decreases from $\mu \approx 500\,000$ cm^2/Vs for $x = 0$ to about 100 000 cm^2/Vs for $x = 0.01$. The second possibility of introducing Mn into the QW is the so called 'digital alloy technique' [56, 79] (type C in fig. 3.1): Evenly spaced monolayers of $Cd_{1-x}Mn_xTe$ are deposited during the growth of the CdTe QW. The advantage of this method is a reduced scattering of charge carriers as the Mn ions are restricted to discrete spatial regions, resulting in higher mobilities compared to a type B QW.
Another feature of the *digital alloy technique* (not utilized in this work) is the possibility to grow quantum structures with a confining potential different from the one of the common rectangular QW [80]. For instance CdTe/CdMnTe quantum wells with parabolic and half-parabolic shape have been reported [81, 82], employing Mn flux pulses of different duration. Thereby a variation in the width of the deposited CdMnTe layers could be achieved, resulting in a curvature of the confining potential. QWs with parabolic shape are for example interesting due to a strong enhancement of the exciton binding energy [81].
To obtain a detailed picture on the bandstructure in the QW regions, simulations have been performed using the *nextnano3* nanodevice simulator[1]. This software allows to fully quantum mechanically calculate the electronic structure of three-dimensional heterostructures, merely requiring input on materials, exact shape and doping. Results are shown in fig. 3.3 for a 30 nm wide CdMnTe and a 20 nm wide digital alloy CdMnTe QW.

3.1.2 Lithography and Structuring

All methods employed in fabricating the samples for later magnetotransport experiments are standard procedures in semiconductor wafer processing. Since they are discussed in detail by many authors, e.g. [83–85], this paragraph will only briefly introduce them. Primarily, features special for CdTe shall be paid attention to. A complete summary of the process parameters can be found in the appendix.

[1] *nextnano3*: Software for simulating electronic and optoelectronic semiconductor nanodevices and materials, www.nextnano.de .

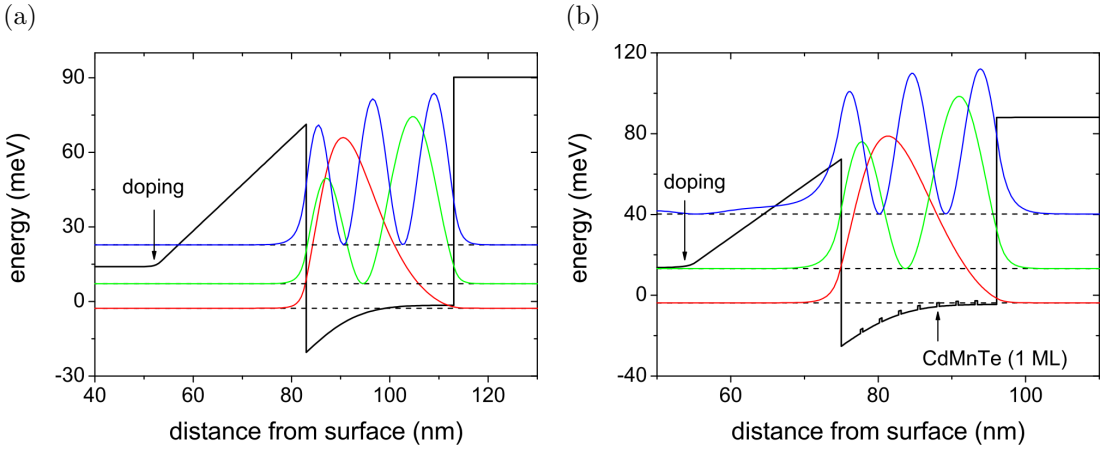

Figure 3.3: Conduction band energies and lowest energy levels with corresponding electron probability distribution for (a) a 30 nm wide CdMnTe QW and (b) a 20 nm wide digital alloy CdMnTe QW. The latter consists of evenly spaced CdMnTe monolayers embedded into a CdTe QW.

Optical and Electron Beam Lithography

Optical and e-beam lithography are based on the same principle: The sample is spin coated with a resist, afterwards certain regions are exposed either to UV light or an electron beam. By this the chemical nature of the exposed resist is changed and it can either be dissolved in or withstand a developer.
In the first instance the resolution of a lithographic process is limited by diffraction effects. Due to the long wavelength ($\approx$ 300 nm for UV light) a standard optical process is restricted to structure sizes of about 1 micron. In fact much smaller patterns are realized in semiconductor industry (down to 32 nm) but this is accompanied by huge technical efforts. On the contrary the de Broglie wave length of electrons is 50 pm at 25 kV acceleration voltage and structure sizes down to 10 nm can be achieved. However, the minimal linewidth to be obtained in an EBL process is less dependent on electron diffraction, but limited by scattering of electrons in the resist and substrate.
Besides a higher achievable resolution another advantage of EBL over optical lithography is its flexibility. Contrary to photolithography no masks are required, but the electron beam is scanned computer controlled over the sample. The system used here (Zeiss electron microscope and nanonic lithography unit) is discussed in detail in reference [86].
The structures defined in a lithographic process finally have to be transferred to the substrate. This is done either by etching or by deposition of a metal or insulator.

Etching

One typical application of etching is the definition of Hallbars. In principle, a substance can be etched employing two different methods: wet chemical or dry etching. CdTe for instance can be wet chemically etched using a bromine-ethyleneglycol solution [87]. The disadvantage of this technique however is its isotropic etch profile, resulting in an undercutting of the resist. Thus, chemical etching is no suitable means of transferring tiny patterns (below some microns), especially when the aspect ratio of the structure (ratio between its height and width) is greater than one.
To define small patterns one needs to utilize a dry etching process, such as Reactive Ion Etching (RIE) or Ion Milling. The latter method applies low energy (typically $100 - 1000$ eV) argon ions and has an extremely anisotropic etch profile. But with argon being a chemically inert gas the resulting etch rate is rather low. For this reason a RIE process employs gases able to react with the substrate thus combining higher etch rates with still very anisotropic etch profiles. According to reference [88] CdTe is be best etched by a mixture of methane and hydrogen with organo-metallic compounds and hydrides being formed as etch products [89]. Dry etching using methane as a process gas usually results in a presumably polymeric deposit on the sample surface which can easily be removed in an oxygen plasma [88]. A more detailed survey concerning the different etching techniques can be found in [83].

Sputtering and Lift-off

Metallic patterns are typically transferred to the substrate by evaporating or sputtering the desired material onto the lithographically shaped resist. A subsequent lift-off step in acetone removes the resist plus its metal cover; only the material deposited directly on the sample surface remains.
In a sputter process a solid target is bombarded with energetic particles (mainly Ar ions) causing atoms to be ejected from the target via collision cascades. If the pressure in the sputtering system is kept low enough those atoms can reach the sample, condense on it and form a thin film. Especially when a material is easily oxidized in air the quality of the deposited film is crucially dependent on the base pressure of the sputtering device. In this work a homemade system is employed which reaches a base pressure of $2 \cdot 10^{-10}$ mbar and exhibits magnetron sputtering sources.
One advantage of sputtering over thermal evaporation is that materials with high or undefined melting points (e.g. tantalum or ceramics) can easily be deposited with the first method while evaporating them thermally might be problematic or impossible. Moreover, sputter deposited films have a better adhesion to the substrate than evaporated ones.

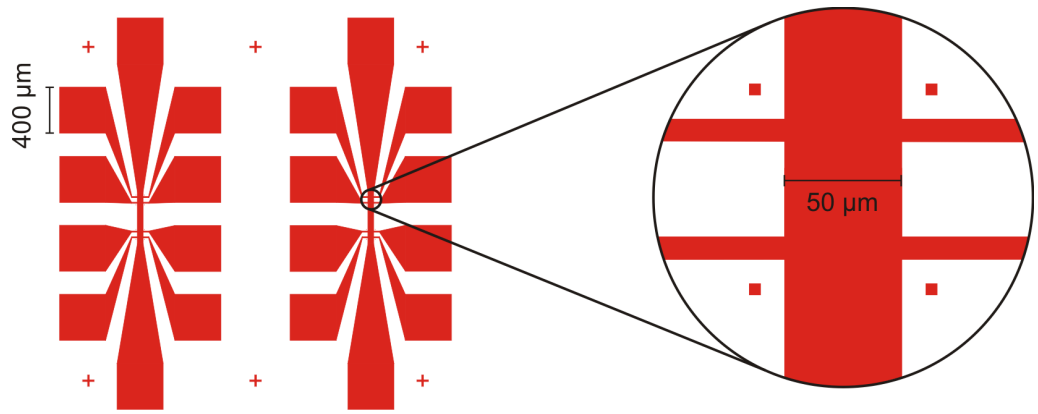

Figure 3.4: Optical mask used for the definition of the Hallbars. The potential probes feature contact pads of 400×400 μm^2, separated from one another by 200 μm. Each of the four active regions (enlargement) is surrounded by square alignment markers used for positioning control in an EBL process.

3.1.3 Sample Design

The following paragraphs introduce the layout of the FQHE samples as well as the one of the spin transistor devices and discuss characteristics of their fabrication. All samples are based on Hallbar structures. After cleaving the bare wafer into pieces of 4×4 mm^2 the Hallbars are defined photolithographically and transferred to the substrate in a RIE process. Here, the minimum etch depth is given by the distance between the 2DES and the sample surface.

Design of the Optical Mask

In order to cope with the special demands of this work a new optical mask (see fig. 3.4) has been prepared, fulfilling the below criteria:

- Potential probes with contact pads of 400×400 μm^2 and an inter-contact distance of 200 μm. Those dimensions are required for making ohmic contacts by hand (see section 3.1.4).
- Alignment markers for EBL. They serve the purpose of orientation and exact positioning in an EBL process (for defining the stripe patterns).
- Four active regions - each 50×50 μm^2 in size - with potential probes for measuring longitudinal and Hall resistance.

Altogether the new mask allows the definition of two Hallbars on a sample measuring 4×4 mm^2. This is the maximum size fitting into the chipcarriers serving as an interface between the specimens and the experimental probes. Despite the ohmic contacts consuming a huge part of the substrate both Hallbars yet exhibit a total of four active regions. Due to the large number of contacts associated to them, all of the 20 pins on the chipcarrier can be allocated.

FQHE Samples

The challenge of making a FQHE sample is less the fabrication itself but the growth of the wafer. High mobilities and low carrier densities are a prerequisite to observe fractional filling factors. As the accessible field range is limited (19 T in this work) a decreasing carrier density allows more and more FQH states to be studied.
The samples are prepared in the following way: After Hallbars have been defined as stated above, contacts - refer to section 3.1.4 - are made by annealing indium with a soldering iron. Electrical connections between the pins on the chipcarrier and the contacts of the sample are now to be set up. Usually a lead bonder is employed for that purpose but due to the elevated and soft indium contacts this is not possible here. Thus, gold wires (25 μm in diameter) are wetted with indium using a soldering iron and pressed on the contacts of the sample. Afterwards the specimen is glued into a chipcarrier utilizing PMMA[2] which has been proven to be a suitable adhesive at cryogenic temperatures. Within 10 minutes the solvent exhales from the PMMA and in a last step the gold wires can be attached to the pins of the chipcarrier. The sample is ready to be measured!
An alternative mode of sample fabrication omits the mesa etching process. Instead, a specimen of approximately 1.5×3 mm^2 is cleaved from the wafer and six contacts are positioned as a crude Hallbar around its edges. This approach allows a fast preparation of a new sample, however it has some disadvantages: As its dimensions (especially the distance between the voltage probes) cannot be determined precisely, material parameters like electron mobility are afflicted with large errors. If the Hall voltage probes should furthermore not be exactly face to face with each other - a situation hardly to avoid in completely handmade samples - the Hall plateaus exhibit wrong resistance values. For these reasons the initially described design should be the favored one.

Magnetically Modulated Samples - Spin Transistor Prototypes

One aim of this work is to enter the so far unexplored transport regime in which electrons in a CdMnTe QW are affected by an artificial spin superstructure (see chapter 5). Such arises in a periodic magnetic field that will be generated by means of micro- and nanopatterned ferromagnetic stripe arrays on top of the specimen. Characteristics of its fabrication will be discussed in the following.
Starting point again is a dry etched Hallbar mesa. The shape of the stripes is defined in an EBL positive process employing a two-layer PMMA resist. The lower layer of PMMA is chosen to be more sensitive to the electron beam than the

[2]PMMA: Polymethylmethacrylat. Typically used as an e-beam resist.

uppermost one, resulting in an undercut of the resist after development[3]. This undercut is an important aid when excess metal after the sputter process is to be removed in a lift-off step.
As discussed earlier, the design of the photomask provides four active regions on two Hallbars. This gives the possibility to have an unpatterned array for reference purposes and three arrays furnished with stripes of various periods within one single sample. Typically, stripe patterns of periods $a = 0.5$, 1 and 2 microns are fabricated where each stripe is $a/2$ wide (see fig. 3.5). Under ultra-high vacuum ($2 \cdot 10^{-10}$ mbar base pressure) 75 nm thick dysprosium or iron films are sputtered onto the shaped resist followed by a 6 nm aluminum cover to prevent them from oxidation in air [90]. Especially in the case of Dy very good vacuum conditions are required since this metal oxidizes extremely fast which strongly affects its magnetic properties. In a subsequent lift-off step the stripes are laid bare. Making ohmic contacts and finishing the specimen is done in the same way as in the case of the FQHE samples.

3.1.4 Ohmic Contacts

In order to perform transport experiments on the Hallbars fabricated, electrical contacts have to be established to the 2DES. Depositing a metal onto a semiconductor surface generally results in the formation of a Schottky barrier with nonlinear current-voltage characteristics. As such rectifying contacts are unfeasible for any AC measurement, many attempts have been made to understand the underlying physics of the methods used to obtain ohmic metal-semiconductor contacts [91, 92]. However several details still remain unclear for which reason contact technology rather is a technical art than a science.

Theoretical Considerations

In the 1930s Schottky published the first acceptable work describing the rectifying properties of a metal-semiconductor contact [93]. His diffusion theory postulates the existence of a space charge region giving rise to an electrostatic potential energy barrier (see fig. 3.6). Thermionic emission of carriers over this barrier explains the exponential current-voltage relationship of such a Schottky contact. In a first approximation the barrier height $E_b = \phi_m - \chi$ should be strongly dependent on the work function ϕ_m of the metal deposited, where χ is the electron affinity of the semiconductor ($\chi_{\mathrm{CdTe}} = 4.3$ eV). However this is only a good model for highly ionic materials, like most of the II-VI compound semiconductors (e.g. ZnS, ZnO). The barrier height for covalent semiconductors (e.g. Si, Ge, GaAs

[3] Typical developers for PMMA are isopropyl alcohol (IPA) or a mixture of methyl-isobutyl-ketone and IPA.

(a)

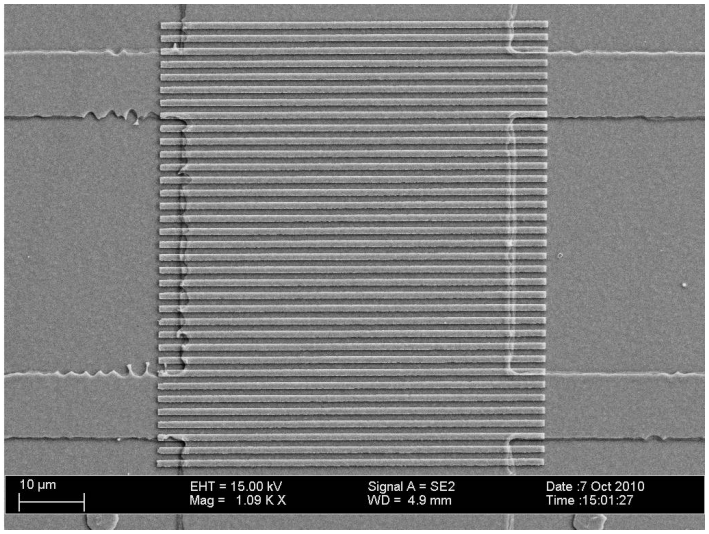

(b)

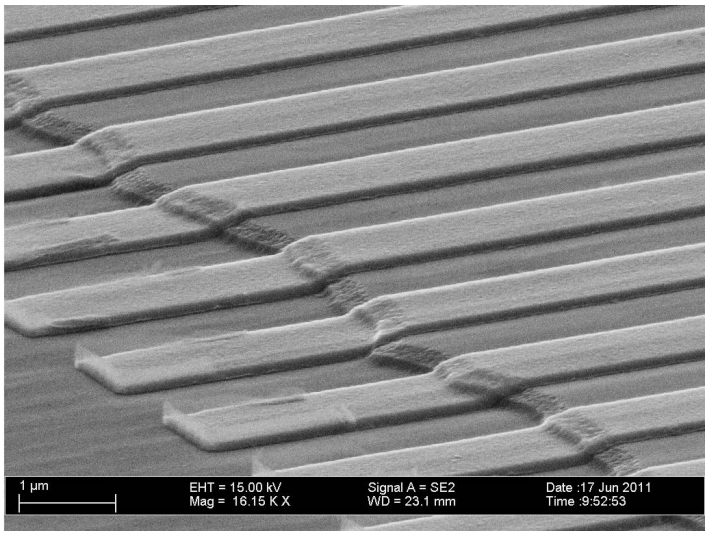

Figure 3.5: Electron micrographs showing a Hallbar active region furnished with a stripe pattern of period $a = 2$ μm. The stripes are made up of 75 nm Dy and a 6 nm Al cover as oxidation protection; their dimensions are 60 microns length by 1 micron width. (a) Topview, (b) lateral view under 30° angle.

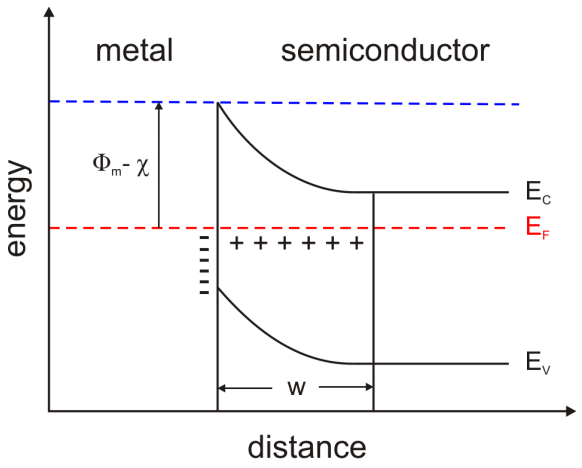

Figure 3.6: Schottky barrier at a metal-n-type semiconductor interface. The diffusion of electrons from the semiconductor to the metal forms a space charge region of width w. It is depleted of mobile carriers and situated in the semiconductor adjacent to the metal layer. In a fist approximation the barrier height $(\phi_m - \chi)$ is related to the work function ϕ_m of the metal deposited. Image force rounding of the barrier is neglected. For details refer to the text.

and CdTe) indeed is essentially independent of the metal used [92, 94] - in the case of CdTe, barriers typically have values of about 0.7 eV [94]. This observation is explained by the mechanism of Fermi level pinning [95, 96]: Imperfections or foreign atoms on the surface of a semiconductor give rise to charged surface states which constitute halffilled impurity levels in the band gap center. As was first proposed in reference [96] a high density of such surface states pins the Fermi level at the interface and therefore fixes the barrier height. When a metal-semiconductor contact is established, i.e. by gradually approaching both materials, the charged surface atoms largely affect the potential difference between the metal and the semiconductor, provided their density is high enough. In this case the height of the potential barrier formed is mainly determined by the surface charge and only merely by the work function of the metal. Exposing CdTe to air results in an approximately 15 Å thick oxide layer of TeO_2 [97, 98] which gives rise to a sufficiently large number of surface states causing the Fermi level to be pinned at the gap center, approximately 0.7 eV below the conduction band minimum.
As the height of the Schottky barrier cannot be influenced by the choice of the deposited material, the most common method to establish an ohmic contact is to place a metal layer in touch with a region of very high doping. The width of the barrier w is given by [92]

$$w \propto \frac{1}{\sqrt{N}} \tag{3.1}$$

where N is the donor concentration. With an increasing surface doping the barrier finally becomes thin enough so that conduction is dominated by quantum-mechanical tunneling instead of thermionic emission. One method to achieve this situation is the in-diffusion of a dopant contained in the contact material.
Ohmic contacts to n-type CdTe are most frequently achieved by means of depositing and annealing indium [99]. To reduce the contact resistivity first of all the surface oxide layer is removed by Ar ion sputtering or an HCl etch. Another possibility of making ohmic contacts is the in-situ growth of neodymium ($\phi_{\mathrm{Nd}} = 3.2$ eV)

on top of a n-CdTe wafer [100]. In this case no oxides are present on the surface resulting in an unpinned Fermi level. Thus the Schottky barrier height depends on the metal work function and due to $\phi_{\mathrm{Nd}} < \chi_{\mathrm{CdTe}}$ contacts feature a linear I-V characteristics.

Fabrication

Various methods of forming ohmic contacts to a CdTe 2DES have been investigated in a precursory work [101]; the only reliable one was demonstrated to be an annealing of tiny In flakes under forming gas atmosphere. However this technique only is applicable to samples with 100 Å wide QWs (as employed in the above cited work) and fails when contacts are to be made to wider wells. For these reasons a somewhat different approach is chosen here: The contact pads of the Hallbars are scratched with a needle to break up the oxide layer. Afterwards small pieces of indium are cut from a lager block and - utilizing a tweezers - pressed with their freshly cut surface on the sample. This fresh indium surface is a basic prerequisite for a successful fabrication of ohmic contacts, probably due to the absence of the In_2O_3 oxide layer. A soldering iron with a fine tip is used to anneal each of the indium contacts for approximately five seconds, resulting in linear current-voltage characteristics. At this juncture a good thermal contact to the soldering iron is crucial, hence its tip always has to be wetted with some indium. To further reduce heat losses, the sample is placed on a titanium base which has a factor of 10 lower heat conductivity ($\lambda_{\mathrm{Ti}} = 21.9\ \frac{\mathrm{W}}{\mathrm{m\,K}}$) compared to the usually employed aluminum one ($\lambda_{\mathrm{Al}} = 237\ \frac{\mathrm{W}}{\mathrm{m\,K}}$). Additionally, the titanium base is pivot-mounted to ensure a convenient sample handling and faster processing.
The quality of the contacts at room temperature is tested by means of a two-terminal measurement; good contacts are indicated by a linear current-voltage relationship and resistances (source-drain contacts plus 2DES) of 10 to 200 kΩ. These conditions are indeed necessary but not sufficient to characterize their behavior at cryogenic temperatures. The Quantum Hall regime yet provides a possibility to determine the magnitude of the contact resistances: A two-terminal measurement carried out on an arbitrary pair of contacts always yields a resistance of 25 812 kΩ at filling factor 1 (Landauer-Buttiker transport theory). In addition the experimentally determined value contains the resistances of contacts and wiring, the latter mainly being caused by the input lines of the experimental probe[4]. The contact resistances quantified with the help of this method range from 0 Ω to 150 Ω.

[4] 0.1 mm diameter constantan wire with 230 Ω each.

3.2 Experimental Setup

Since its invention in the mid 1960s at Leiden University the dilution refrigerator has become *the* standard instrument for obtaining temperatures in the range of 5 mK to 1 K. Bound to temperatures below 300 mK none of the experiments in this work could have been carried out without this refrigeration technology. Hence, this chapter will on the one hand introduce this essential cooling technique but on the other hand also focus on the measurement electronics employed. The best dilution refrigerator is of no avail when working with an improper measurement setup.

3.2.1 Dilution Refrigeration

Using pumped liquid He is the simplest method for obtaining temperatures below its normal boiling point of 4.2 K. But as the cooling power decays exponentially, external head loads limit the minimum achievable temperatures to 1.4 K when pumping ^{4}He and to 0.3 K in the case of ^{3}He, respectively. In contrast to using the latent heat of evaporation a new cooling mechanism based on the heat of mixing of the two helium isotopes was proposed in 1962 by London, Clarke and Mendoza [102] - heralding the era of the dilution refrigerator. Until then the only method of achieving low temperatures has been the adiabatic demagnetization of a paramagnetic salt.
All experiments were performed in a *Kelvinox TLM* toploading dilution refrigerator supplied by Oxford Instruments. Different from conventional systems the sample is inserted directly from above into the cold fridge by means of an experimental probe. This gives very quick experiment turnaround times as there is no need to remove the mixture during loading - inserting a sample and running to base temperature only lasts about six hours. The experimental probe is fitted with a motorized *in-situ* sample rotation stage to perform experiments in (tilted) fields generated by a 19 T superconducting magnet.
Many textbooks [103, 104] are devoted to a detailed description of dilution refrigerator operation principle for which reason it shall only be explained briefly here. The schematic of a ^{3}He-^{4}He dilution refrigerator is depicted in fig. 3.7. When a mixture of ^{3}He and ^{4}He is cooled below a temperature of 0.87 K the liquid will separate in two phases, one rich in ^{4}He (dilute phase) and the other rich in ^{3}He (concentrated phase). Due to its lower density the ^{3}He rich phase floats on top of the ^{4}He rich liquid. Even when the temperature approaches zero there is a finite solubility of 6.6% ^{3}He in the ^{4}He rich phase - being of utmost importance for the operation of a dilution refrigerator. The fact that the specific heat of a ^{3}He atom is larger in the dilute phase than in the concentrated phase leads to a cooling of the mixture if this atom is passed from the concentrated to the dilute phase. This transfer only is possible due to the finite solubility of ^{3}He in the dilute phase,

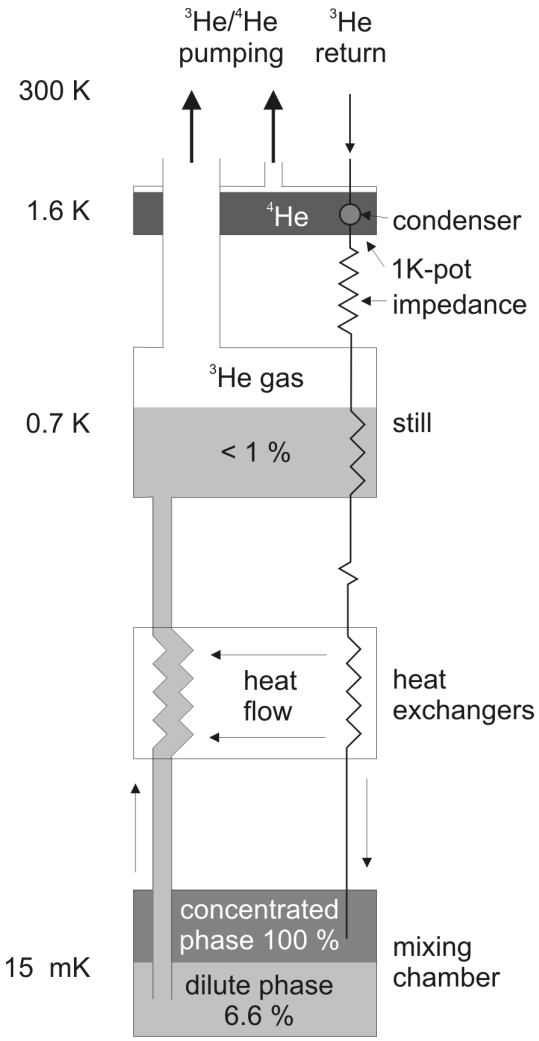

Figure 3.7: Schematic ^{3}He-^{4}He dilution refrigerator. ^{3}He entering the system is liquefied in the condenser placed inside a 1K-pot. The following flow impedance serves to establish sufficient pressure for the incoming ^{3}He to indeed condense at 1.6 K. After precooling to millikelvin temperatures in several heat exchangers it is fed into the concentrated phase (100% ^{3}He) of the mixing chamber. Evaporating ^{3}He from the still reduces its concentration below 1% thus creating an osmotic pressure which causes ^{3}He atoms to cross the phase boundary between concentrated and dilute phase (6.6% ^{3}He). As the specific heat of ^{3}He is larger in the dilute than in the concentrated phase this transition consumes entropy thus cooling the mixing chamber. The evaporated gas is pumped out of the fridge; after cleaning in cold traps it reenters the condenser.

even for $T \to 0$ K. In contrast to evaporative cooling, the cooling power $\dot{Q}$ at this juncture does not decrease exponentially but with the second power of T:

$$\dot{Q} \propto \dot{n}_3 T^2 \tag{3.2}$$

where $\dot{n}_3$ is the ^{3}He flow rate. In order to maintain a ^{3}He flow across the phase boundary the still is heated to a temperature of approximately 0.7 K. Due to the substantial difference in the vapor pressures of ^{4}He and ^{3}He (at the same T) only the latter isotope is evaporated from the still which allows the circulation of almost pure ^{3}He. As ^{3}He is evaporated, a concentration gradient develops, driving ^{3}He atoms from the mixing chamber into the still. This causes other atoms to cross the phase boundary in order to maintain a concentration of 6.6% ^{3}He in the dilute phase.
One of the biggest challenges in dilution refrigerator technology is returning the warm ^{3}He gas into the mixing chamber. First of all the gas is liquefied in a condenser, situated in a small pumped ^{4}He reservoir (1K-pot) with a temperature of roughly 1.6 K. Heat exchangers are then utilized to bring the temperature of the incoming ^{3}He as close to the mixing chamber temperature as possible by precooling it with the outstreaming liquid. This normally is achieved by using several heat exchangers between still and mixing chamber (counter-flow tube type, sintered metal powder). Their quality critically affects the performance of the dilution refrigerator. With ^{3}He returning to the mixing chamber a closed circuit is established allowing continuous cooling operation. The whole fridge displayed in fig. 3.7 is surrounded by a helium jacket, containing the magnet and serving as a supply for the 1K-pot.

3.2.2 Electronics

All experiments are based on the same principle: A constant current is driven through the sample and the voltage drops across various potential probes are recorded as a function of external magnetic field. All voltages are measured in a four-terminal setup employing separate pairs of current-carrying and voltage-sensing electrodes. The advantage of this technique stems from the fact that almost no current flows in the sense wires resulting in an extremely low voltage drop across them. Hence the sample resistance is probed independent of the sense wire resistances.
However, problems arise due to the required low temperatures. To avoid ohmic heating, low excitation currents - typically in the nanoamps range - have to be used, resulting in voltage drops of only several microvolts. Despite all shielding attempts (see below) those signals are obscured by noise sources - such as broadcast stations or power line noise - which may be many thousands of times larger. When the signal-to-noise ratio becomes much smaller than one, only lock-in technique allows to recover and amplify the original signal. For this purpose lock-in amplifiers

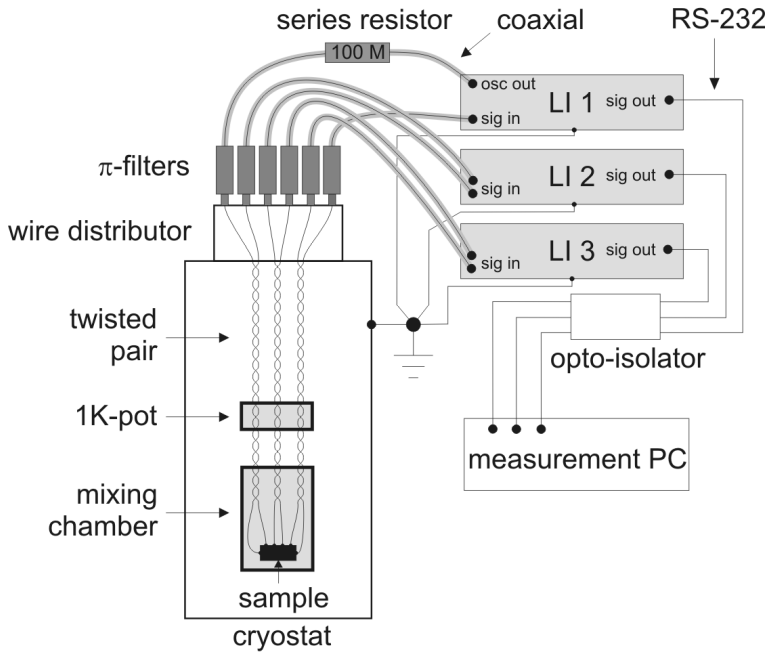

Figure 3.8: Wiring scheme of the experimental setup. Together with a high-value series resistor the internal oscillator of lock-in (LI) #1 serves as a current source. Voltage drops across the sample are probed with up to seven further LIs (only two more shown for simplicity). All input lines to the cryostat are fitted with π-filters to shield high frequency noise signals; for minimizing enclosed loop areas they are additionally set up in twisted pair design. Ground loops are eliminated by separating each instrument from the power line using isolating transformers and connecting it to a single point ground. Opto-isolators in the RS-232 data lines decouple the LIs from the measurement PC.

utilize AC signals and a technique known as phase-sensitive detection (PSD), to be discussed in detail in references [105, 106]. As a result, noise signals at frequencies other than a given reference frequency are rejected and do not affect the measurement. Nevertheless, proper shielding and grounding is necessary in order to achieve high sensitivities. If noise signals at the lock-in input amplification stage should be too large it may only be operated at low gain to avoid an overload anywhere in the instrument. In this case problems in signal processing at the PSD stage arise since the signal to recover finally is too weak.
Fig. 3.8 sketches the experimental setup: Four or eight digital lock-in amplifiers (Signal Recovery 7265) are employed, exhibiting an input noise of 5 nV/$\sqrt{\text{Hz}}$ at 1 kHz and an input resistance of 10 MΩ. The internal oscillator of lock-in #1 generates a sine wave (typically 1.0 V rms, 17.0 Hz) which in combination with a series resistor (100 MΩ) serves as a current source; all other lock-ins probe voltage drops across the various potential probes. The data are recorded by a homemade measurement software which additionally allows to operate the superconducting magnet power supply. Within the framework of this PhD thesis this software has been expanded to allow for both, automated alteration of the mixing chamber

temperature and automated stepper motor control. Additionally, all PCs can be remote operated via internet which enables the user to monitor relevant status parameters (e.g. He level, temperatures, magnet power supply output) by software or webcam and to interact with the setup from at home. These measures have led to a reduction of fridge idle time (mainly weekends and nights) by about 60%, hence drastically increasing output.
Low frequency noise in the measured signal is most commonly caused by ground loops since each instrument is connected to earth via protective ground and/or neutral lead. Alternating magnetic fields - mainly generated by 50 Hz power line currents - may induce a voltage in such a loop which adds to the original signal [107]. For these reasons all instruments are connected to a single point ground and are separated from the power line by an isolating transformer. Data lines (RS-232) are fitted with opto-isolators in order to decouple the instruments from each other and from the measurement computer. Furthermore, metal pumping lines are equipped with plastic connectors to interrupt the otherwise existing ground loop between pumps, cryostat and magnet power supply. For similar reasons all wiring between sample and lock-ins is set up in twisted pair design thus minimizing loops formed by the sense wires.
The temperatures of electronic system and mixing chamber may diverge strongly in the limit $T \to 0$ K due to electron-phonon coupling decreasing with T^5 [108]. Therefore, temperature equalization between substrate and electrons almost vanishes in the above limit and the latter may be heated up by external effects. Such can for instance be the measurement current[5] or high frequency radiation coupling into the cryostat. The latter has minor influence on the measurement accuracy since it is strongly attenuated by the lock-in amplifier due to the much lower frequency of the reference signal. However, such HF-radiation induces currents in the measurement circuit thus heating the electrons. For this reason all input lines to the experimental probe are fitted with π-filters[6] suppressing high frequency noise signals which allows the electronic system to stay in equilibrium with the mixing chamber temperature [109].

[5]For this reason an excitation current (few nanoamps) not heating the electrons was chosen. The effect of increasing current on the electronic temperature can easily be probed via the longitudinal resistance at a FQH state [63].
[6]Type: Tusonix 4201-001, 5500 pF.

4 Fractional Quantum Hall Effect in CdTe and CdMnTe

Since its discovery nearly 30 years ago [30], the fractional Quantum Hall effect (FQHE) has been observed in only a few (nonmagnetic) two-dimensional systems, though being predicted to be a material independent phenomenon. Typically, GaAs-based systems have been investigated in the early stages followed later by Si/SiGe [31], graphene [32, 33] and the oxide MgZnO/ZnO [34]. Only recently, sample quality of CdTe and CdMnTe two-dimensional electron systems could significantly be increased with carrier mobilities now approaching the level of 10^6 cm^2/Vs for CdTe and 500 000 cm^2/Vs for CdMnTe ($x \approx 0.01$) quantum wells, respectively. Their quality now is comparable to the first GaAs/AlGaAs heterostructures having displayed the fractional Quantum Hall effect, thus the possibility of getting an insight to the FQHE of (magnetic) II-VI based 2DESs has arisen for the very first time.
This chapter will only briefly address the observation of fractional Quantum Hall states in CdTe since the focus shall mainly be on the emergence of this effect in the semimagnetic material $Cd_{1-x}Mn_xTe$.

4.1 FQHE in CdTe

Certain fractional Quantum Hall (FQH) ground states of interacting charge carriers may be spin unpolarized, provided the Zeeman energy E_Z is sufficiently small. This is typically observed in GaAs-based systems where an increase in E_Z (by tilting the magnetic field at an angle θ to the sample plane normal) induces a change in the spin polarization of the ground state from unpolarized to fully spin-polarized. This transition becomes noticeable as a gap opening or closing and has been reported in GaAs for FQH states at filling factors $\nu = 4/3$, $8/5$, $2/3$ or $2/5$ [52, 110–112] as well as in a GaAs 2D hole gas [113]. These observations can elegantly be interpreted within the Composite Fermion (CF) approach to the FQHE [46] by introducing Zeeman energy-induced crossings between spin split Composite Fermion Landau Levels (CF-LLs) [53]. As already discussed in chapter 2.2.3, these crossings lead to possible changes of the spin configuration of the ground state. More recently, the FQHE was reported in a strained Si QW [114] - a system exhibiting spin-polarized fractional ground states due to its

much larger g-factor compared to GaAs ($g^*_{\mathrm{Si}} = -3.2$ vs. $g^*_{\mathrm{GaAs}} = -0.46$). The latter work addresses the interesting question of how the FQHE manifests itself in a 2D system with an intrinsically larger Zeeman energy. However, the valley degeneracy of Si is another degree of freedom that is suspected to interfere with the FQH physics.
Here, we study the evolution of FQH states in a QW structure based on the single-valley semiconductor CdTe - a system featuring a relatively large g-factor of $g^*_{\mathrm{CdTe}} = -1.67$. Transport measurements at mK temperatures reveal fully developed FQH states in the $n = 0$ LL at filling factors $\nu = 5/3$ and $4/3$, which to our knowledge constitutes the first observation of the FQHE in a II-VI semiconductor [36]. In addition, experiments in tilted magnetic fields of up to 28 T were performed in the group of M. Potemski at Grenoble High Magnetic Field Laboratory and show no significant changes of the energy gaps of both filling fractions investigated. This behavior is typical of spin-polarized ground states for which the lowest energy excitation does not involve a spin-flip and it is a direct consequence of the high intrinsic Zeeman energy of CdTe.

Experimental

The sample under investigation (sample F1, see appendix for details) is a modulation doped 20 nm wide CdTe QW structure, embedded between $\mathrm{Cd}_{1-y}\mathrm{Mg}_y\mathrm{Te}$ barriers ($y = 0.26$). Electrons are delivered by iodine donors which are introduced into the top barrier, 20 nm away from the QW. The specimen (approximately 1.5×3 mm^2 in size) features no etched mesa; instead six indium contacts are positioned around its edges to form a crude Hallbar. Experiments are performed in a dilution refrigerator equipped with an *in situ* sample rotation stage and a 28 T magnet. We explore transport coefficients either before or after illumination with a yellow LED using standard low-frequency lock-in technique with low excitation currents to avoid ohmic heating. The resulting electron densities before and after illumination are $3.80 \cdot 10^{15}$ m^{-2} and $4.53 \cdot 10^{15}$ m^{-2}, respectively, with the electron mobility peaking at 260 000 cm^2/Vs in the latter case.

Results and Discussion

Fig. 4.1 shows Hall and longitudinal resistances in perpendicular magnetic field after illumination. Pronounced FQH states with the longitudinal resistance ρ_{xx} approaching zero at lowest temperatures are observed at filling factors $\nu = 5/3$ and $4/3$. The role of illumination in improving the sample quality is critical, as the quantum lifetime τ_q extracted from low-field SdH oscillations (Dingle plots) [26, 115] is found to increase more than five times from 0.6 ps in the dark to 3.0(3) ps after illumination. This value of τ_q is comparable to the one observed in GaAs samples with electron mobilities of several millions, despite the moderate

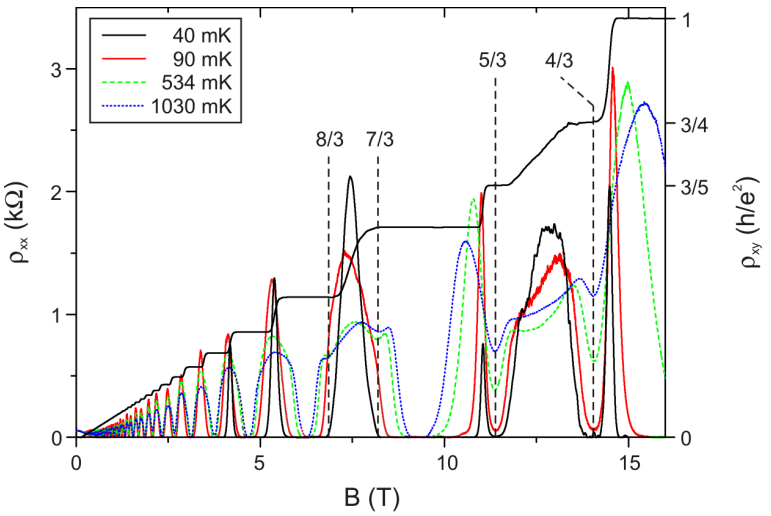

Figure 4.1: Observation of the fractional Quantum Hall effect in CdTe: Hall resistance ρ_{xy} and longitudinal resistance ρ_{xx} as a function of perpendicular magnetic field for different temperatures. Filling factors are indicated. Sample F1, after illumination.

mobility of 260 000 cm^2/Vs in our CdTe sample. The apparent contradiction stems from the fact that in high mobility GaAs samples the long-range scattering at remote donors is even more predominant and leads to a higher mobility for a comparable τ_q.

At very low temperatures a large number of electronic states is localized, thus leading to wide zero resistance states in the integer Quantum Hall effect (IQHE). In the first excited ($n = 1$) LL this prevents the observation of any signs of the FQHE. But upon increasing T the fraction of localized states is reduced and weak FQH minima become visible at filling factors $\nu = 8/3$ and $7/3$. These features persist up to temperatures of higher than 1 K, hence demonstrating the excellent quality achievable in CdTe-based QW devices now. Since the $\nu = 8/3$ and $7/3$ states can only be probed in an intermediate temperature regime we are not able to draw reliable conclusions on their angular gap evolution. Hence, the FQHE in the $n = 1$ LL will not be discussed here, the interested reader may refer to reference [36] for details.

Let us now focus on the FQHE in the $n = 0$ LL: Fig. 4.2a depicts the temperature dependence of the longitudinal resistance at $\nu = 5/3$ and $4/3$ as a function of inverse temperature after illumination. The corresponding energy gaps Δ_ν are commonly estimated by fitting the data points of these so called 'Arrhenius plots'. However, a simple extraction of the energy gap requires the observation of an expanded linear region - typically at least over one order of magnitude - where the condition for simple thermally activated transport

$$\rho_{xx} \propto \exp(-\Delta_\nu / 2k_B T) \tag{4.1}$$

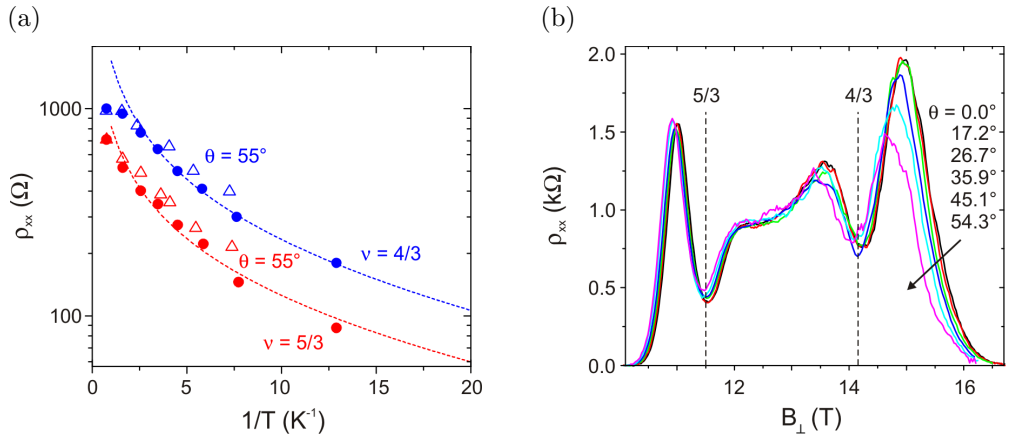

Figure 4.2: (a) Longitudinal resistance ρ_{xx} at $\nu = 5/3$ (red symbols) and $\nu = 4/3$ (blue symbols) as a function of inverse temperature at $\theta = 0°$ (circles) and $\theta = 55°$ (triangles). Sample F1, after illumination. Calculations of the thermally activated resistance account for the disorder broadening of the LLs and are shown by dashed lines. (b) Angular dependence of longitudinal resistance at filling factor $\nu = 5/3$ and $4/3$ at $T = 390$ mK. Increasing tilt angle θ is indicated by the arrow. Sample F1, after illumination.

holds. In above relation, k_B denotes Boltzmann's constant. Though, instead of a linear region in our data deviations occur at low temperatures. This non-thermally activated behavior is actually expected when disorder broadened LLs of Gaussian or Lorentzian shape are taken into account, rather than assuming δ-like levels. The effect of LL broadening becomes important when their width is no longer negligible in comparison to the gap size Δ_ν. To analyze our data we therefore use the model proposed in ref. [116] which includes a disorder-induced Gaussian broadening to calculate the temperature dependence of the resistance. Details on this model will be discussed in section 4.2. The results of our calculations are plotted as dashed lines in fig. 4.2a and show an excellent agreement with the experimental data points. From this model we estimate the gaps in the illuminated case to 3.0 K and 3.15 K for $\nu = 5/3$ and $\nu = 4/3$, respectively.
Activation data was also collected when tilting the magnetic field to an angle $\theta = 55°$ away from the sample plane normal (open triangles in fig. 4.2a), revealing a behavior similar to the one at $\theta = 0°$. In particular, the gap values at $\theta = 0°$ and $\theta = 55°$ are equal in case of both filling factors, $\nu = 5/3$ and $\nu = 4/3$. The qualitative angular evolution of these two FQH states can be inferred from fig. 4.2b, depicting ρ_{xx} as a function of perpendicular magnetic field $B_\perp = B \cdot \cos\theta$ for various tilt angles θ. Over the entire angular range studied ($0° < \theta < 55°$) the resistance values at $\nu = 5/3$ and $4/3$ only show a very weak variation, demonstrating that the associated gaps do not significantly change. As will be outlined below, such behavior is expected for fully spin-polarized FQH ground states with excitations which do not involve a spin-flip.
The situation can qualitatively be understood within the Composite Fermion

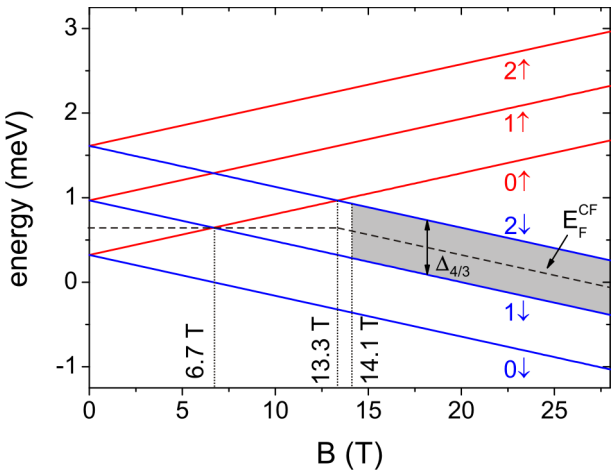

Figure 4.3: CF-LL fan diagram for the $\nu = 4/3$ ($\nu_{CF} = 2$) state in CdTe. Via tilting the sample the gap $\Delta_{4/3}$ can experimentally be probed within the gray shaded region. Due to the large CdTe g-factor, excitations do not involve a spin-flip within this magnetic field range and the gap exhibits no angular dependency. E_F^{CF} denotes the CF Fermi energy at $\nu = 4/3$.

model, where the FQHE of electrons is mapped onto the IQHE of CFs. Around filling factor $\nu = 3/2$ these CFs are quantized into CF-LLs by the perpendicular component of the effective magnetic field [53]

$$B_{\mathit{eff}} = 3(B_\perp - B_{3/2}), \tag{4.2}$$

where $B_\perp = B \cdot \cos\theta$ denotes the perpendicular magnetic field component at tilt angle θ and $B_{3/2}$ the perpendicular magnetic field at $\nu = 3/2$. In this case the $\nu = 5/3$, respectively $\nu = 4/3$ FQHE of electrons is the $\nu_{CF} = 1$ or rather $\nu_{CF} = 2$ IQHE of CFs. The CF-LL spectrum of a non-magnetic semiconductor (e.g. CdTe, GaAs) has already been discussed in chapter 2.2.3 and is given by the following equation:

$$E_{N,\uparrow\downarrow} = \left(N + \frac{1}{2}\right)\hbar\omega_c^{CF} \pm \frac{1}{2}g^*\mu_B B, \tag{4.3}$$

with

$$\omega_c^{CF} = \frac{e|B_{\mathit{eff}}|}{m_{CF}}. \tag{4.4}$$

Here, N denotes the CF-LL index and g^* the g-factor of CFs in CdTe which we assume to be equal to the one of electrons [53, 117], i.e. $g^* = -1.67$.
With an experimental estimate of the CF mass [118]

$$m_{CF} = (0.51 + 0.074\,|B_{\mathit{eff}}|)\,m_0 \tag{4.5}$$

we may plot in fig. 4.3 the arrangement of CF-LLs for the $\nu = 4/3$ (i.e. $\nu_{CF} = 2$) state in our sample as a function of total magnetic field B. While the ground state at $\nu_{CF} = 2$ initially is formed by the $(0,\uparrow)$ and $(0,\downarrow)$ CF levels this situation is altered at sufficiently high fields[1]: In case $B > 6.7$ T, the ground state is formed

[1]Note that the magnetic field values discussed here are by a factor of two larger than the ones given in reference [36]. This is due to an incorrect computation in ref. [36], which however does not affect the conclusions drawn there.

by the $(1,\downarrow)$ and $(0,\downarrow)$ levels and therefore is spin-polarized. At higher fields ($B > 13.3$ T) - where excitations do not involve a spin-flip anymore - the gap becomes independent of the total field, i.e. independent of tilt angle. Since for our sample the perpendicular magnetic field at $\nu = 4/3$, $B_{4/3} = 14.1$ T, already is larger than 13.3 T and tilting the specimen shifts states to even higher fields, the gap does not depend on tilt angle for the entire magnetic field range investigated (14 T $< B <$ 25 T). In a similar fashion the gap of the $\nu = 5/3$ state can be shown to be independent of tilt angle, provided $B > 5.5$ T. We note here that the CF energy gaps used in above calculations are by a factor of about two larger than the experimentally measured activation gaps, hence the transition to a spin-polarized ground state with no spin-reversed excitations should occur at an even smaller magnetic field. The discrepancy in the measured and calculated gap energies is related to deviations of the CF mass in our sample from the one extracted in ref. [118]. These deviations stem from disorder effects, from a different LL mixing due to the larger effective mass of CdTe and from finite thickness effects that we do not consider here.

Chapter Summary

We demonstrate that the quality of CdTe-based 2DESs has by now reached a level making the observation of pronounced FQH states in the vicinity of filling factor $\nu = 3/2$ possible. Our results hence constitute the very first observation of the FQHE in a II-VI semiconductor. The physics of the studied fractional states at $\nu = 5/3$ and $\nu = 4/3$ is strongly influenced by the large intrinsic Zeeman energy of CdTe, resulting in a complete spin polarization of the corresponding ground states. The observation of angular independent activation gaps for both fractions $\nu = 5/3$ and $\nu = 4/3$ is in good agreement with predictions of the CF model.

4.2 FQHE in CdMnTe

A fundamental asset of CdTe-based quantum structures is the possibility to easily incorporate magnetic manganese ions, hence making this material system ideally suited for the search for fractional states in a diluted magnetic semiconductor (DMS). $Cd_{1-x}Mn_xTe$ is one to the most thoroughly investigated members of the DMS class with all its spin-dependent properties being strongly enhanced due to spin exchange interaction between mobile charge carriers and localized magnetic moments (*s-d* exchange, see sec. 2.3). However, the FQHE has not been observed in any diluted magnetic semiconductor so far, raising the question if magnetic impurities inhibit the formation of FQH states.
In this chapter, we report on the observation of FQH states in the lowest Landau level (LL) of a two-dimensional electron system formed in a high quality

$Cd_{1-x}Mn_xTe$ quantum well. This constitutes the first experimental demonstration of this effect in a diluted magnetic semiconductor ever. We prove that *s-d* exchange interaction crucially affects the properties of FQH ground states when the Zeeman energy E_Z is changed by tilting the sample.

4.2.1 Setup and Material Parameters

This introductory chapter will briefly illustrate the experimental setup as well as the basic design of the sample utilized for the FQHE studies. The main focus though, shall be on the one hand on the effect of finite voltmeter input impedances on Quantum Hall measurements, possibly leading to false residual minima in longitudinal resistance. On the other hand we elaborate on a method for the experimental determination of the manganese concentration in $Cd_{1-x}Mn_xTe$ QWs.

Sample and Setup

The sample employed in this study (sample F2, see appendix for details) is a modulation doped $Cd_{1-x}Mn_xTe$ QW structure with a homogenous manganese concentration of $x = 0.0024(2)$, estimated from a detailed analysis of the ρ_{xx} beating pattern at low magnetic fields (see paragraph below and sec. 2.3). The 30 nm wide QW is embedded between $Cd_{1-y}Mg_yTe$ barriers ($y = 0.29$), electrons are delivered by iodine donors introduced 30 nm apart into the top barrier. To perform magnetotransport experiments, six indium contacts are - similar to specimen F1 - positioned as a crude Hallbar around the edges of the sample (approx. 1.5×3 mm^2 in size).
The specimen is cooled down in a toploading ^{3}He/^{4}He dilution refrigerator (accessible temperature range 15 mK to 1 K) equipped with a 19 T superconducting magnet and an *in situ* sample rotation stage. Both, the sample and a calibrated RuO_2 resistor thermometer are immersed in the liquid of the mixture. Resistances are probed either before or after illumination with a yellow LED using standard low-frequency lock-in technique with low excitation currents (typically 10 nA) to avoid ohmic heating. The resulting electron densities before and after illumination are $1.86 \cdot 10^{11}$ cm^{-2} and $3.95 \cdot 10^{11}$ cm^{-2}, respectively with the mobility peaking at 115 000 cm^2/Vs in the illuminated case.

In the Quantum Hall effect regime the finite lock-in input resistance (typically 10 MΩ for digital lock-in amplifiers) is known to lead to nonzero minima in longitudinal resistance ρ_{xx} (see fig. 4.4a) [119]. A similar behavior is usually expected in case of parallel conduction in the doping layer. However, this can be ruled out here as the finite ρ_{xx} minima are *not* measured at *all* voltage probes and they further disappear either upon reversing the magnetic field direction or swapping source and drain contacts. In a standard four-point resistance measurement

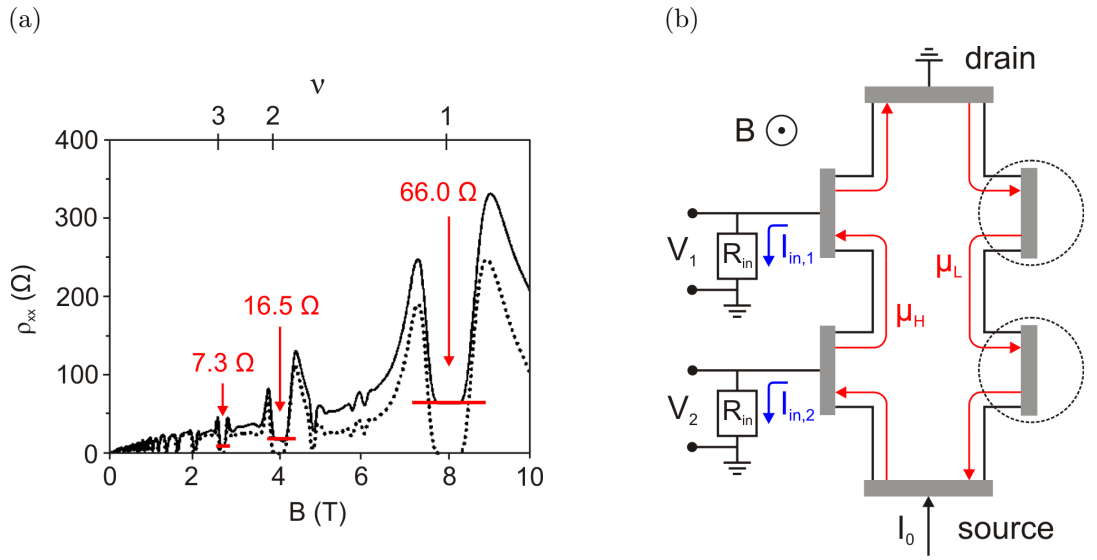

Figure 4.4: (a) Longitudinal resistance ρ_{xx} measured on opposite sides of a Hallbar. In contrast to the dotted trace, the solid one features nonzero SdH minima which are attributed to the finite input resistance of the employed voltmeter. (b) Schematic Hallbar geometry at filling factor $\nu = 1$: A current I_0 is driven from source to drain (grounded), edge channels (at potential μ_H or μ_L) are indicated by red arrows. The circled voltage probes allow to measure proper $\rho_{xx} = 0$ minima (see panel (a), dotted trace), whereas the opposing ones give rise to a residual resistance. In the latter case the finite input resistance R_{in} of the voltmeter probing the voltage drop $V_{xx} = V_1 - V_2$ allows currents $I_{in,1}$ and $I_{in,2}$ to flow to ground. For details refer to the text. Both figures adjusted from [119].

current is typically fed into the Hallbar via the source contact, with the drain set to ground. If the sample is at an integer or fractional filling factor ν (i.e. a SdH minimum is observed) then the edge channels on one side of the Hallbar have the same potential as the current source (high potential side, μ_H) while the ones on the opposite side are on ground potential (low potential side, μ_L) (see fig. 4.4b). Connecting a voltmeter with finite input resistance to a pair of voltage probes located on the high potential side causes a current to flow through the voltmeter to ground. This gives rise to a residual resistance of [119]

$$\rho_{xx} = \frac{\rho_{xy}}{R_{in}}, \tag{4.6}$$

where, R_{in} is the input resistance of the voltmeter and $\rho_{xy} = h/\nu e^2$. In contrast, the nonzero ρ_{xx} minima are not observed when probing the voltage on the low potential side of the Hallbar.
The occurrence of finite ρ_{xx} minima may easily be circumvented by means of:

- Switching the polarity of the magnetic field.
- Swapping source and drain contacts.
- Using voltage probes on the opposite side of the specimen.

The first two methods simply exchange the high and low potential side of the sample. All measurements presented in this PhD thesis utilize one of the above possibilities to eliminate residual minima resistances.

Determination of Manganese Content

When dealing with diluted magnetic semiconductors one of the most important material parameters to know is the concentration x of manganese ions incorporated into the QW structure. In case of $Cd_{1-x}Mn_xTe$ this parameter can easily be extracted from the temperature shift of either the Quantum Hall Ferromagnet spike position [23] or the beating pattern [59] which both arise due to *s-d* exchange interaction between mobile charge carriers and localized magnetic moments (see section 2.3). Hence, the observation of either effect is a direct proof of the presence of magnetic impurities in or close to the QW. We will focus here on the determination of x from the beating pattern at low magnetic fields - the other method may be inferred from reference [23].
Fig. 4.5a depicts the low-field longitudinal resistance ρ_{xx} of sample F2, clearly evidencing a beating pattern with seven distinct nodes (filled triangles). Those nodes occur whenever the condition [59]

$$E_Z = \left(\tilde{n} + \frac{1}{2}\right)\hbar\omega_c, \quad \text{with} \quad \tilde{n} = 0, 1, 2, \dots \quad , \tag{4.7}$$

is met. Here, E_Z denotes the Zeeman splitting of a DMS,

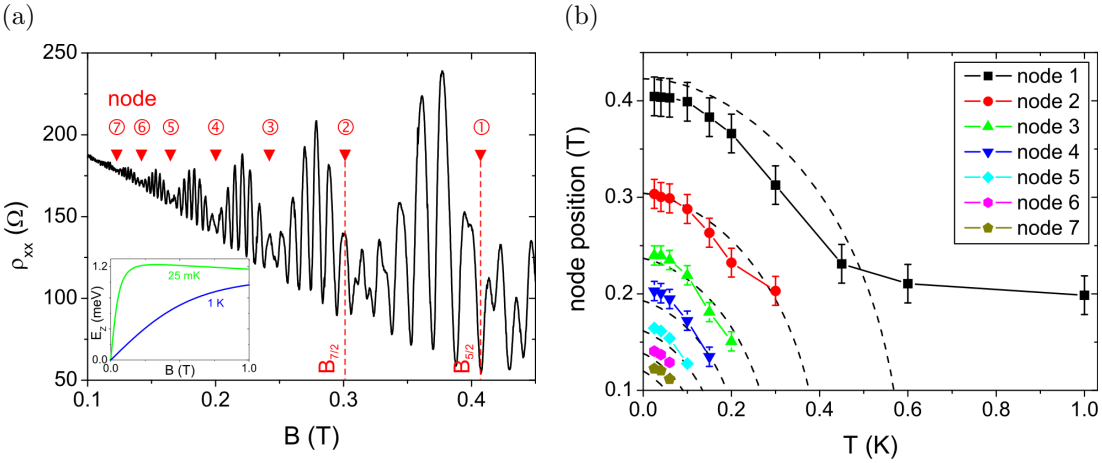

Figure 4.5: (a) Low-field magnetoresistance ρ_{xx} of sample F2 after illumination; $T = 25$ mK. Due to the presence of manganese in the QW a distinct beating pattern with nodes (filled triangles) emerges. The latter are located at magnetic fields $B_{5/2}, B_{7/2}$, etc. Inset: Zeeman splitting E_Z as function of magnetic field, calculated for sample F2 using $x = 0.0024$. At low temperatures and within the field range of the beating pattern ($0.1\ \mathrm{T} \leq B \leq 1\ \mathrm{T}$) E_Z can be regarded as a constant. (b) Temperature dependence of the node positions. The dashed lines are fits to the experimental data suggesting a manganese concentration of $x = 0.0024$ for sample F2. Error bars are either indicated or are of the size of the symbols. Deviations from theoretical predictions occur at high temperatures (node 1) and for nodes at very low fields (nodes 6+7).

$$E_Z = g^* \mu_B B + \alpha N_0 x_{\mathit{eff}} S \mathcal{B}_S \left(\frac{g \mu_B S B}{k_B T_{\mathit{eff}}} \right), \tag{4.8}$$

with all constants having already been defined in the context of eq. 2.33 and eq. 1.5. Knowing the node positions $B_{\tilde{n}+1/2}$, we can extract the manganese concentration x according to ref. [59]: In case of low temperatures and low magnetic fields ($0.1\ \mathrm{T} \leq B \leq 1\ \mathrm{T}$) the Zeeman splitting is saturated and rather constant (see inset of fig. 4.5a). Therefore, we may neglect the small intrinsic contribution $g^* \mu_B B$ and roughly approximate E_Z by

$$E_Z = \Delta_{\mathit{exch}} = \text{const.} \quad , \tag{4.9}$$

where $\Delta_{\mathit{exch}} = \alpha N_0 x_{\mathit{eff}} S$. Then, the node condition, eq. 4.7, leads to a simple series of nodes at positions

$$\frac{B_{\tilde{n}+1/2}}{B_{\tilde{m}+1/2}} = \frac{\tilde{m} + 1/2}{\tilde{n} + 1/2} = \frac{2\tilde{n} + 3}{2\tilde{n} + 1}, \quad \text{with} \quad \tilde{m} = \tilde{n} + 1. \tag{4.10}$$

In experiment (fig. 4.5a) we observe consecutive nodes at lowest temperature for instance at $B = 0.41$ T (node 1) and $B = 0.30$ T (node 2) fulfilling the relation

$$\frac{0.41\ \mathrm{T}}{0.30\ \mathrm{T}} \approx \frac{7}{5}. \tag{4.11}$$

Hence, $B_{5/2} = 0.41$ T, $B_{7/2} = 0.30$ T, $B_{9/2} = 0.24$ T, ... Using the data gathered for node 1 ($\tilde{n} = 2$, $B_{5/2} = 0.41$ T at $T = 25$ mK) and the CdTe effective mass $m^* = 0.1\ m_0$, eq. 4.7 yields

$$\Delta_{exch} = \left(\tilde{n} + \frac{1}{2}\right) \hbar\omega_c = 1.19 \text{ meV}. \tag{4.12}$$

This allows us to estimate the effective manganese concentration to $x_{\mathit{eff}} = 0.0022$ from which we deduce the effective temperature $T_{\mathit{eff}} = (T + 0.0776)$ K (via equations 1.12 and 1.10).
The knowledge of T_{eff} now allows us to perform a more detailed evaluation by considering the full Zeeman splitting as given by eq. 4.8. Hence, the node condition 4.7 now reads

$$\left(\tilde{n} + \frac{1}{2}\right) \hbar\omega_c = g^* \mu_B B + \alpha N_0 x_{\mathit{eff}} S \mathcal{B}_S \left(\frac{g\mu_B SB}{k_B T_{\mathit{eff}}}\right). \tag{4.13}$$

With x_{eff} and T_{eff} being the only unknowns, above equation can be solved for a specific node (for instance: node 1, $\tilde{n} = 2$) to obtain a theoretical estimate of its magnetic field position. We may use $T_{\mathit{eff}} = (T + 0.0776)$ K from our above rough approach and consider x_{eff} as a fitting parameter to adjust all theoretical node positions to the measured ones. Our data is best reproduced when assuming $x_{\mathit{eff}} = 0.0023$ (see fig. 4.5b) which via eq. 1.12 corresponds to $x = 0.0024$. These values yield $\Delta_{exch} = 1.30$ meV, differing by only 9% from our rough approach.

Chapter Summary

Quantum Hall measurements are typically interfered by the finite input resistances of the employed voltmeters. This might lead to nonzero minima in longitudinal resistance which can be mistaken as a result of parallel conduction in the doping layer of the device. The residual minima resistances become the more pronounced the lower the input impedance R_{in} of the voltmeter is. Typically, digital lock-in amplifiers are used in QHE measurements, but these devices feature the lowest values of R_{in} and therefore give rise to large undesirable effects. In order to circumvent this nonzero resistance problem, experiments need to be carefully set-up using one of the methods discussed.
The presence of manganese ions in a CdTe QW becomes evident upon the emergence of a beating pattern of the longitudinal resistance at low magnetic fields. A precise analysis of the positions where the SdH oscillations are damped (node positions) allows to extract the concentration x of magnetic impurities embedded in the quantum structure. Since this value is important to calculate the size of the exchange-enhanced electron g-factor (needed for later analysis), we discuss here a simplified as well as an accurate method to determine the manganese content. Both procedures lead to very similar results differing only by about 10%.

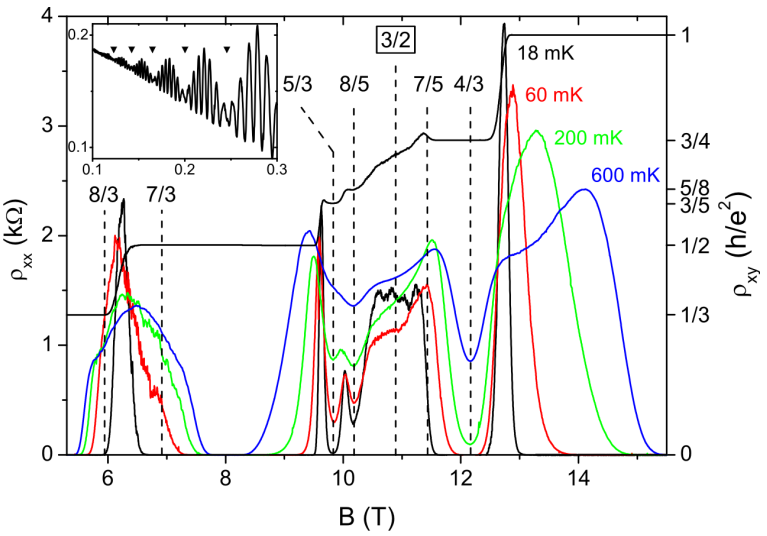

Figure 4.6: Hall resistance ρ_{xy} and longitudinal resistance ρ_{xx} of sample F2 at various temperatures after illumination. Magnetic field is applied perpendicular to the sample plane, filling factors are indicated. The inset depicts the ρ_{xx} trace at $T = 18$ mK in the limit of low magnetic fields. The presence of manganese in the QW is evidenced by the emergence of a distinct beating pattern with nodes (filled triangles).

4.2.2 Composite Fermions in a Diluted Magnetic Semiconductor

We demonstrate the emergence of FQH states in a $Cd_{1-x}Mn_xTe$ QW despite the presence of magnetic impurities. The latter - by giving rise to *s-d* exchange interaction - strongly affect the angular evolution of activation energy gaps which we explain within an extended Composite Fermion model.
In particular we have investigated the angular dependence of activation energy gaps in $Cd_{1-x}Mn_xTe$ in the vicinity of filling factor $\nu = 3/2$. By fitting our extended CF model to the observed gap openings and closings, we are able to gain information about the CF masses and *s-d* exchange constants for the investigated fractional states.

Experimental Findings

Fig. 4.6 depicts the longitudinal resistance ρ_{xx} of sample F2 in perpendicular magnetic field for selected temperatures after illumination with a yellow LED. Pronounced minima corresponding to filling factors $\nu = 5/3$, $8/5$ and $4/3$ emerge in the lowest ($n = 0$) LL at low temperatures in the vicinity of $\nu = 3/2$. In contrast, the $\nu = 7/5$ minimum is not observable in the perpendicular magnetic field configuration. Similar to the case of CdTe (see section 4.1 and ref. [36]) the $\nu = 5/2$ state ($n = 1$ LL) is not observable over the entire temperature range

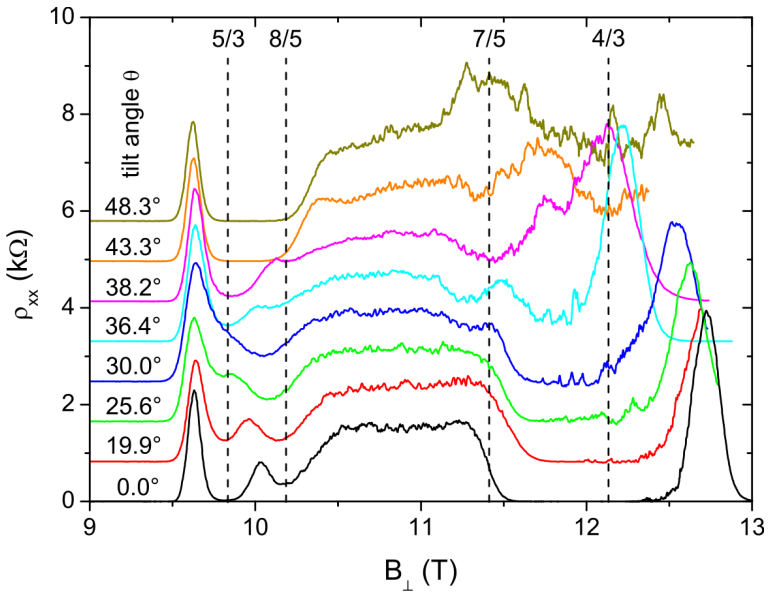

Figure 4.7: Angular dependence of longitudinal magnetoresistance ρ_{xx} of sample F2 in the vicinity of $\nu = 3/2$. Data are recorded at a temperature of $T = 25$ mK, after illumination of the specimen. Filling factors are indicated, traces are shifted for clarity, except for the lowest one. $B_\perp = B\cos\theta$ is the perpendicular magnetic field at angle θ. When tilting the sample, the minima corresponding to filling factors $\nu = 5/3$, $4/3$ and $8/5$ initially disappear before they eventually reemerge at larger angles. On the contrary, the $\nu = 7/5$ minimum only is observable at intermediate tilt angles around $\theta = 38°$.

studied, while weak FQH minima at $\nu = 7/3$ and $8/3$ emerge at temperatures above $T \approx 450$ mK. As these states are masked by the integer Quantum Hall effect at lowest temperatures and further display an analogous characteristics as their counterparts in CdTe we will not discuss details here. Note that the presence of manganese in the QW is evidenced by the presence of a distinct beating pattern with nodes at low magnetic fields [59] (see inset of fig. 4.6 and fig. 4.5a).
Illuminating the sample is found to be of utmost importance for the observation of the FQHE: Despite a doubling of the transport lifetime $\tau = \mu m^*/e$, the quantum lifetime τ_q extracted from low-field SdH oscillations (Dingle plots) [26, 115] increases by more than five times from 0.58 ps in the dark to 3.0(3) ps, a value comparable to the one of high mobility GaAs samples. Indeed, FQH states in $Cd_{1-x}Mn_xTe$ are observed in post-illumination data only.
The FQHE in the lowest LL is studied in more detail in fig. 4.7, depicting a set of angular dependent magnetoresistance traces recorded at a temperature of $T = 25$ mK. Here, the sample is tilted to an angle θ which yields the perpendicular magnetic field as $B_\perp = B \cdot \cos\theta$. In the vicinity of $\nu = 3/2$ a rather complex angular dependence appears in the ρ_{xx} traces, i.e. upon tilting the sample, minima disappear and reappear in a certain fashion. The $\nu = 5/3$ minimum for instance starts to weaken continuously as soon as the sample is tilted away from the initial $\theta = 0°$ position, completely vanishes at roughly $\theta = 30°$ and reemerges upon

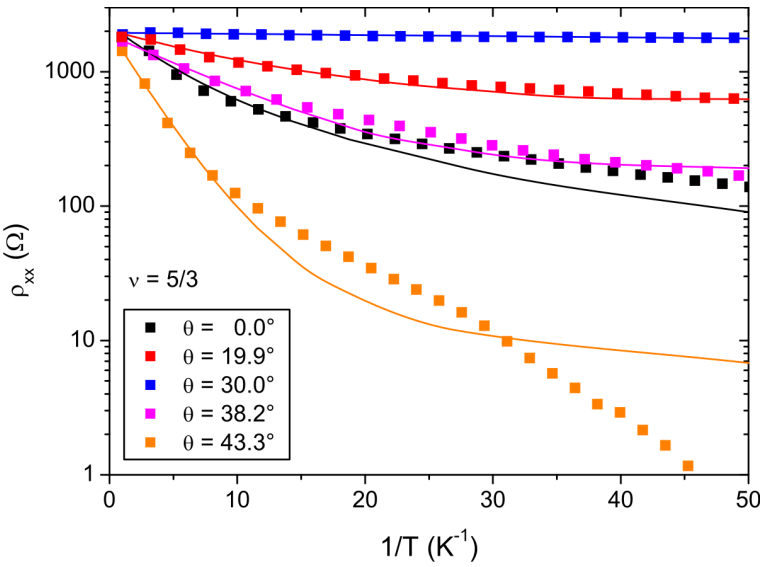

Figure 4.8: Semi-log plot showing activation data measured at filling factor $\nu = 5/3$ for various tilt angles θ. Sample F2, after illumination. Deviations from simple thermally activated transport, i.e. a linear $1/T$ behavior, are expected in case of disorder-broadened LLs. Solid lines are fits to the data using a model that considers such level broadening (see text for details).

further tilt. This behavior is rather similar to the one observed at $\nu = 8/5$ and $4/3$. In contrast, the $\nu = 7/5$ minimum is absent in perpendicular magnetic fields but becomes noticeable around $\theta = 38°$.

To check the validity of our observations we performed angular dependent *activation energy measurements*, as exemplified in fig. 4.8 for the case of the $\nu = 5/3$ state. In an activation measurement the longitudinal resistance ρ_{xx} at a particular LL filling is recorded as a function of temperature, typically while the dilution refrigerator cools from 1 K to base temperature. As will be discussed below, the $\rho_{xx}(T)$ trace then allows to extract the size of the activation energy gap Δ_ν. In order to obtain the angular gap evolution this procedure is repeated for various tilt angles while keeping $B_\perp$ unchanged.

Since our data (fig. 4.8) in general strongly deviates from the linear $1/T$ behavior expected for simple thermally activated transport (see discussion in section 4.1), activation gaps Δ_ν are obtained by fitting the $\rho_{xx}(T)$ traces with a model that considers disorder-broadened LLs of Gaussian shape. Level broadening indeed becomes important when being comparable to the gap Δ_ν and may not be neglected [116].

Let us develop here an analytical expression of the expected $\rho_{xx}(T)$ behavior in the presence of Gaussian LL broadening: Starting point of our considerations is the number of electrons n_e in the highest occupied LL

$$n_e = \int_{E_F}^{\infty} f(E)\, D(E)\, \mathrm{d}E, \tag{4.14}$$

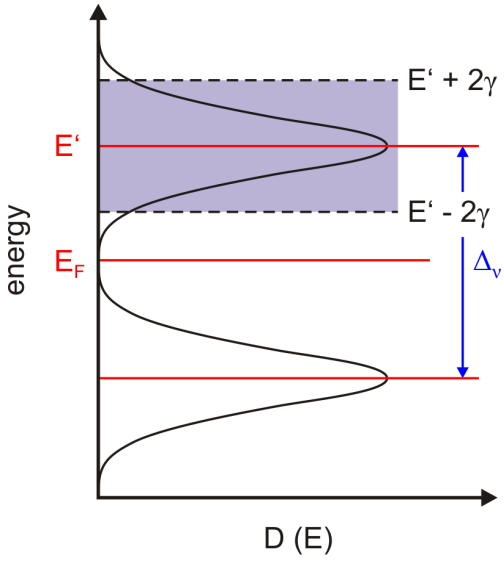

Figure 4.9: Density of states $D(E)$ of a 2DES exhibiting Gaussian LL broadening. Only extended states are shown here, which lie close to the center of the levels and - distinct from the localized ones - account for only a small amount of the total number of states. The center of the upper level is located at energy E'. Integration in eq. 4.14 is limited to states that lie within the shaded range $(E' \pm 2\gamma)$, where 4γ roughly is the width of the extended states region. E_F denotes the Fermi energy and Δ_ν the activation gap.

where E_F is the Fermi energy, $D(E)$ the density of states of the upper level and

$$f(E) = \frac{1}{1 + \exp((E - E_F)/k_B T)} \tag{4.15}$$

the Fermi-Dirac distribution function.
In a Hallbar geometry the measured longitudinal resistance ρ_{xx} is related to the conductivity via

$$\sigma_{xx} = \frac{\rho_{xx}}{\rho_{xx}^2 + \rho_{xy}^2}. \tag{4.16}$$

At a ρ_{xx} minimum - where $\rho_{xx} \ll \rho_{xy}$ holds - above relation simplifies to

$$\sigma_{xx} \approx \frac{\rho_{xx}}{\rho_{xy}^2} \propto \rho_{xx}. \tag{4.17}$$

When assuming that $\sigma_{xx} \propto n_e$ [116], equation 4.14 yields the law of simple thermally activated transport (i.e. eq. 4.1), given that LLs are δ-like and the relation $\Delta_\nu \gg k_B T$ holds.
In case of LLs of Gaussian shape[2] however, the density of states of the upper level is given by

$$D(E) = \frac{1}{\gamma\sqrt{2\pi}} \exp\left(-\frac{(E - E')^2}{2\gamma^2}\right), \tag{4.18}$$

where 4γ roughly is the width of the extended states region and E' the energy of the level center (see fig. 4.9). Assuming $\Delta_\nu \gg k_B T$ and carrying out the integration in eq. 4.14 only over states that lie within $\pm 2\gamma$ away from the level

[2]The LL width and shape discussed here is those of the extended state region which lies close to the level center.

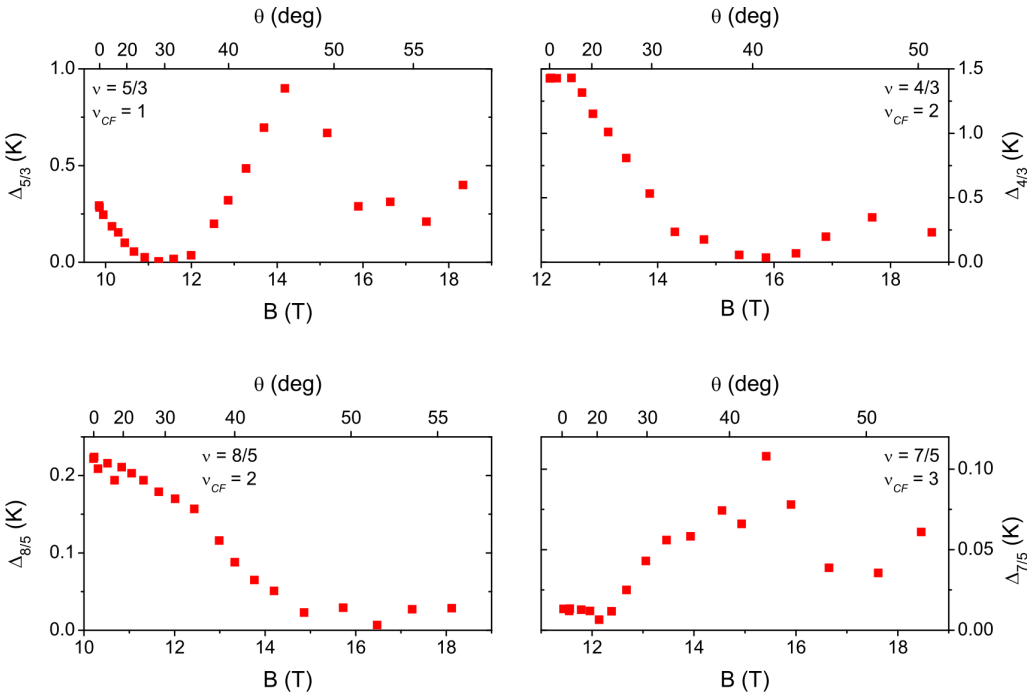

Figure 4.10: Experimentally determined angular gap evolution of FQH states around $\nu = 3/2$. $B = B_\perp / \cos\theta$ is the total magnetic field at angle θ. The maximum gap size is about 1 K in the case of $\nu = 5/3$ and $4/3$ but at least by a factor of 5 lower for states at filling factor $8/5$ and $7/5$, respectively.

center (this covers about 95% of the total number of states of this level) we expect the longitudinal resistance at a FQH minimum to evolve as

$$\rho_{xx}(T) \propto \sigma_{xx}(T) \approx \frac{1}{2} \exp\left(-\Delta_\nu / 2k_B T\right) \exp\left(\gamma^2 / 2k_B^2 T^2\right) \times \\ \times \left[\operatorname{erf}\left(\frac{2k_B T - \gamma}{\sqrt{2} k_B T}\right) + \operatorname{erf}\left(\frac{2k_B T + \gamma}{\sqrt{2} k_B T}\right)\right] \quad . \quad (4.19)$$

Here, $\operatorname{erf}(z)$ is the error function which may be expanded in a Taylor series as

$$\operatorname{erf}(z) = \frac{2}{\sqrt{\pi}} \left(z - \frac{z^3}{3} + \frac{z^5}{10} - \frac{z^7}{42} + \frac{z^9}{216} - \ldots\right). \quad (4.20)$$

Consequently, equation 4.19 allows us to fit activation data (see fig. 4.8) and hence to determine the angular dependence of energy gaps $\Delta_\nu(B)$.
Results are summarized in fig. 4.10 for filling factors $\nu = 5/3$, $8/5$, $7/5$ and $4/3$. Let us for example focus on the $\nu = 5/3$ state: The gap $\Delta_{5/3}$ starts to close when the total magnetic field B is increased by tilting the sample, vanishes completely at around 11.3 T ($\theta \approx 30°$), opens again and reaches a maximal value at 14.1 T ($\theta \approx 45°$). This behavior is in line with the observed disappearance and reappearance of the $\nu = 5/3$ minimum presented in fig. 4.7 (see discussion above).

All other fractions (i.e. $\nu = 4/3$, 8/5 and 7/5) show a similar good agreement between fig. 4.7 and the closing and opening of the activation energy gap. In accordance with experiments on other two-dimensional systems, e.g. GaAs and Si [54, 120], higher order fractions feature reduced energy gaps - in the case of sample F2 roughly $0.01 - 0.2$ K for the fifths fractions, compared to $1.0 - 1.5$ K for the thirds.

Composite Fermion-based Model

In order to *qualitatively* retrace the observed gap behavior we expand the Composite Fermion model (see chapter 2.2.3 and ref. [46]) to also cover the characteristics of diluted magnetic semiconductors. The CF approach maps the FQHE of electrons onto the IQHE of non-interacting composite fermionic particles. Around $\nu = 3/2$ these particles encounter an effective magnetic field

$$B_{\mathit{eff}} = 3(B_\perp - B_{3/2}), \tag{4.21}$$

where $B_{3/2}$ is the perpendicular field component at $\nu = 3/2$ [53]. They are consequently quantized into CF-LLs, separated by a cyclotron-like energy gap of $\hbar\omega_c^{CF}$, with $\omega_c^{CF} = e|B_{\mathit{eff}}|/m_{CF}$ and the CF effective mass m_{CF}. As the CF cyclotron gap arises due to Coulomb interaction between the electrons, it scales as $\hbar\omega_c^{CF} \propto \sqrt{B_\perp}$. The CF mass consequently must be proportional to $\sqrt{B_\perp}$,

$$m_{CF} = C_\nu m_0 \sqrt{B_\perp}. \tag{4.22}$$

Here, m_0 is the bare electron mass and C_ν a constant being material and filling factor dependent [117].
In the vicinity of $\nu = 3/2$ the CF filling factor ν_{CF} is related to the one of electrons via

$$\nu = (3\nu_{CF} \pm 2)/(2\nu_{CF} \pm 1). \tag{4.23}$$

In close analogy to the LL spectrum of electrons in a DMS (see eq. 2.33) we propose the CF energy spectrum in $Cd_{1-x}Mn_xTe$ to be given by

$$\begin{aligned} E_{N,\uparrow\downarrow} &= \left(N + \frac{1}{2}\right)\hbar\omega_c^{CF} \pm \\ &\pm \frac{1}{2}\left[g^*\mu_B B + \alpha N_0 x_{\mathit{eff}} S\mathcal{B}_S\left(\frac{Sg\mu_B B}{k_B T_{\mathit{eff}}}\right)\right]. \end{aligned} \tag{4.24}$$

Here, the upper spin branch of the lowest ($n = 0$) electronic LL is chosen as energy zero. The first term in eq. 4.24 represents the cyclotron energy of a CF in the N^{th} CF-LL while the second one is the Zeeman splitting in the presence of magnetic impurities [1]. The Zeeman term has two contributions: Its first part corresponds to the well known level splitting due to the external magnetic

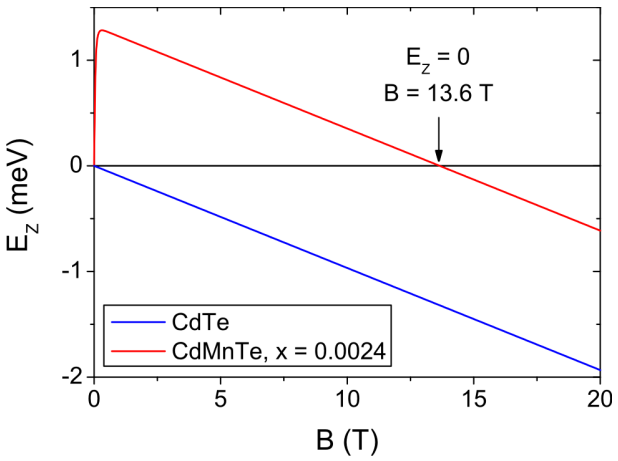

Figure 4.11: Zeeman splitting E_Z in CdTe and CdMnTe at $T = 25$ mK. In the latter case the exchange contribution to the spin splitting accounts for the steep rise of E_Z at low magnetic fields before saturating at $B > 1$ T. The decrease at yet higher fields is then caused by the Zeeman term $-g^*\mu_B B$. Depending on temperature T and manganese content x, E_Z reverses its sign at a specific field value. For sample F2 ($x = 0.0024$) the sign reversal occurs around $B = 13.6$ T at low temperatures.

field B, where g^* is the g-factor of CFs. The second component arises due to exchange interaction between CFs and manganese spins as described by the s-d exchange constant αN_0 and the Brillouin function $\mathcal{B}_S$ in which $S = 5/2$ and $g = 2$. Antiferromagnetic interactions between manganese spins in $Cd_{1-x}Mn_xTe$ lead to a reduction of their overall magnetization which is taken into account by the functions $x_{\mathit{eff}}(x) < x$ and $T_{\mathit{eff}}(x) > T$ [1] (see chapters 2.3 and 1.3).
According to section 4.2.1, the following parameters hold for sample F2 (including the uncertainty of their estimation): $x_{\mathit{eff}} = 0.0023(2)$ and $T_{\mathit{eff}} = T + 84(7)\,\mathrm{mK}$. Since for these values the Brillouin function in eq. 4.24 is already saturated for magnetic fields exceeding 1 T at low temperatures, the exchange contribution to the spin splitting hence gives a large constant background in the relevant field range between 10 T and 19 T (see fig 4.11).
In order to model the angular gap evolution of the FQH states around $\nu = 3/2$ we may adjust the CF-LL schemes suggested by eq. 4.24 to the experimental data by using g^*, m_{CF} and αN_0 as fitting parameters. The individual contributions of these three parameters to the gap are identified as follows:

- The CF mass m_{CF} adjusts the cyclotron gap $\hbar\omega_c^{CF} = \hbar e|B_{\mathit{eff}}|/m_{CF}$ and thus defines the maximum gap size possible. Note that $B_\perp$ (and hence B_{eff}) is fixed for each filling factor; consequently the cyclotron gap only depends on m_{CF}.

- As a result of the CF spin, crossings of (spin split) CF-LLs may occur which cause gap openings and closings as the Zeeman energy is tuned by tilting the sample. Since the exchange contribution to the spin splitting is saturated in the relevant field range, the CF g-factor g^* therefore is directly related to the slopes of the $\Delta_\nu(B)$ traces via $|\partial\Delta_\nu/\partial B| = |g^*\mu_B|$.

- The s-d exchange constant αN_0 defines the crossing points of different CF-LLs, i.e. positions where the gap vanishes or reaches a maximum.

Since the magnitude of the gap is usually strongly influenced by, for instance disorder effects, the slopes $\partial\Delta_\nu/\partial B$ do not represent a real physical quantity anymore. We hence use $g^* = -1.67$ in our model as it is a reasonable assumption that the CF g-factor is roughly equal to the one of electrons [53].
In fig. 4.12 we plot experimental and modeled gaps Δ_ν together with the corresponding CF-LL fan diagram as a function of total magnetic field. As an example, let us focus on the $\nu = 5/3$ ($\nu_{CF} = 1$) state: Basically, the gap $\Delta_{5/3}$ (gray shaded region) is given by the energy difference between the two CF-LLs lying closest to the Fermi energy E_F^{CF}. The CF-LL fan chart does however only correctly reproduce the $\Delta_{5/3}$ minimum at roughly 11.3 T and its maximum at about 14.1 T when setting the *s-d* exchange constant to $\alpha N_0 = 184(8)$ meV in this case. Our simple model yields a rather good agreement with experiment. The angular gap dependence can be qualitatively retraced, not only for $\nu = 5/3$ but for each fractional state (see fig. 4.12). Let us stress here that this would not have been possible when neglecting the exchange contribution to the Zeeman splitting. Similar to electrons, CFs in a DMS are therefore subject to *s-d* exchange interaction.
The αN_0 parameters obtained from above model are summarized in table 4.1 below: We find a rather filling factor independent exchange constant with an average of $\alpha N_0 = 186(22)$ meV, deviating by only 15% from 220 meV, the value measured for electrons in $Cd_{1-x}Mn_xTe$ [1]. This deviation is crucially linked to the 10% uncertainty in determining x_{eff}. In the particular case of $\nu = 5/3$ we note that the gap $\Delta_{5/3}$ closes at the same magnetic field ($B = 11.3$ T) as the Zeeman splitting vanishes due to a crossing of the $0\uparrow$ and $0\downarrow$ CF-LLs (see fig. 4.12). This level crossing is expected to occur at $B = 13.6$ T in case of $\alpha N_0 = 220$ meV. A 10% uncertainty in the Mn concentration largely accounts for this difference and also for the deviation of αN_0 from the value of electrons.
Activation gaps are overestimated by our model by a factor of roughly $2 - 3$ in case of $\nu = 5/3$ and $4/3$ and by about $30 - 40$ times in case of $\nu = 7/5$ and $8/5$, respectively[3]. In general, gaps are overestimated in theoretical models when disorder effects, Landau level mixing and the finite thickness correction are neglected. Assuming the impact of those effects on CdTe to be similar to GaAs, we may explain the differences between model and experiment: The finite thickness correction is especially important in the case of wide systems, such as our QW of width $w = 30$ nm. Strong corrections arise in GaAs if $w/l_B > 1$, where $l_B = \sqrt{\hbar/eB_\perp}$ is the magnetic length. Hence, we expect a gap reduction by at least a factor of two [121, 122] as for the density of our sample $w/l_B \approx 4$. In addition to this, disorder has been shown to diminish gaps in GaAs even more drastically [123], with the mobility of our sample suggesting a nearly ten-fold decrease. Finally, Landau level mixing effects reduce gaps by at least 10% in

[3] As a consequence of the strong overestimation of the energy gaps Δ_ν, this simple approach cannot account for the correct CF masses.

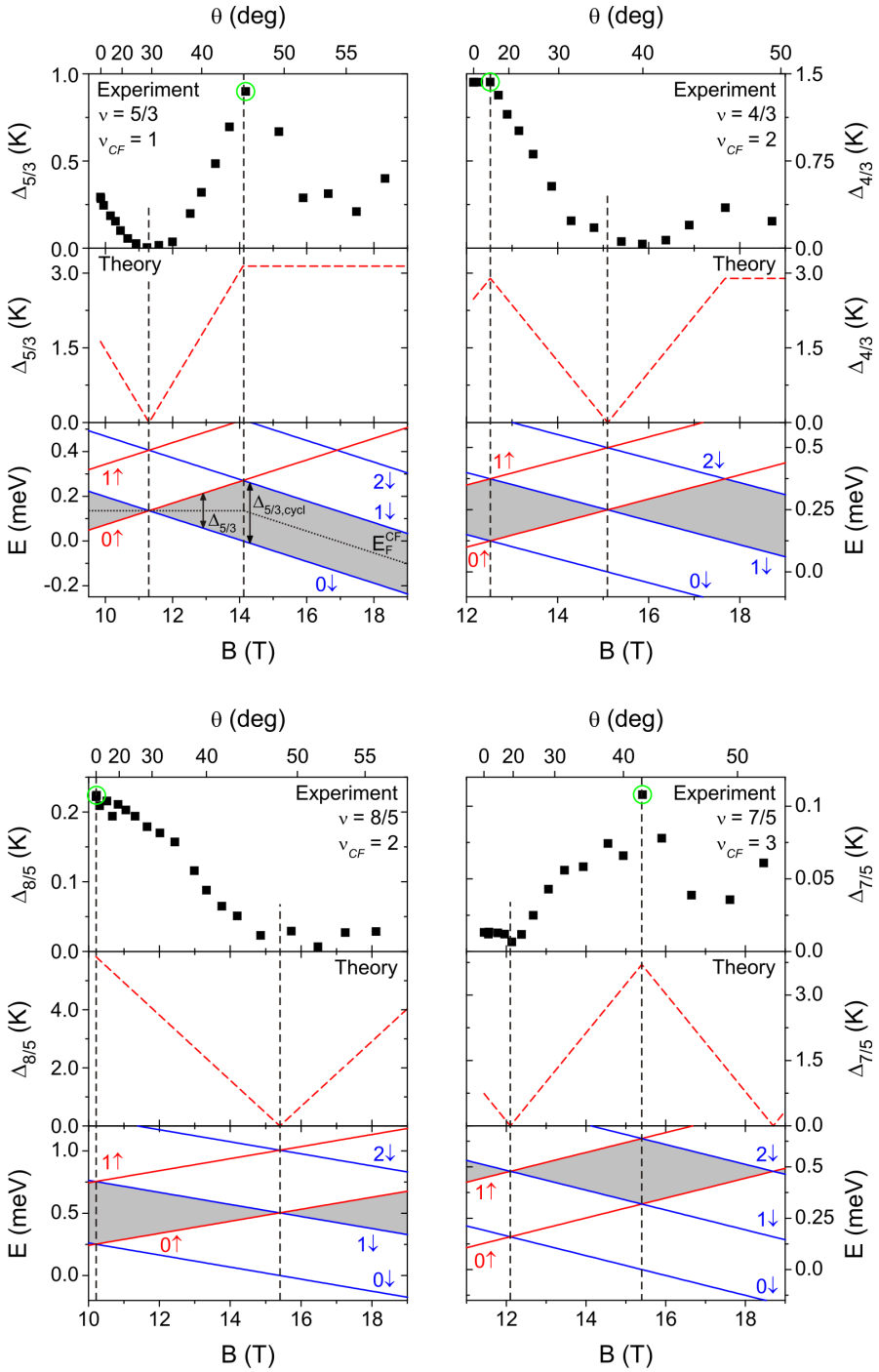

Figure 4.12: Measured (top panels) and calculated (middle panels) activation energy gaps Δ_ν as function of total magnetic field B. Corresponding tilt angles θ are given on the top axes. The modeled gaps are estimated from the CF-LL schemes (lowermost panels) which are adjusted to fit the extreme points of the experimental data (indicated by dashed vertical lines). Here, the gaps (gray shaded regions) are defined by the CF-LLs lying closest to the Fermi energy E_F^{CF} (dotted line), as exemplified for the $\nu = 5/3$ state. Circled data points refer to pure CF cyclotron gaps $\Delta_{\nu,cycl}$ (see text for details). Sample F2, after illumination.

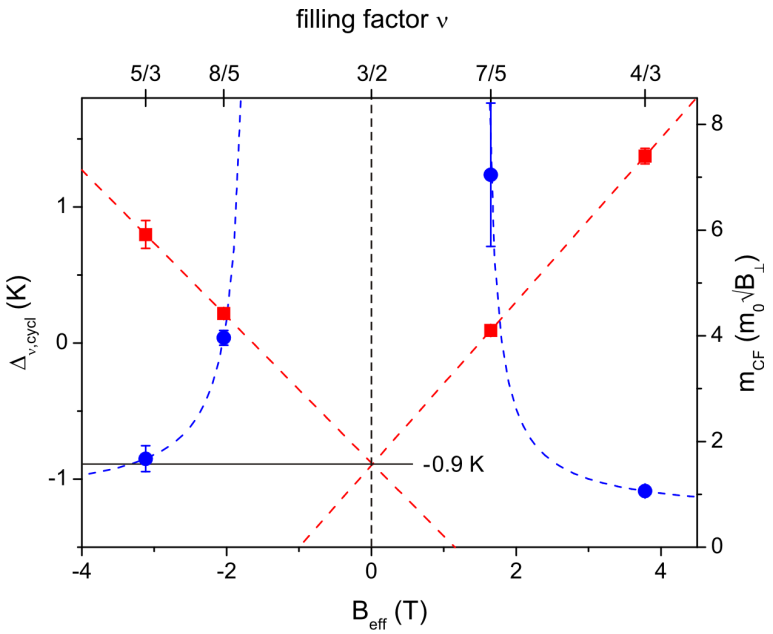

Figure 4.13: CF cyclotron gaps $\Delta_{\nu,cycl}$ (red symbols) as function of effective magnetic field B_{eff} in sample F2 around $\nu = 3/2$. Gaps are linear in B_{eff} with an intercept of roughly -0.9 K at $B_{\mathit{eff}} = 0$ T; this value reflects the CF-LL broadening. The CF masses m_{CF} (blue symbols) derived from these experimental gap values drastically increase as the filling factor approaches $\nu = 3/2$. The dashed blue lines show the expected mass increase. Error bars are either indicated or are of the size of the symbols.

GaAs [124]. Another effect caused by the finite QW width (neglected in our model) is the gap suppression as the filling factor approaches $\nu = 3/2$ [125], i.e. the experimentally observed smaller activation gaps of the fifths fractions compared to the thirds.

Despite all the limitations of our model, the qualitative knowledge of the CF-LL fan charts allows us to yield a *quantitatively accurate* description of the CF masses. We may use the fan charts to extract the pure CF cyclotron gaps $\Delta_{\nu,cycl}$ at filling factor ν from the $\Delta_\nu(B)$ plots (see highlighted data points in fig. 4.12). According to eq. 4.24 the cyclotron contribution to the CF gap is given by

$$\Delta_{\nu,cycl} = \hbar\omega_c^{CF} = \frac{\hbar e}{C_\nu m_0 \sqrt{B_\perp}}\, 3(B_\perp - B_{3/2}). \tag{4.25}$$

In fig. 4.13 we plot the so determined $\Delta_{\nu,cycl}$ values as a function of CF effective field B_{eff}. As expected, the cyclotron gaps are linear in B_{eff} with a negative intercept at $\nu = 3/2$, suggesting a CF-LL broadening of $\Gamma' = 0.9(2)$ K [126]. This value is in reasonable agreement with $\Gamma = \hbar/2\tau_q = 1.3(1)$ K extracted from low-field Shubnikov-de Haas oscillations. A plot similar to fig. 4.13 was already proposed in an investigation of high mobility GaAs systems. In their work, Du *et al.* [126] showed that the slope of $\Delta_{\nu,cycl}(B_{\mathit{eff}})$ increases with increasing mobility; the rather 'flat' characteristics of the cyclotron gaps in our sample

Table 4.1: Experimental *s-d* exchange constants αN_0 and CF masses m_{CF} for various FQH states of sample F2 in the vicinity of $\nu = 3/2$. The CF filling factor is denoted by ν_{CF} and the bare electron mass by m_0. Errors are estimated from the uncertainties in determining the extreme points in the experimental data.

ν	ν_{CF}	αN_0 (meV)	m_{CF} $(m_0\sqrt{B_\perp})$
5/3	1	184(8)	1.67(24)
8/5	2	160(7)	3.96(14)
7/5	3	194(6)	7.05(135)
4/3	2	202(4)	1.06(5)

can thus be attributed to disorder. From the slopes we may estimate a filling factor independent CF mass of $\tilde{m}_{CF} = 2.4\, m_0$ for our sample, about one order of magnitude larger than the electron mass in CdTe ($m^* = 0.1\, m_0$). Slightly lower filling factor independent CF masses have been reported for high-quality GaAs samples with mobilities exceeding $6 \cdot 10^6$ cm^2/Vs [126].
Besides this, the knowledge of the cyclotron gaps $\Delta_{\nu,cycl}$ allows us to directly determine a realistic CF mass $m_{CF} = C_\nu m_0\sqrt{B_\perp}$ for each filling factor from eq. 4.25 (see table 4.1). The C_ν parameters are plotted in fig. 4.13, revealing the expected mass increase as the filling factor approaches $\nu = 3/2$. This behavior is in accordance with previous experiments on GaAs [55].

Chapter Summary

Our results demonstrate the emergence of the FQHE in a semimagnetic CdMnTe QW structure. Although the presence of magnetic impurities in a 2DES is associated with strong *s-d* exchange interaction, it is evidently no obstacle to the formation of FQH sates. We perform activation energy measurements in tilted magnetic fields around filling factor $\nu = 3/2$ in order to assess the angular evolution of energy gaps at fractional fillings 5/3, 8/5, 7/5 and 4/3. In our DMS sample, the angular gap evolution is found to be strongly governed by *s-d* exchange which we capture within an extended CF model. Relevant parameters, i.e. CF masses, exchange constants and the CF g-factor, are in a good agreement with previous experiments on GaAs and Si if considering the material characteristics and the quality of the sample. The reason why the $\nu = 5/2$ state ($n = 1$ LL) remains absent down to the lowest temperatures of $T = 18$ mK in our specimen (see fig. 4.6) still remains an open question. It might primarily be attributed to an insufficient sample quality, although we clearly observe ρ_{xx} minima at $\nu = 7/3$ and 8/3. Those two states are always present along with $\nu = 5/2$ in GaAs. In this context the absence of $\nu = 5/2$ is even more surprising since the state is expected to be stabilized in case of wide QWs, such as the one of the studied sample.

4.3 Summary - FQHE in CdTe and CdMnTe

A central issue concerning the investigation of the FQHE is the spin polarization of the FQH ground states, usually strongly influenced by the external magnetic field [52, 110]. Since its discovery quite exactly 30 years ago the FQHE has typically been studied in GaAs-based systems where due to the small Zeeman energy E_Z several fractional ground states are spin unpolarized. Increasing E_Z then typically induces changes in their spin polarization and consequently results in angular dependent energy gaps. As we demonstrate in experiment, the situation however is different in case of the II-VI compound semiconductor CdTe: Transport experiments at mK temperatures reveal no significant changes of the energy gaps of the $\nu = 5/3$ and $4/3$ states as the Zeeman energy is increased by tilting the sample. Such behavior is indeed expected for spin-polarized ground states where the lowest energy excitation does not involve a spin-flip and is a direct consequence of the about 4 times larger g-factor of CdTe compared to GaAs.
Despite its emergence in several non-magnetic materials (including GaAs, CdTe, graphene and others), the FQHE has never been observed in any diluted magnetic semiconductor. This raised the question whether the formation of FQH states might be inhibited by the presence of magnetic impurities. Our experiments however rule out such scenario, as they clearly reveal the emergence of FQH states in a semimagnetic CdMnTe QW device at filling factors $\nu = 5/3$, $8/5$, $7/5$ and $4/3$. We prove that s-d exchange interaction - brought about by the incorporated manganese ions - strongly influences the evolution of activation energy gaps when E_Z is changed by tilting the sample. $Cd_{1-x}Mn_xTe$ presents a perfect system for the investigation of spin-related effects in the FQHE regime since s-d exchange offers the possibility to tune the Zeeman splitting to zero at nearly any desired magnetic field value (via changing the in-plane field or the manganese content of the sample). The tunability of E_Z might for instance help to answer the outstanding question whether the $\nu = 5/2$ state (possibly emerging in $Cd_{1-x}Mn_xTe$ with increasing sample quality) could form skyrmions[4] or spin topological defects at $E_Z = 0$ meV. Even though the $5/2$ state has been proven to be fully spin-polarized [40,41], some optical experiments suggest its depolarization by skyrmion formation or spin topological defects at vanishing E_Z [39, 40, 127].

[4] A skyrmion is a coherent charge and spin excitation that is spread over two energy levels. It comprises a spin texture that rotates several spins simultaneously and carries an electric charge of $\pm e/m$ at filling factor $\nu = 1/m$.

5 Spin Transistor Action via Tunable Adiabaticity

Besides high mobilities - necessary for the observation of the fractional Quantum Hall effect - the CdMnTe systems with its giant spin splitting of up to several meV offers the possibility to explore magnetotransport in yet another novel regime: Electrons under the influence of an artificial spin superstructure (helical spin polarization). In analogy to experiments on magnetically driven commensurability effects, an array of pre-magnetized ferromagnetic stripes (dysprosium or iron) on the sample surface is utilized to induce a spatially varying magnetic field in the underlying 2DES. As a consequence of the huge CdMnTe Zeeman splitting even the small stray field amplitude of such stripe grating is sufficient to give rise to a significant (spatially oscillating) spin polarization of the electrons, thus constituting a spin superstructure.
As will be discussed in detail below, the formation of such a helical spin polarization allows to control spin transmission through the sample (i.e. its resistance) by an external magnetic field. The studied devices therefore represent an alternative way to realize spin transistor action, distinct from the approach by Datta and Das [128].

5.1 Initial Considerations

The schematic sample design employed in the following investigations is displayed in fig. 5.1: A grating of pre-magnetized ferromagnetic stripes on the sample surface, patterned to periods a ranging from 0.5 μm to 8 μm. Their fabrication has already been discussed in chapter 3.1.3. The 75 nm thick stripes are made of either dysprosium or iron and provide an approximately helical stray field B_s in the plane of the electrons (see fig. 5.2). Its inplane ($B_{s,x}$) and out-of-plane ($B_{s,z}$) components are phase shifted by $\pi/2$ and in a first approximation they are of sinusoidal shape with a field strength of about 50 mT in the case of Dy stripes (details are to be discussed later). In order to translate this helical magnetic field texture into the desired spin superstructure, a semiconductor with huge Zeeman splitting is required. We therefore have chosen CdMnTe-based QWs, exhibiting an exchange-enhanced spin splitting of several meV at low temperatures and low

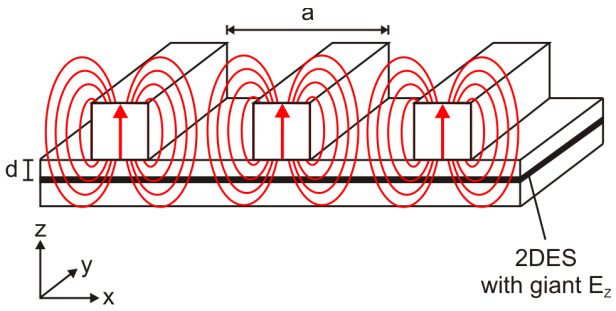

Figure 5.1: Schematic layout of the specimens under investigation. A grating of pre-magnetized ferromagnetic stripes of period a on the sample surface gives rise to a stray field in the underlying 2DES at depth d. The magnetization direction of the stripes is indicated by red arrows. If a semiconductor with giant Zeeman splitting E_Z is chosen (e.g. CdMnTe), the stray field directly induces a spatially oscillating spin polarization. Note the close analogy to experiments on commensurability effects.

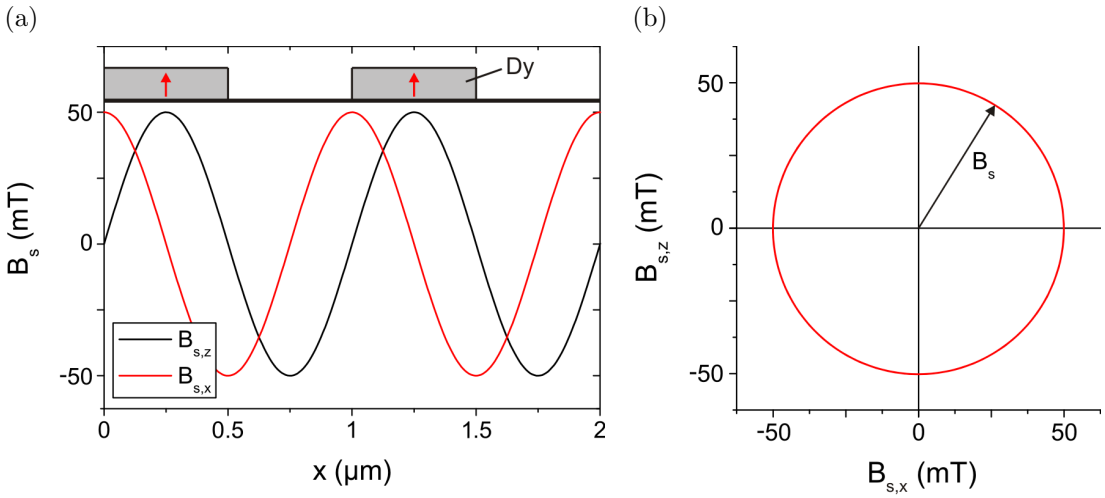

Figure 5.2: (a) Idealized magnetic stray field components $B_{s,x}$ and $B_{s,z}$ of a Dy stripe grating of 1 micron period in the plane of the 2D electron gas at a distance of 100 nm below the surface. The position of the stripes and their magnetization is indicated. (b) The helical shape of the stray field becomes apparent when plotted in the $B_{s,x}$-$B_{s,z}$ plane.

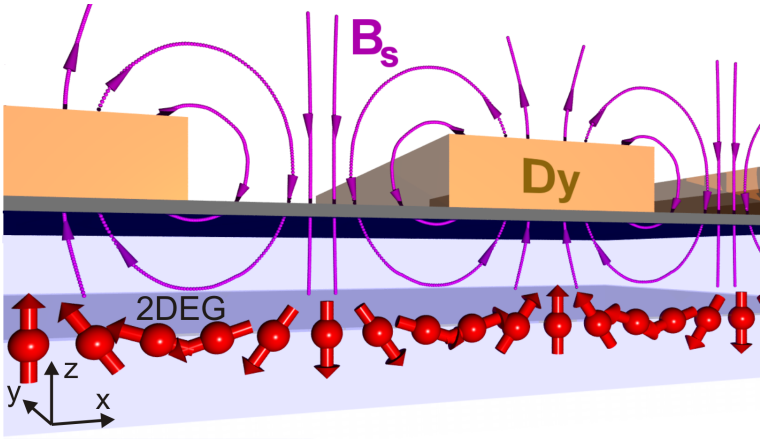

Figure 5.3: Schematic view of the experimental situation in the absence of an external magnetic field. Due to the giant Zeeman splitting of CdMnTe electron spins in the 2DES (spheres with arrows) are aligned by the stray field B_s of the stripes and a spin helix forms.

magnetic fields (see fig. 2.9). The stray field induced spin polarization p is given by

$$p = \frac{n_\uparrow - n_\downarrow}{n_\uparrow + n_\downarrow} = \frac{E_Z}{2E_F - E_Z} \approx \frac{E_Z}{2E_F}, \tag{5.1}$$

where

$$n_\uparrow = E_F \frac{D(E)}{2} \quad \text{and} \quad n_\downarrow = (E_F - E_Z) \frac{D(E)}{2} \tag{5.2}$$

is the number of spin-up and -down electrons in the CdMnTe conduction band, respectively. E_F denotes the Fermi energy, E_Z the spin splitting and $D(E)$ the density of states. The relation $2E_F \gg E_Z$ allows to simplify the above equation. For the samples under investigation (see appendix and tab. 5.1) the Zeeman splitting is estimated from the beating pattern of the SdH oscillations at low fields (see sec. 4.2.1) to 1 meV in the case of 50 mT stray field and a temperature of 25 mK. Hence, E_Z is the largest spin-dependent energy scale in our structures, as Rashba and Dresselhaus spin-orbit splittings are more than one order of magnitude smaller (about 100 μeV). The Fermi energy on the other hand is simply given by the carrier density and is about 10 meV in our case. Consequently, in the presence of giant Zeeman coupling and the absence of an external field the grating's (helical) stray field induces a helical pattern of spin polarization (spin helix) in the 2DES (see fig. 5.3). Its magnitude ranges between 8% and 15%, dependent on the exact carrier density (here $n_s = 2.77 \cdot 10^{15}$ m^{-2} to $4.99 \cdot 10^{15}$ m^{-2}). Since an increasing temperature drastically lowers the Zeeman splitting in CdMnTe (see fig. 2.9b) the spin polarization is expected to vanish rapidly upon heating the sample to temperatures above 1 K.

In experiments dysprosium is typically chosen as stripe material for two reasons: First, due to its high (bulk) saturation magnetization $M_s = 2.92 \cdot 10^6$ A/m (compare to $M_s = 1.74 \cdot 10^6$ A/m of iron) and the hence enhanced stray field. Second,

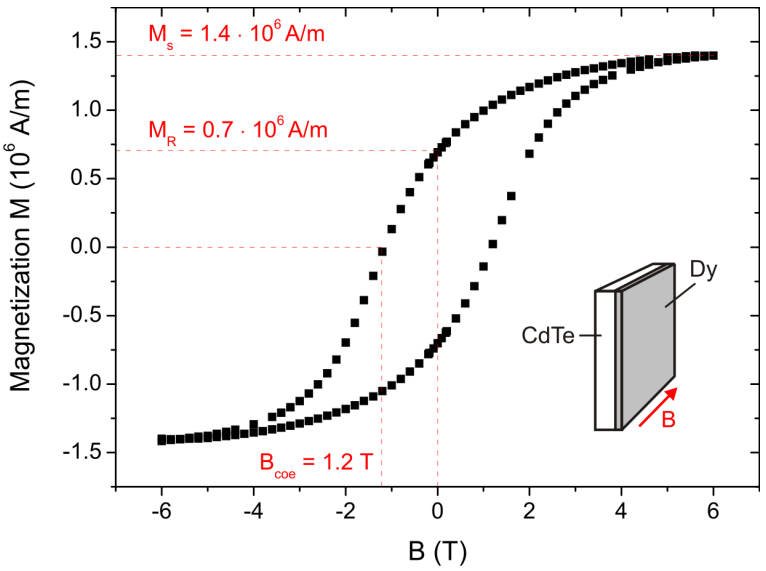

Figure 5.4: SQUID magnetometry of a 75 nm thick film of dysprosium at $T = 4$ K; the magnetic field B is applied inplane. The film features a remanent magnetization of $M_R = 0.7 \cdot 10^6$ A/m and a coercive field $B_{coe} = 1.2$ T. Magnetization saturation at $M_s = 1.4 \cdot 10^6$ A/m occurs at fields higher than 6 T. The inset sketches the experimental situation.

because of its large coercive field of about $0.5-1$ T [129] which allows to choose the stripes' remanent magnetization direction via pre-magnetization in a sufficiently large external magnetic field. The low Curie temperature of $T_c = 88.3$ K of dysprosium is no limitation for this work, since all experiments are performed at cryogenic temperatures. Results obtained on iron gratings will be reviewed in section 5.4.

The magnetization of the Dy stripes is estimated from SQUID[1] magnetometry studies performed in the group of Christian Back in Regensburg. For this purpose 75 nm thick films of dysprosium are deposited on CdTe substrates. Their magnetization is recorded at 4 K temperature as a function of an external magnetic field which is applied in the plane of the film. As revealed by the hysteresis trace shown in fig. 5.4, the magnetization saturates at $M_s = 1.4 \cdot 10^6$ A/m for fields exceeding 6 T. Thus, in magnetotransport experiments the stripe gratings will be pre-magnetized at a field of 8 T. The SQUID results further yield a remanent magnetization of the films of $M_R = 0.7 \cdot 10^6$ A/m and a coercive field B_{coe} of about 1 T. We consider both to be equal to the remanent magnetization and the coercive field of the Dy stripe arrays, respectively. Future experiments will address the question why the saturation magnetization of the Dy films deviates from the bulk value by about a factor of two.

Micromagnetic simulations are subsequently employed to calculate the stray field of the pre-magnetized stripes. For this purpose the latter are spatially discretized

[1]SQUID: Superconducting Quantum Interference Device.

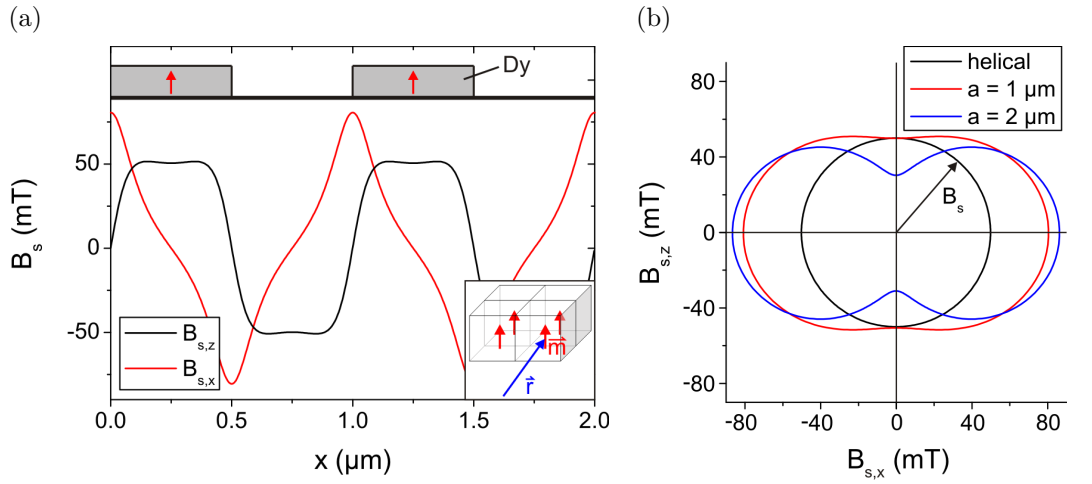

Figure 5.5: (a) Computed stray field texture of 75 nm thick Dy stripes of period $a = 1$ μm as present in a 2DES 100 nm below the surface; the stripes are magnetized perpendicular to the sample plane. Inset: For numerical calculations the stripes are discretized into small cubes, each carrying a magnetic dipole moment $\vec{m}$. A dipole at position $\vec{r}$ contributes to the total stray field according to the dipole formula 5.3. (b) Computed stray field profiles plotted in the $B_{s,x}$-$B_{s,z}$ plane. Upon larger modulation period they increasingly deviate from helical shape.

into small cubes of volume V, each carrying a magnetic dipole moment $m = M_R V$, where M_R is the remanent magnetization of the stripe array. In the plane of the 2DES the total stray field is given by the stray field contribution of every single cube. These individual contributions are computed within the framework of the magnetic dipole approximation, assuming stripes that extend to infinity in y direction and display a perfectly homogeneous magnetization perpendicular to the 2DES (see fig. 5.1). This idealized picture is sufficient to correctly explain the experiments. According to simple electrodynamics the stray field far from a magnetic dipole is in first order given by [130]

$$B_\alpha = \frac{\mu_0}{4\pi}\frac{1}{r^5}\left[3x_\alpha \sum_{\beta=1}^{3} m_\beta x_\beta - r^2 m_\alpha\right]. \tag{5.3}$$

Here, x_α denotes one space coordinate of the dipole ($\alpha = 1, 2, 3$), m_α the component of the dipole moment in x_α direction and $r = \sqrt{x_1^2 + x_2^2 + x_3^2}$ the distance to the dipole (see inset of fig. 5.5a). The stray field of an isolated dipole hence decreases as r^{-3}, while in case of an infinite line-element (i.e. an idealized stripe) it can be shown to decay as r^{-2}. In the studied devices the distance r is mainly given by the cap thickness of the QW structure. Some realistic stray field textures are depicted in fig 5.5 for the case of a 2DES 100 nm below the surface. The field amplitude in the electron gas sheet is of about 50 mT, its shape deviates more and more from a helix as the modulation period a is increased.
The helical spin polarization is expected to affect magnetotransport in the limit of

low external fields where the grating stays magnetized - i.e. the external field does not exceed the stripes' coercive field. At higher fields however the modulating stray field only is a perturbation to the larger homogeneous external field. In this regime magnetic commensurability oscillations (COs) are expected, if the electron mean free path satisfies the relation $l_{mfp} > a$. The samples under investigation exhibit mean free paths of 0.47 to 1.39 μm, consequently (weakly developed) COs can be observed in case of the shortest modulation periods only (see sec. 5.2).

Chapter Summary

CdMnTe QW structures subjected to a magnetic modulation potential are expected to reveal new low-field magnetoresistance effects. As a consequence of the giant Zeeman coupling present in this material system, the helical stray field of a ferromagnetic stripe pattern on the sample surface transforms into a helical pattern of spin polarization (spin helix). The latter is sufficiently large only at mK temperatures and decreases rapidly when heating the system. Magnetoresistance anomalies caused by such spin superstructure should therefore display a temperature dependence which follows the T-dependence of the giant spin splitting of CdMnTe. In a nutshell, the observability of spin superstructure effects is crucially linked to the magnitude of the induced spin polarization. It may either be enhanced by a lower carrier density or a higher electron g-factor (via lower temperature, higher manganese concentration or larger stray field).

5.2 Evidence of Spin Transistor Action

In recent years much of the research in the field of spin electronics has been motivated by attempts to realize the seminal Datta-Das spin transistor [128], as sketched in fig. 5.6. It is based on the idea of spin injection from a ferromagnetic contact into a narrow channel of a 2D electron gas. In case of the semiconductor featuring a strong spin-orbit coupling the typically present structure inversion asymmetry[2] gives rise to an intrinsic electric field E_z in z direction. In the moving electron's frame of reference E_z transforms into a magnetic field $B_{R,y}$ in y direction, the so called *Rashba field*. Since the source contact is magnetized along the x axis, charge carriers are injected with a spin polarization along the very same direction. They consequently start to precess under the influence of the Rashba field. When transport is ballistic the channel resistance depends on the relative orientation of the spin at the drain contact with respect to its magnetization; it is lowest in the parallel case. The gate voltage V_G allows to tune the magnitude of E_z which - via the Rashba field $B_{R,y}$ - alters the spin-precession rate. Consequently, the channel

[2] Caused by an intrinsic asymmetry of the heterostructure, e.g. due to single-sided doping of a QW or applying a gate voltage.

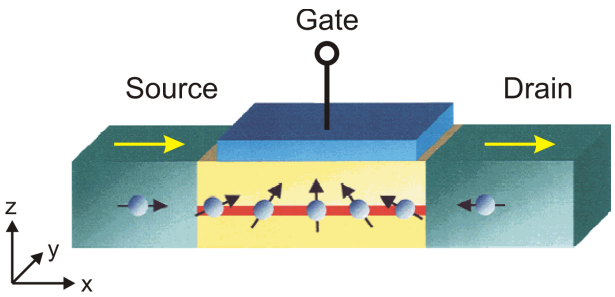

Figure 5.6: Datta-Das spin transistor. Spins are injected from the ferromagnetic source into a two-dimensional conducting channel; the magnetization of source and drain is indicated by yellow arrows. Under the influence of a gate-controlled spin-orbit field pointing in y direction spins precess into 'on' or 'off' orientations. The channel conductance is low, whenever a spin at the drain contact is antiparallel to its magnetization direction. Adopted from ref. [131].

conductance of the Datta-Das transistor is expected to oscillate periodically as a function of increasing gate voltage. Even though such spin manipulation in a spin-orbit field has been demonstrated in a non-local measurement [132], signal levels remain small due to issues in spin injection efficiency and limited spin lifetime.
Both, this and the next chapter pursue the following objective: They on the one hand provide experimental evidence that the presence of a helical spin polarization does indeed affect low-field magnetotransport, i.e. by the emergence of two distinct resistance peaks at specific field values $B_{C,\pm}$. On the other hand they introduce a theoretical model which links the observed resistance peaks to a magnetic field induced transition from the regime of adiabatic to diabatic spin transport. As will be discussed below, our studies therefore present an alternative approach to achieve spin transistor action, namely by tuning the device resistance via the regulation of adiabaticity of spin transport. Our concept strongly differs from the one proposed by Datta and Das in 1990.

5.2.1 Setup and First Experiments

We demonstrate the validity of our spin transistor concept in a CdMnTe QW structure where spins are transported in a spatially periodic magnetic field due to pre-magnetized ferromagnetic stripes on top of the device. As will be shown, adiabaticity of spin transport is controlled with an external homogeneous magnetic field. Similar to the original Datta-Das concept we measure the source-drain resistance which in our case is modulated by changes in the spin transmission. However, no ferromagnets are used to inject spin, instead spin polarization in the 2DES is induced by the giant Zeeman splitting of the chosen semiconductor material. The emerging helical spin polarization is maintained by keeping spin transport in the adiabatic regime. In the moving electron's frame of reference this means that the magnetic stray field rotates slowly on the time scale defined by

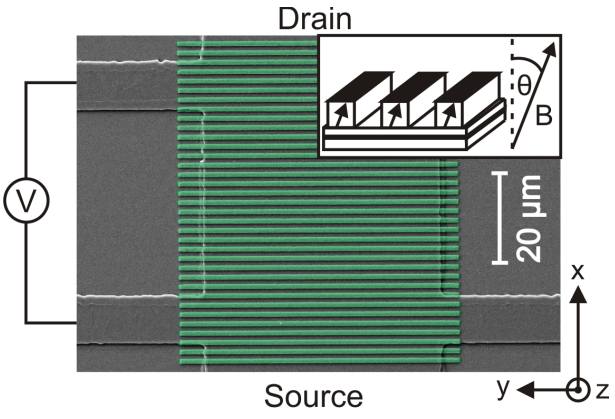

Figure 5.7: Electron micrograph of a spin transistor prototype: A Hallbar segment, covered with dysprosium stripes (green) of period $a = 2$ μm. Current is fed from source to drain, the potential probes measure the longitudinal voltage drop $V = \rho_{xx} I$. Inset: Orientations of external magnetic field B and magnetic moments of the pre-magnetized stripes as defined by the tilt angle θ. At sufficiently large values of B the magnetic moments are always aligned along the field direction.

Larmor precession (with Larmor frequency $\omega_L = g_{\mathit{eff}} \mu_B B_s / \hbar$) and electron spin therefore aligns with the local field. In our samples $g_{\mathit{eff}} \approx 350$ at $T = 25$ mK and for a stray field amplitude of 50 mT. Details on adiabatic spin transport are to be discussed in section 5.3.

The experimental setup is displayed in fig. 5.7: A simple Hallbar geometry is used to explore the magnetotransport coefficients. All measurements are performed on samples covered with dysprosium stripes and follow the same scheme: At first the stripes are pre-magnetized in a field of 8 T, either perpendicular to the electron gas sheet or tilted in the x-z plane to an angle θ away from the sample plane normal (see inset of fig. 5.7 and fig. 2.2a). Afterwards the magnetic field B is swept from +8 T to −3 T and data is recorded while keeping the tilt angle θ unchanged. All experiments are conducted at angle $\theta = 0°$, except when noted. Relevant sample parameters are summarized in table 5.1 below.

In the presence of a helical stray field the longitudinal resistance ρ_{xx} in the low-field limit features distinct peaks at about $B_{C,\pm} \approx \pm 50$ mT. This is depicted in fig. 5.8 (blue trace) for one of the studied devices, sample A with $a = 2$ μm and the 2DES located 85 nm below the surface. In contrast, the peaks do not appear in the magnetically unmodulated reference structure where the helical spin polarization is absent (black trace). The beating pattern emerging at fields $|B| > B_{C,\pm}$ allows to estimate the manganese concentration in the QW of sample A to $x = 0.55\%$ (for details refer to sec. 4.2.1).

Sample A further reveals (fig. 5.9) that a reduction of the modulation period from 2 μm to 0.5 μm results in a rather unchanged low-field texture of the longitudinal resistance ρ_{xx} (black trace, $T = 25$ mK). The observation of spin helix induced resistance peaks in modulated CdMnTe samples hence is not limited to a specific stripe period. However, the resistance peaks at $B_{C,\pm} \approx \pm 50$ mT are found to be less distinct in the case of $a = 0.5$ μm, namely due to superposition of another effect: the positive magnetoresistance associated with magnetic commensurability oscillations (COs). Their regime is entered as a stripe period of 0.5 μm already is shorter than sample A mean free path ($l_{\mathit{mfp}} = 1.39$ μm). In fact, weakly developed

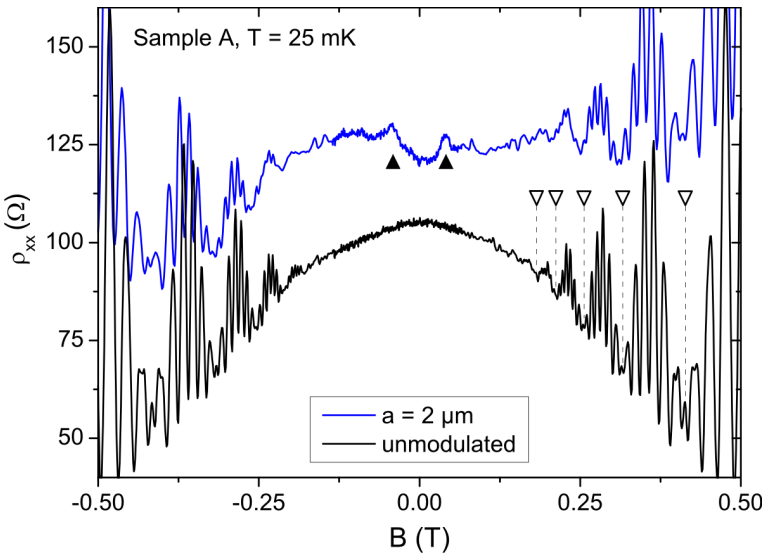

Figure 5.8: Low-field longitudinal magnetoresistance of sample A in the absence (black trace) and presence of a helical stray field (blue trace, shifted for clarity). Sample tilt angle $\theta = 0°$ and temperature $T = 25$ mK. Distinct resistance peaks only emerge in the case of magnetic modulation at fields $B_{C,\pm} \approx \pm 50$ mT (filled triangles). A distinct beating pattern with nodes (open triangles) emerges at higher magnetic fields $|B| > B_{C,\pm}$ due to the presence of manganese in the quantum well.

COs are observed, quite well coinciding with the magnetic flatband condition (eq. 2.36)

$$2R_c = \left(\lambda + \frac{1}{4}\right) a, \quad \text{with} \quad \lambda = 1, 2, 3, \ldots \quad . \tag{5.4}$$

In addition, the manganese beating pattern quenches the amplitude of the SdH oscillations at several other field values, thus leading to a rather complex pattern of local ρ_{xx} minima in the case of $T = 25$ mK. However, above effects can be separated by their temperature dependence: The beating pattern is found to wash out upon increasing T [59], as well as the spin helix induced resistance peaks which are strongly attenuated at temperatures higher than 300 mK (see fig. 5.13 and discussion later in this text). Due to their orbital nature, commensurability effects sustain temperatures of up to 40 K [65] on the contrary. They therefore dominate low-field magnetotransport at already 1 K (see fig. 5.9, red trace), the highest temperature achievable in the dilution refrigerator employed in these studies. Since the positive magnetoresistance around $B = 0$ T exhibits nearly no temperature dependence we can conclude that it mainly originates from commensurability effects. In the low T limit it is superimposed by spin helix induced resistance peaks which - rather than causing distinct features - only slightly modify the shape of the magnetoresistance. Despite the fact that commensurability effects mask the spin helix induced resistance peaks in the limit $l_{mfp} > a$ we benefit from their occurrence for the following reasons:

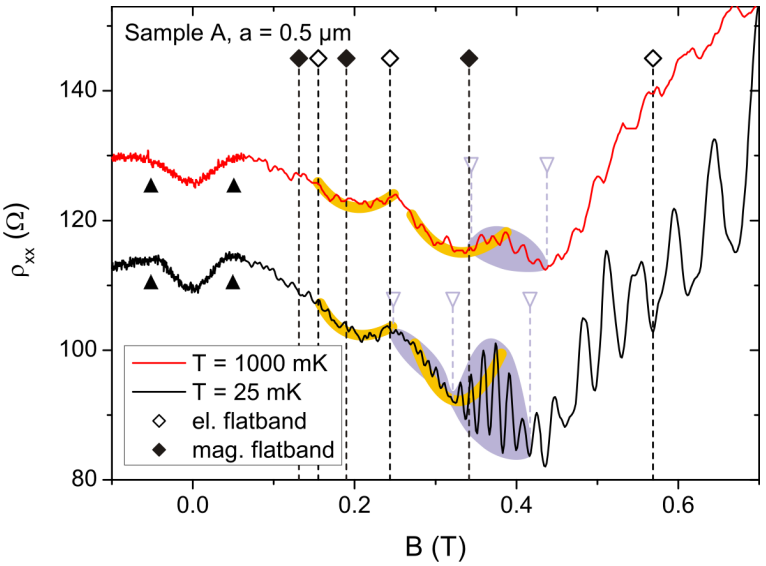

Figure 5.9: Temperature dependence of longitudinal resistance ρ_{xx} of sample A with 0.5 μm modulation period at $\theta = 0°$ (red trace shifted for clarity). Due to the long electron mean free path of 1.39 μm weak commensurability oscillations are observed: Filled/open diamonds indicate the magnetic/electric flatband condition, thick solid lines are guides to the eye. The SdH beating pattern (blue shaded) is superimposed on the COs and quenches the amplitude of the ρ_{xx} oscillations at specific positions (open triangles). The positive magnetoresistance around zero field shows merely no temperature dependence and thus is related to commensurability effects. Its saturation value of about 55 mT (filled triangles) allows to estimate the strength of the stray field z component. At $T = 25$ mK the magnetoresistance is superimposed by the spin helix induced resistance peaks which only cause a slight shape modification.

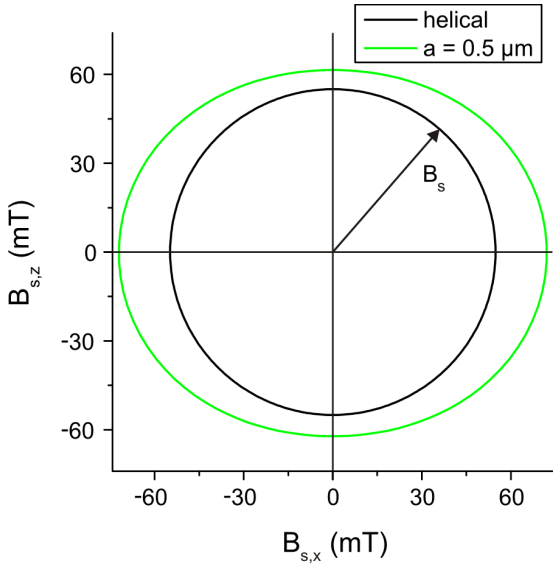

Figure 5.10: Calculated stray field texture of 0.5 μm period dysprosium stripes in the plane of sample A 2DES, 85 nm below the surface. The black trace represents the helical approximation of the stray field with 55 mT amplitude, as estimated from the saturation of the positive magnetoresistance at 1 K (see fig. 5.9).

- Since at high temperatures merely commensurability effects prevail, we can estimate the stray field strength from the saturation of the positive magnetoresistance around $B = 0$ T. The 1 K data reveal a saturation value of $\tilde{B} = 55$ mT which according to the theory of COs equals the out-of-plane stray field component $B_{s,z}$. This value deviates by only 8% from the one obtained by micromagnetic simulations for the case of sample A and 0.5 μm period dysprosium stripes (see fig. 5.10).
- The *assumption* that the positive magnetoresistance in fig. 5.9 purely is caused by electrostatic effects gives an upper bound of the electric modulation amplitude V_0, as discussed in chapter 2.4.2:

$$V_0 = \frac{\tilde{B}eav_F}{2\pi} = 0.82 \text{ meV}, \tag{5.5}$$

  where $v_F = \hbar\sqrt{2\pi n_s}/m^*$ is the Fermi velocity. V_0 certainly is by far overestimated, but even this value satisfies the condition of weak electrostatic modulation, $V_0 \ll E_F$, with $E_F = 10$ meV for sample A.
- The good coincidence of magnetic flatband condition and low-field ρ_{xx} minima is an additional hint that electrostatic effects play a minor role in the samples. The minima would otherwise be shifted closer towards the electric flatband positions. Electrostatic effects could either be strain induced (different thermal expansion coefficients) or result from the illumination of the sample (see below) since the stripe grating acts as a shadow mask. The persistent photoeffect in CdTe [133] could in principle turn these spatially periodic illuminated regions into an electrostatic modulation potential.

In order to avoid a mixing of effects stemming from the helical spin polarization with the commensurability related positive magnetoresistance we will from now on study samples which satisfy the condition $a \geq l_{mfp}$.
Prior to transport experiments the specimens are typically illuminated using a yellow LED as this drastically enhances sample quality - mainly via an increase of quantum lifetime τ_q (see discussion in sec. 4.1). However, illumination is not a prerequisite for the observation of the resistance peaks as shown in fig. 5.11 which compares the longitudinal resistance of sample D (furnished with 0.5 μm period dysprosium stripes) before and after illumination. The spin helix induced resistance peaks are strongest pronounced in pre-illumination data (peak height about a factor 2.5 larger) which can be attributed to a higher carrier density and thus lower spin polarization after illumination.

5.2.2 Towards a Spin Transistor

As was already implied by above discussions, the emergence of the resistance peaks at $B_{C,\pm}$ is independent of the detailed wafer structure as well as of the

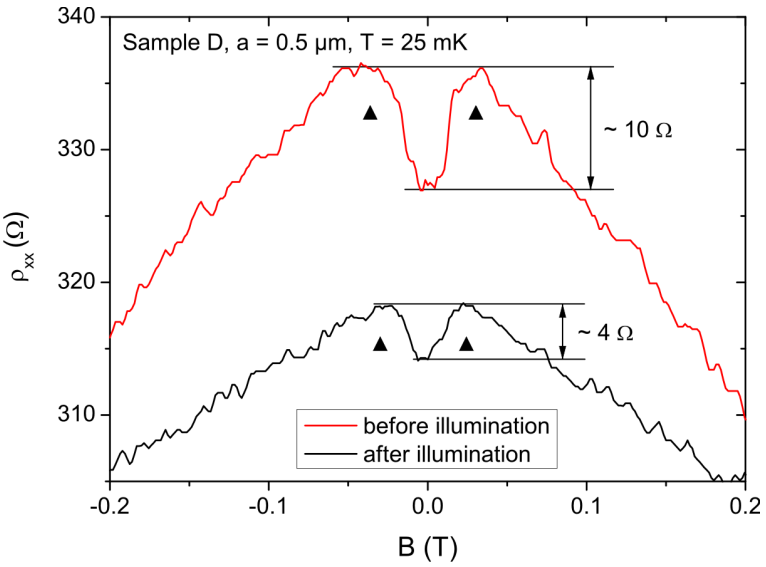

Figure 5.11: Longitudinal resistance ρ_{xx} of sample D before and after illumination. The modulation period a is 0.5 μm, $T = 25$ mK and $\theta = 0°$. Prior to illumination the spin helix induced resistance peaks (filled triangles) are strongest pronounced (roughly 10 Ω peak height). Traces are not shifted with respect to each other, but illumination leads to higher mobilities and hence reduced overall resistances.

modulation period - at least within the investigated ranges. The studied devices (listed in tab. 5.1) differ essentially in QW thickness, carrier density n_s, electron mobility μ and Mn concentration x, but qualitatively show the same features. This is summarized in fig. 5.12 depicting the low-field magnetoresistance ρ_{xx} of samples B and C for selected modulation periods. Apart from a small dip near $B = 0$ T, which is reminiscent of weak anti-localization (black traces), the reference samples do again not show any notable features at low magnetic fields. The resistance peaks are found to be most pronounced in sample C (as a consequence of its low carrier density - see discussion in the next chapter) and for a stripe period of $a = 1$ μm. We will therefore exemplify the properties of spin

Table 5.1: Details on the studied heterostructures. Here, d denotes the distance between 2DEG and sample surface and x the manganese concentration. The values of carrier density n_s, electron mobility μ and electron mean free path l_{mfp} are obtained after illuminating the sample. Manganese is incorporated into sample A, B and D QWs by the digital alloy technique [79] while sample C QW features a homogeneous manganese distribution.

sample	wafer no.	QW (nm)	spacer (nm)	d (nm)	x (%)	n_s (10^{11} cm^{-2})	μ (10^5 cm^2/Vs)	l_{mfp} (μm)
A	013108A	20	20	85	0.55	4.18	1.30	1.39
B	030607A	10	15	75	1.1	4.99	0.40	0.47
C	020508A	30	30	100	1.0	2.77	0.75	0.65
D	092106A	10	15	98	0.70	4.55	0.43	0.47

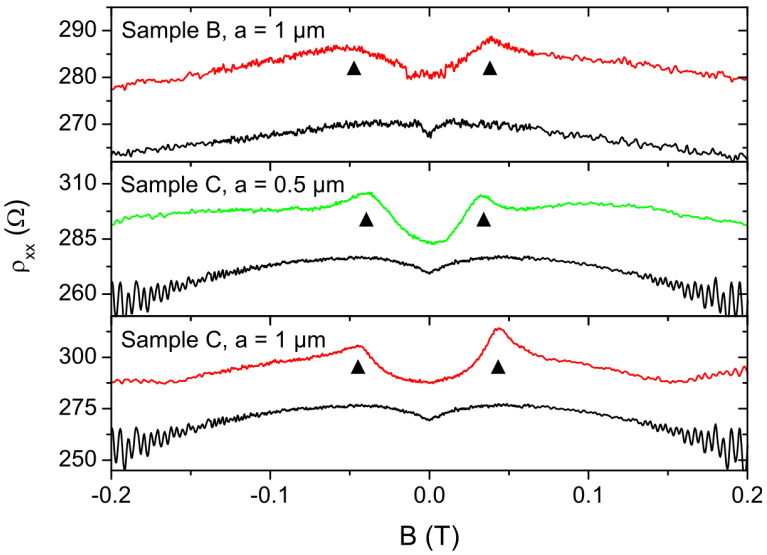

Figure 5.12: Longitudinal resistances of samples B and C in the absence (black traces) and presence (colored traces, shifted for clarity) of a helical spin polarization. Sample tilt angle $\theta = 0°$ and temperature $T = 25$ mK. Filled triangles indicate the resistance peaks at $B_{C,\pm}$.

helix induced resistance peaks mainly by considering sample C.
In order to substantiate the claim that the observed low-field resistance peaks are related to the formation of a helical spin polarization, we carried out additional experiments which are summarized in figs. 5.13 and 5.14 for sample C. The other samples showed very similar behavior. The resistance peaks in the magnetically modulated samples vanish rapidly with increasing temperature (fig. 5.13) and they are no longer recognizable above 1 K. This is in line with the expected temperature dependence of the spin polarization of CdMnTe since the dominant s-d exchange part in the g-factor contributes significantly only at low temperatures (see eq. 2.35 and fig. 2.9b). Again, magnetic commensurability effects can on the one hand be excluded because of the large modulation period and on the other hand since they sustain much higher temperatures [65] due to their orbital nature. The temperature dependence of the peaks hence confirms a spin-related effect. In addition, measurements in tilted magnetic fields allow to prove the relation between stray field and spin helix. Since the actual stray field profile of the magnetized stripes is anisotropic and deviates from helical shape in the plane of the 2DES (see figs. 5.5 and 5.10) the resistance peak positions should depend on the angle of stripe magnetization. In fact, tilting the sample alters the strength of both stray field components $B_{s,x}$ and $B_{s,z}$, resulting in a modified field texture. This anisotropy is indeed observed in experiments (fig. 5.14) where we measure the magnetoresistance at magnetic fields which are tilted to an angle θ with respect to the 2DEG plane in the direction of the x axis. With increasing tilt

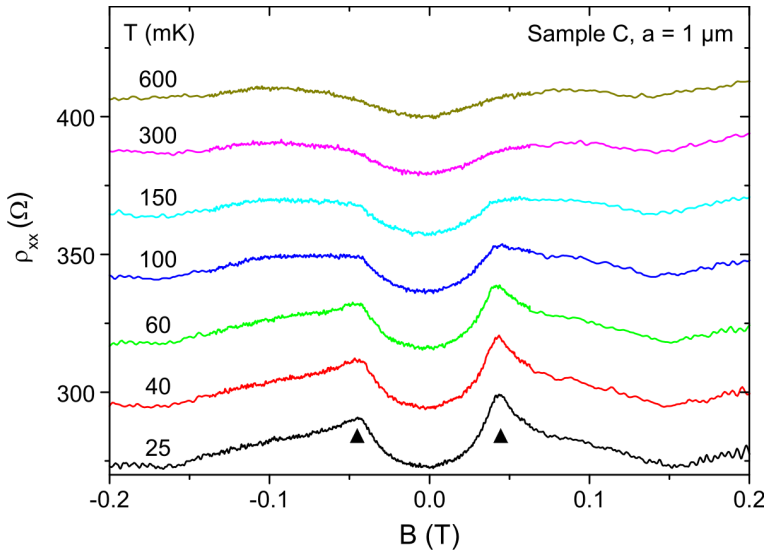

Figure 5.13: Longitudinal magnetoresistance traces collected on sample C at different temperatures T. The spin helix induced resistance peaks (filled triangles) only emerge at the lowest temperatures and hence indicate a spin related effect. Period length $a = 1$ μm and $\theta = 0°$. The curves are shifted for clarity, except the black one. Sample inhomogeneities are likely to cause the asymmetry between left and right peaks.

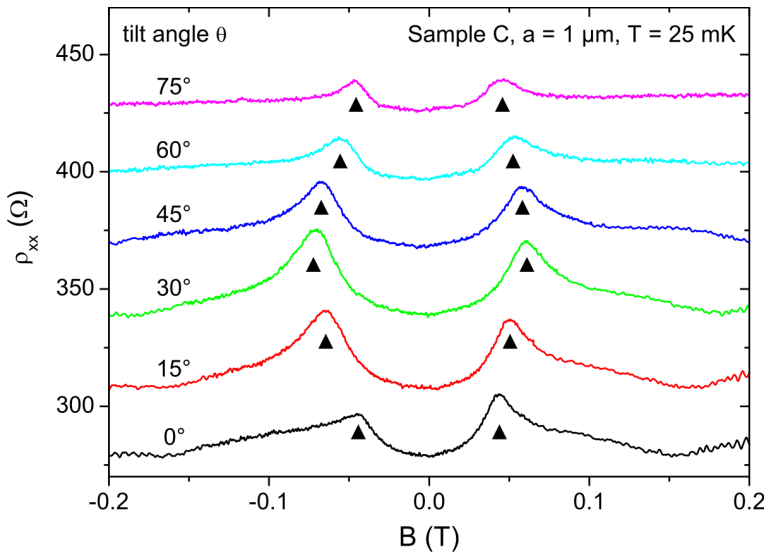

Figure 5.14: Longitudinal resistance of sample C for various tilt angles θ at $T = 25$ mK and period $a = 1$ μm. The angular shift of the peaks (filled triangles) reflects the anisotropy of the realistic stray field texture of the ferromagnetic stripes. Curves are shifted for clarity, except the black one.

angle the position of the spin helix induced peaks shifts non-monotonously first towards larger $B_{C,\pm}$ values and finally back for still higher θ. This gives additional evidence that the low-field resistance peaks are related to the formation of a (in first approximation) helical spin polarization.

Chapter Summary

A CdMnTe-based 2DES features pronounced peaks in the low-field longitudinal magnetoresistance at distinct values $B_{C,\pm} \approx \pm 50$ mT, when subjected to an unidirectional magnetic modulation. The expected formation of a helical pattern of spin polarization (spin helix) is indeed confirmed by experiment: On the one hand the temperature dependence of the resistance peaks - namely a strong attenuation above 300 mK - is in agreement with the T-scaling of the spin polarization which is governed by the exchange-enhanced CdMnTe Zeeman splitting. On the other hand the peak positions shift upon tilting the stripes' magnetization away from the sample plane normal. This modifies the texture of the stray field in the electron gas sheet and hence the exact spin polarization pattern. Both observations confirm that the resistance peaks at $B_{C,\pm}$ are a spin related effect. They are found to be independent of heterostructure details as well as modulation period (at least within the range between 0.5 μm and 8 μm).
Our setup, which consists of only a high-mobility 2DES with giant Zeeman splitting and a grating of ferromagnetic stripes, hence allows to tune the device resistance via an external magnetic field. In the upcoming chapter we will prove that these resistance peaks are caused by a magnetic field induced backscattering of spin-polarized states.

5.3 Blocking of Spin Transmission

In the following we present an approach to realize an efficient spin transistor design by utilizing adiabatic spin propagation to protect spin information and tunable diabatic Landau-Zener transitions between spin eigenstates for spin transmission control (see fig. 5.15). According to the adiabatic theorem of quantum mechanics (refer to the next section for a brief introduction) a spin which initially is in an eigenstate will remain in its instantaneous eigenstate during transport if external perturbations act on it slowly. In our case this means that in the adiabatic regime a spin is continuously rotated by the helical stray field. Hence, spin information is protected against decay, allowing spin to propagate over typical device distances. For rapidly changing perturbations however, spin cannot adapt its configuration and the latter becomes a superposition of eigenstates instead. Diabatic Landau-Zener transitions between the spin eigenstates are hence caused, which can be used to selectively backscatter spin-polarized charge carriers. This gives rise to

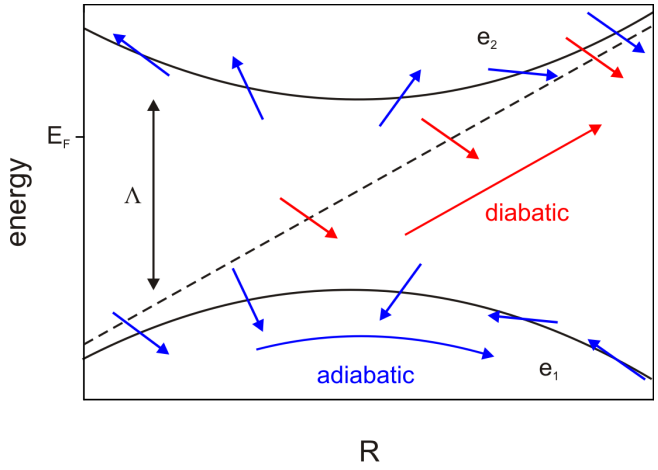

Figure 5.15: Spin transistor action via tunable diabatic transitions in a system of two orthogonal spin eigenstates e_1 and e_2 with energy separation Λ at the closest approach. A spin which is transported along the coordinate R through the system starting from e_1, will remain in this instantaneous eigenstate if evolution (here rotation of eigenstate spin orientation) is slow in the reference frame of the spin (small $\mathrm{d}R/\mathrm{d}t$). In a fast evolution (large $\mathrm{d}R/\mathrm{d}t$) spin cannot adapt to the changing environment, leading to a diabatic evolution (red arrows) corresponding to a Landau-Zener transition to e_2. The e_2 state lies above the Fermi energy E_F which causes wave function decay and spin backscattering. Spin transistor action involves either tuning Λ or $\mathrm{d}R/\mathrm{d}t$.

transistor action, based on the control of the degree of transport adiabaticity rather than on spin precession in a gate-controlled spin-orbit field.

5.3.1 The Adiabatic Theorem of Quantum Mechanics

Since adiabatic spin transport and diabatic Landau-Zener transitions are the key operation principles of the studied devices, these concepts shall briefly be introduced. The *adiabatic theorem* of Quantum Mechanics - proposed by Born and Fock in 1928 [134] - may be stated as follows [135]:

> *A physical system remains in its instantaneous eigenstate if a given perturbation is acting on it slowly enough.*

To account for its consequences, let us consider a quantum mechanical system which at time $t = t_0$ is in an eigenstate $\psi(x, t_0)$ of the Hamiltonian $H(t_0)$. A perturbation gradually changes this Hamiltonian into a new Hamiltonian $H(t_1)$ at some later time $t_1 > t_0$ and the system reaches the final state $\psi(x, t_1)$. According to the adiabatic theorem, the time scale $\tau = t_1 - t_0$ on which the perturbation acts on the system crucially affects the wave function $\psi(x, t_1)$, thus defining two types of processes:

- *Adiabatic process* ($\tau \to \infty$)
  A quantum mechanical system which is subjected to a slowly varying

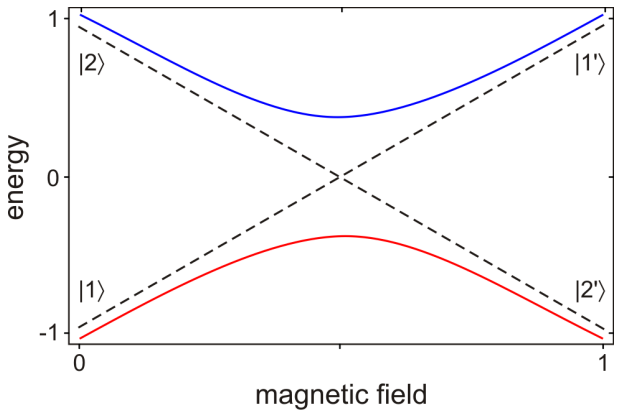

Figure 5.16: Energy levels of a two-level system subjected to an external magnetic field (in arbitrary units). The dashed lines represent the energy levels at coupling $\mathbb{V} = 0$ while the solid lines are the eigenenergies of the perturbed system at finite coupling. If initially prepared in state $|1\rangle$ the system remains in this state in an adiabatic passage, i.e. follows the red trace.

perturbation will adapt its wave function, i.e. the process modifies the probability density ($|\psi(x,t_0)|^2 \neq |\psi(x,t_1)|^2$). A system which initially is in an eigenstate of the Hamiltonian $H(t_0)$ will end up in the *corresponding* eigenstate of the final Hamiltonian $H(t_1)$. If the system for instance is in its ground state at time $t = t_0$ it will remain in the (new) ground state throughout the perturbation.

- *Diabatic process* ($\tau \to 0$)
  In the event of a rapid perturbation there is no time for the system to adapt its wave function and the latter consequently remains unchanged. Hence, the probability density is unaffected ($|\psi(x,t_0)|^2 = |\psi(x,t_1)|^2$) and the final state typically is a linear combination of eigenstates of the Hamiltonian $H(t_1)$.

A common example to illustrate diabatic vs. adiabatic processes is the avoided energy level crossing in a two-level system. Such system can for instance be a pair of Stark or Zeeman levels [136] which are linearly dependent on an external (electric or magnetic) field and cross at some specific field value (dashed lines in fig. 5.16). When they are coupled by an interaction $\mathbb{V}$, the degeneracy at the crossing point is broken and the levels repel each other. This is indicated by the solid lines in fig. 5.16 which represent the eigenenergies of the perturbed Hamiltonian. Let us now assume that the system initially is in state $|1\rangle$. The probability P that it undergoes a transition to state $|1'\rangle$ (Landau-Zener transition) when ramping up the magnetic (or electric) field is given by [136, 137]

$$P = \mathrm{e}^{-2\pi\Gamma}, \quad \text{with} \quad \Gamma = \frac{\mathbb{V}^2}{\hbar(\mathrm{d}E/\mathrm{d}t)}. \tag{5.6}$$

Here, $E = E_1 - E_2$ is the energy separation of the unperturbed levels (dashed lines) which varies linearly with B and $\mathrm{d}E/\mathrm{d}t = (\mathrm{d}E/\mathrm{d}B)(\mathrm{d}B/\mathrm{d}t)$ the slew rate. In the limits $\mathbb{V} \to 0$ or $\mathrm{d}B/\mathrm{d}t \to \infty$ the crossing is passed diabatically, i.e. $P \to 1$, and the system undergoes the transition to state $|1'\rangle$ (Landau-Zener transition). In the opposite case of finite $\mathbb{V}$ and $\mathrm{d}B/\mathrm{d}t \to 0$ the system remains in an eigenstate of the perturbed Hamiltonian throughout the process and follows the solid red

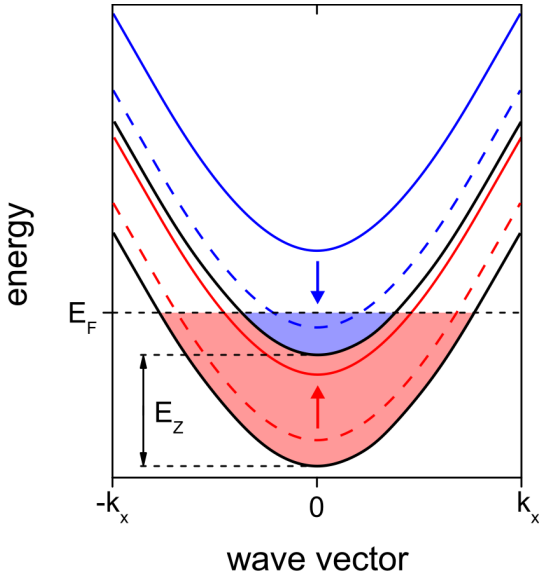

Figure 5.17: Energy dispersion relation of the CdMnTe conduction band for a spin polarization of about 30%. The dashed lines exemplify a spin-compensated pair of states whereas the red solid line shows a spin-polarized state with its counterpart unoccupied above the Fermi energy E_F (blue solid line). Black lines are the conduction band minima corresponding to each spin orientation. The shaded regions indicate a quasi-continuum of filled Landau levels at low magnetic fields. E_Z is the Zeeman splitting and k_x the wave vector in transport direction.

line (adiabatic passage, $P \to 0$). Typically, the intermediate situation of neither purely adiabatic nor diabatic behavior is the one observed in reality.

5.3.2 Ballistic Model

The spin transmission blocking in our devices can be intuitively explained within a simple ballistic model: Due to the high mobility of the samples we may for the moment assume that spin transport is ballistic on the length scale of the magnetic modulation period a, i.e. $l_{mfp} \gg a$. Figure 5.17 sketches the arrangement of the Zeeman-split parabolic energy bands of CdMnTe as a function of wave vector k_x in transport direction x in the presence of a weak magnetic field. When the field strength is of the order of 50 mT - equal to the stray field of the stripes - a quasi-continuum of filled Landau levels exists in between the Fermi energy and spin-up or -down conduction band minima. Right at the Fermi energy there is an imbalance of up and down spins propagating through the channel as some spin states exhibit unoccupied counterparts above E_F. Exactly this case is shown in fig. 5.17 for a pair of *spin-polarized* states: the upper state (solid blue line) is unoccupied while the lower one (solid red line) is occupied and carries spin. The reverse situation of a *spin-compensated* pair of states is indicated by the dashed blue and red lines. Within this simple model we assume the stray field to be purely helical

$$\vec{B_s}(x) = B_s \sin\left(\frac{2\pi}{a}x\right)\hat{x} + B_s \cos\left(\frac{2\pi}{a}x\right)\hat{z}. \tag{5.7}$$

Here, $B_s = 50$ mT denotes the stray field amplitude, a the modulation period, $\hat{x}$ and $\hat{z}$ the unit vectors in x and z direction, respectively. The total field B_{tot}

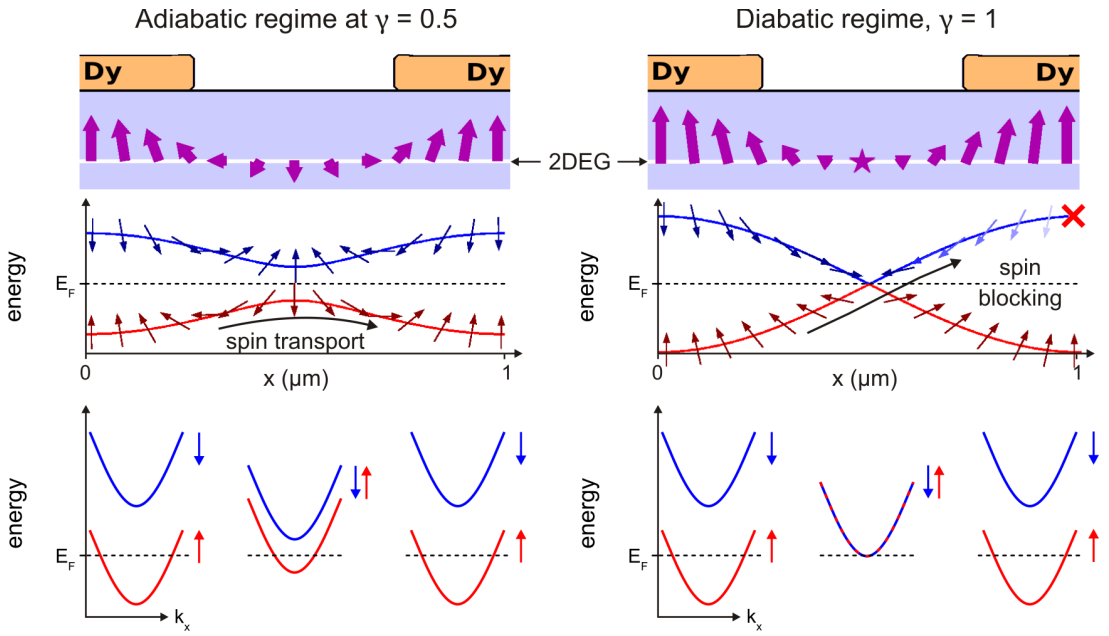

Figure 5.18: Total magnetic field acting on an electron (purple arrows, upper panels) and Zeeman-split energy bands of a spin-polarized state (middle panels) with spin orientations (arrows) in the adiabatic transport regime at $\gamma = B/B_s = 1/2$ (left) and in the diabatic regime $B = B_s$ (right) plotted for one magnetic modulation period. In the latter case the total magnetic field reverses direction at the degeneracy point in the middle (cf. stars in fig 5.19). Due to this discontinuous change in the magnetic field orientation a spin which has been transported adiabatically up to this point ends up in the higher energy band above the Fermi energy. The electron is backscattered from this Zeeman barrier and transport is consequently blocked. The lowermost panels show the corresponding local Zeeman split energy bands.

seen by the electrons consequently is composed of the external magnetic field B in z direction and the stray field and gives rise to a position dependent Zeeman splitting

$$E_Z(x) = \pm\frac{1}{2} g_{\mathit{eff}} \mu_B B_s \sqrt{1 + \gamma^2 + 2\gamma \cos\left(\frac{2\pi}{a} x\right)}. \tag{5.8}$$

The parameter $\gamma = B/B_s$ defines the ratio between external and stray field strength, g_{eff} is the (giant) effective g-factor of CdMnTe and μ_B Bohr's magneton. Let us now study in detail what happens to a spin when transported from source to drain contact. We therefore consider the spin-polarized pair of states already known from fig. 5.17 (solid red/blue lines). For this pair (i.e. for a fixed k_y) the total magnetic field, Zeeman-split energy levels, spin directions and local energy bands are depicted in fig. 5.18 for the two cases $B = B_s/2$ and $B = B_s$, respectively. Due to the large Zeeman splitting the Larmor frequency

$$\omega_L = \frac{g_{\mathit{eff}} \mu_B B_s}{\hbar} \tag{5.9}$$

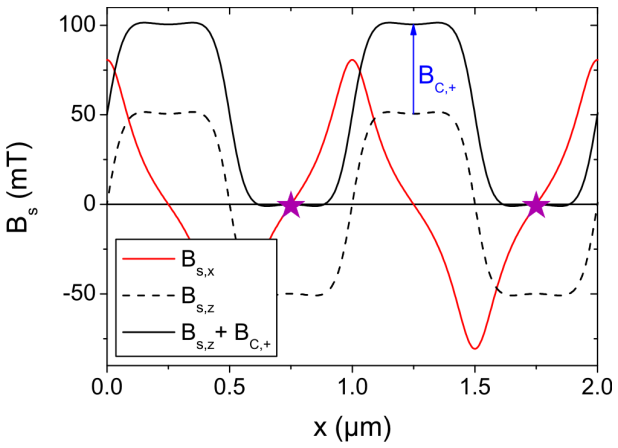

Figure 5.19: Calculated magnetic stray field components in the electron gas sheet of sample C, created by 75 nm thick Dy stripes of period $a = 1$ μm (dashed and red line; also compare to fig. 5.5a). An external homogeneous magnetic field can be tuned to $B_{C,+}$ to create a total magnetic field $B_{tot} = B_{C,+} + B_s$ which vanishes at certain positions (purple stars) and reverses its direction in the vicinity of these points. Spins cannot follow this instantaneous field reversion but are backreflected instead.

of electron spin is much higher than the frequency of stripe modulation in a ballistic flight through the device, $v_{F,x}/a$, where $v_{F,x} = \hbar k_x/m^*$ is the component of the Fermi velocity parallel to the transport direction and m^* the effective mass of CdTe. The spin splitting of typically 1 meV at 50 mT stray field and 25 mK gives rise to an effective g-factor $g_{eff} \approx 350$ and consequently to a ratio of $\omega_L\, a/v_{F,x} \approx 10$ for a stripe period of 1 μm. This keeps spin transport predominantly in the adiabatic regime as expressed by the condition

$$Q = \frac{\omega_L a}{2\pi v_{F,x}} > 1, \tag{5.10}$$

where Q measures the degree of adiabaticity in ballistic systems [138]: The larger the value of Q - the larger transport adiabaticity.
In the adiabatic regime and absence of spin-dependent scattering spins follow the total magnetic field which rotates slowly as the electron propagates through the system (see fig. 5.18, topmost left panel). Consequently, spin orientation depends only on the position along the transport direction and not on the specific path spin has taken[3]. At exactly $B = 0$ T a spin helix forms (see fig. 5.3) which even persists at external fields $B < B_s$. On the contrary, in the case $B = B_s$ a degeneracy point in the energy bands emerges midway between adjacent stripes, corresponding to a vanishing total magnetic field at exactly its position (see fig. 5.18, topmost right panel and fig. 5.19). As the external field is applied in z direction it consequently shifts the stray field z component. At exactly $B = B_{C,\pm} = \pm B_s$ the total field $B_{tot} = B + B_s$ is quenched at well defined positions giving rise to degeneracy points in the energy bands. In the reference frame of the spin the direction of the total magnetic field first rotates continuously as it approaches the degeneracy point adiabatically but then the field suddenly reverses direction (see right panels of fig. 5.18). This violates the conditions for adiabaticity since an instant 180° spin

[3]This is analogous to the mechanism which causes enhanced stability of the spin-orbit induced persistent spin helix [139, 140].

rotation would be needed to stay on the lower band. A transition to the upper Zeeman band hence occurs close to the degeneracy (Landau-Zener transition). Here the spin is now antiparallel to the magnetic field, hence giving rise to a tunneling barrier because the potential energy rises above E_F. This leads to a backreflection of carriers and spin transport is thus blocked which in turn increases the resistance of the sample. This blocking mechanism is alternatively illustrated by the lowermost panels of fig. 5.18 displaying the local energy bands of a spin-polarized pair of states: In the adiabatic regime the red band is populated with spins while the blue one lies above E_F and is empty. This situation remains unchanged on the entire path of the spin through the sample. However, in the diabatic regime at $B = B_s$ the Zeeman splitting locally vanishes and both spin bands become degenerate. Since at this particular position a 180° flip is required for the spin to stay on the (lower) red band it is instead transferred to the blue one. But this band rises above E_F which causes spins to be backreflected. Only spin-polarized modes are affected by this blocking mechanism because both spin bands of spin-compensated modes remain everywhere below the Fermi energy.
This ballistic model directly relates the height of the spin blocking peaks at $B_{C,\pm}$ to the magnitude of the spin polarization $p = E_Z/2E_F$ (eq. 5.1): An increased polarization is equivalent to a larger number of spin-polarized states in the semiconductor. Hence, more charge carriers are blocked at the degeneracy points, with $\rho_{xx} \to \infty$ as $p \to 100\%$. For a given material the resistance peaks at $B_{C,\pm} = \pm B_s$ may be enhanced by either a larger stray field (increased E_Z) or a lower carrier density (see fig. 5.11). Due to its exchange-enhanced spin splitting CdMnTe further offers the possibility to increase E_Z via lowering the temperature (see fig. 5.13) or increasing the manganese concentration x. A follow-up master thesis is going to address the carrier density dependence of the resistance peaks in detail by using gated devices. Additionally it will probe for a manganese concentration dependence in wafers with identical structure. As the samples investigated within the framework of this PhD thesis differ essentially in QW width and cap thickness we cannot unambiguously distinguish between effects stemming from a higher manganese content or a thinner cap (larger stray field).

5.3.3 Transport Calculations

This chapter will briefly review the different models used to calculate the magnetotransport properties of our spin transistor devices. Details are discussed in the supplement to ref. [141]. All our models consider spin-dependent quantum transport within the framework of the Landauer-Buttiker formalism [17, 142, 143]. When electron-electron interaction is neglected the magnetoconductance $G(B)$ of a system of width W between two leads can be expressed in terms of quantum

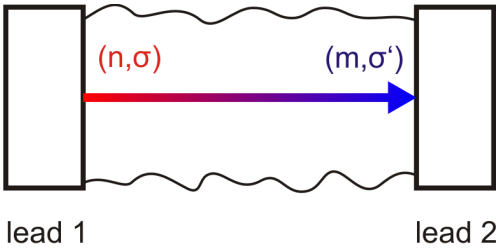

Figure 5.20: Ballistic conductor with one transverse channel, defined by channel and spin quantum number (n, σ) at the left lead and (m, σ') at the right lead, respectively. In the Landauer-Buttiker formalism each channel is assigned with a transmission probability to carry a conductance quantum e^2/h from the left to the right lead.

transmission probabilities $|t_{nm}^{\sigma\sigma'}|^2$ via

$$G(B) = \frac{e^2}{h} \sum_{n,m,\sigma,\sigma'} \left| t_{nm}^{\sigma\sigma'}(B) \right|^2 . \tag{5.11}$$

Here, the indices (n, σ) denote the transverse channel number and spin polarization ($\sigma = \pm 1$, with respect to spin quantization axis) for a state at the left lead and (m, σ') the channel and spin quantum number for a right lead state, respectively (see fig. 5.20).
The spin-dependent magnetoconductance through the magnetically modulated samples are computed on two levels of approximation outlined below: First, using a ballistic model which treats spin-flips within the Landau-Zener theory and second, using large-scale numerics based on a recursive Green's function technique for both ballistic and disordered systems.

Ballistic Spin Transport within the Landau-Zener Model

This model is a simple approach to analytically estimate the low-field magnetoresistance $\rho = 1/G$ of our spin transistor devices. We neglect disorder and consider a 2DES subject to both, a modulating stray field $\vec{B}_s(x)$ and a homogeneous perpendicular field $\vec{B} = B\hat{z}$. This is described by the Schrödinger equation

$$\left[-\frac{\hbar^2}{2m^*} \frac{\partial^2}{\partial x^2} + H_S(x) \right] \Psi = E\Psi, \tag{5.12}$$

where

$$H_S(x) = \frac{1}{2} g_{\mathit{eff}} \mu_B \left(\vec{B} + \vec{B}_s(x) \right) \cdot \vec{\sigma}. \tag{5.13}$$

In the above equation m^* is the effective mass of CdTe and $\vec{\sigma}$ is the vector of the Pauli matrices.
We do not consider orbital effects of the magnetic field here and therefore omit the magnetic vector potential in the kinetic energy term, i.e. $(\vec{p} - e\vec{A}) \to \vec{p}$. This approximation is valid if the cyclotron radius is much larger than the relevant length scales at experimental stray field strengths. The stray field texture in the plane of the 2DES is further approximated with a helical field as given by

equation 5.7. Solving equation 5.12 in the leads (where the total magnetic field $B_{tot} = B + B_s$ is present) yields the dispersion relation

$$E_{n,\sigma}(k_x) = \frac{\hbar^2 k_x^2}{2m^*} + E_n + \frac{\sigma}{2}\mu_B g_{\mathit{eff}}(B + B_s) \tag{5.14}$$

for the longitudinal wavenumbers k_x and the corresponding spin eigenstate σ. Here, E_n are the eigenenergies of a one-dimensional infinite potential well which arise due to the finite width of the sample; the set (n, σ) uniquely defines a spin channel.

The overall conductance is now calculated employing the Landauer-Buttiker formula (eq. 5.11). Since states with different transverse channel numbers do not couple ($|t_{nm}^{\sigma\sigma'}|^2 = 0$ for $n \neq m$) the problem reduces to a one-dimensional one for a number of N independent channels. For a particular channel (n, σ) the spatially inhomogeneous Zeeman coupling induces transitions between different spin-states $\sigma \to \pm\sigma$, which we investigate with the help of the Landau-Zener model [137]. As the stray field oscillates slowly on the time scale defined by Larmor precession, spin aligns with the helical stray field and transport therefore is adiabatic. This is expressed by the adiabaticity parameter $Q = \omega_L a/(2\pi v_{F,x}) > 1$ which can be derived from above considerations (see supplement to ref. [141]).

In the absence of an external magnetic field the Zeeman splitting for a pair of spin states (see fig. 5.17) is constant, $E_Z = \pm\frac{1}{2}\mu_B g_{\mathit{eff}} B_s$, and no transitions between these states occur. Therefore the transmission probability of a spin is 1 for each of the N ballistic channels, resulting in a total conductance of $G = N \cdot e^2/h$. In the presence of an external magnetic field however, Zeeman splitting depends on x, as given by eq. 5.8. The total field amplitude has local minima midway between adjacent stripes, as depicted in the middle panels of fig. 5.18. For simplicity, let us consider only one of these minima: All spin-compensated pairs of states can be shown to give rise to a background conductance which is unaffected by the magnetic field texture. But in the case of spin-polarized channels, diabatic transitions from the occupied lower Zeeman band to the unoccupied upper one may occur with probability P_n, giving rise to signatures in the magnetoresistance. After a diabatic transition the kinetic energy of the electron is too small to overcome the rising Zeeman barrier for the new spin state, leading to a backreflection and thus diminishing transmission (see fig. 5.22a). These spin-polarized channels Δ_s hence give a magnetic field dependent contribution to the conductance of

$$\delta G = \frac{e^2}{h} \cdot \sum_{n=N-\Delta_s+1}^{N} (1 - P_n). \tag{5.15}$$

Within the Landau-Zener model, the probability P_n for a transition scales roughly inversely like the distance of the energy levels at the (avoided) crossing [137]. If the distance between these energy levels is large, P_n is low and transport is to a good approximation adiabatic. However, if the energy levels cross, $P_n = 1$ and

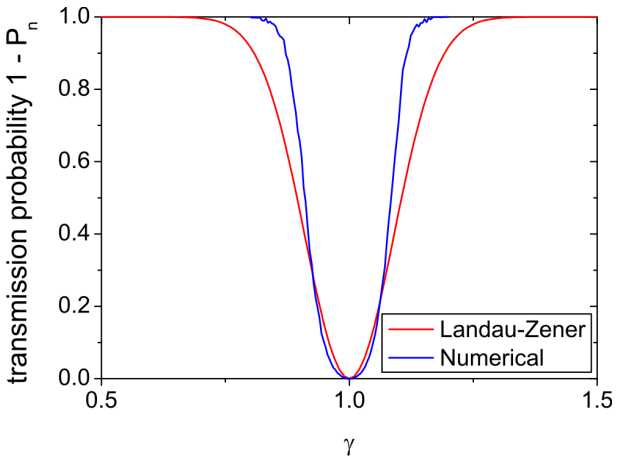

Figure 5.21: Spin transmission probability $1 - P_n$ for a ballistic sample as function of $\gamma = B/B_s$. Here, B denotes the homogeneous external magnetic field and B_s the stray field amplitude. Adiabaticity parameter $Q = 40$. The spin transmission is zero when the spin-split bands cross at $\gamma = 1$. Calculations are either done within the Landau-Zener model (eq. 5.15) or with a recursive Green's function algorithm.

the spin transmission is blocked (see fig. 5.18 and fig. 5.21).
In experiments multiple modulations of the stray field are realized due to the large number of ferromagnetic stripes. Qualitatively this does not change the previous model since the corresponding effective Zeeman barriers have a small tunneling probability and interferences between successive Landau-Zener transitions can be neglected. Stray field profiles in experiments however deviate from perfectly helical fields. Nevertheless, for large Q the mechanism of diabatic transitions presented above applies analogously to global minima of the amplitudes of arbitrary magnetic field profiles along the transport direction, yielding corresponding maxima in magnetoresistance traces.

Numerical Calculations

In numerical calculations we use a recursive Green's function (RGF) algorithm based on a tight-binding discretization of the system [144]. The transmission coefficients of transport modes $t_{nm}^{\sigma\sigma'}$ are calculated within the RGF algorithm and conductance G is then obtained from the Landauer-Buttiker formula (eq. 5.11). We model the sample either with or without disorder[4] and assume the stray field to be helical with amplitude B_s (cf. eq. 5.7). Since source and drain leads are partially covered by the magnetized stripes (see fig. 5.7), they are assumed to exhibit a uniform spin polarization due to the total magnetic field $B_{tot} = B + B_s$. Again we neglect orbital effects due to the magnetic vector potential $\vec{A}$.
We have above presented an intuitive (ballistic) 1D model for spin transistor action via tuning of adiabaticity. At $B = B_s$ all spin-polarized channels are blocked due to diabatic transitions. In order to probe the validity of this argument also in two dimensions we used the RGF method and found that the very same mechanism causes the resistance increase in 2D geometries: All spin-polarized channels are blocked (see fig. 5.22a).

[4] Anderson-like disorder model [145], accounting for spin-independent scattering processes.

Conclusions

Calculations show that the probability of a diabatic transition to the upper Zeeman band is finite even if there are no degeneracy points in the energy bands. A diabatic transition becomes increasingly probable as the distance between the Zeeman-split levels at the closest approach decreases or transport velocity $v_{F,x}$ increases [146]. The latter case merely reflects decreasing adiabaticity due to a fast perturbation as discussed by Landau and Zener [137]. The periodic stripe grating forms a spatially repeating sequence of potential transition points which enhances the probability of a diabatic transition. As a consequence, the resistance peaks broaden as shown by transport calculations in fig. 5.22a.
In addition to spin effects caused by the Zeeman coupling the magnetic field gives rise to orbital effects due to the magnetic vector potential $\vec{A}(x)$ which we have neglected so far. The full Hamiltonian is then given by

$$\hat{H} = \frac{1}{2m^*}\left(\vec{p} - e\vec{A}(x)\right)^2 + \frac{1}{2}g_{\mathit{eff}}\mu_B\left(\vec{B} + \vec{B}_s(x)\right)\cdot\vec{\sigma}. \tag{5.16}$$

Spin transport in the presence of the orbital part shows a complex dependence on the geometry of the system. Preliminary numerical transport calculations indicate that the magnetoresistance peaks may be enhanced due to a combination of orbital and spin effects (see fig. 5.22b). This may explain why the stability of spin transistor action in experiments is better than in calculations which include only the Zeeman energy.
Let us stress here that the number of modulation stripes does not play any role in our theoretical calculations, i.e. one degeneracy point is sufficient of block spin transmission. This situation however changes when taking into account orbital effects. First results indicate increasing peak heights with more degeneracy points being present.
The influence of orbital effects on the spin blocking peak heights in the presence of disorder is going to be addressed in future studies.

5.3.4 Non-Helical Stray Fields

The ballistic model introduced in chapter 5.3.2 can be generalized to non-helical stray fields. As already discussed the actual stray field profile of the magnetized stripes is anisotropic, i.e. different for x and z direction (see fig. 5.5). Consequently the spin blocking peak positions should depend both on the stripe periodicity as well as on the angle of stripe magnetization. To further illuminate those anisotropy effects we have conducted additional experiments which show the non-helicity of the stray field and once more confirm that the resistance peaks observed in experiment stem from spin transmission blocking: On the one hand we studied samples with different stripe periodicities a, ranging from 0.5 μm to 8 μm. As an

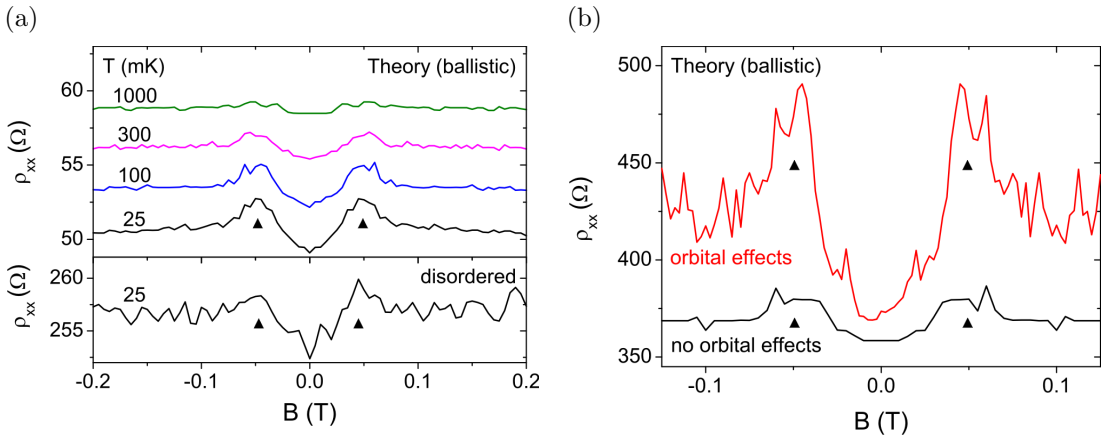

Figure 5.22: (a) Calculated magnetoresistance traces in a system which models sample C ($a = 1$ μm) with a ballistic model (upper panel) and a disordered transport model with a mean free path $l_{mfp} = 4$ μm (lower panel). Compare the good agreement with experiment (fig. 5.13). (b) Computed magnetoresistance peaks (filled triangles) in the presence of orbital effects for a 8 μm long ballistic model system (red trace). Temperature $T = 25$ mK and $a = 1$ μm. The reference curve (black line) depicts the spin blocking peaks in the absence of orbital effects for the very same system.

example, data are shown for sample C at a tilt angle of $\theta = 45°$ (fig. 5.23) where the resistance peaks are found to be most pronounced (compare fig. 5.14). The peak positions indeed shift to larger $B_{C,\pm}$ values as the modulation period a is increased. This is in contrast to the behavior expected for purely helical stray fields where no modulation period dependence would be present. On the other hand the dependency of magnetoresistance ρ_{xx} on tilt angle θ was measured for the samples under investigation, as has already been partially considered in fig. 5.14 for the individual case of sample C and a modulation period of 1 micron. In addition, the stray field B_s of the stripes was calculated within the dipole approximation for different values of θ and a (see section 5.1). This yields the positions $B_{C,\pm}$ of the spin blocking peaks as field values where zeros form in the total field, i.e. $B_{tot} = 0 = B + B_s$ (degeneracy point condition). The theoretical data for the peak separation $\Delta = B_{C,+} - B_{C,-}$ are compared to the corresponding values extracted for samples B and C in fig. 5.24 revealing the expected anisotropy both on modulation period a and tilt angle θ. Note that no fit parameters are used in the calculations of the degeneracy point. The excellent agreement between model and experiment gives further evidence that the observed magnetoresistance peaks originate from reduced spin transmission.
A similar kind of anisotropy was also found in an experiment where the stripes are first magnetized along the x direction but the probing external magnetic field is then swept while keeping it perpendicular to the plane of the 2DES (see fig. 5.25, using sample C as an example). In detail the measurements are performed as follows: First, the sample is tilted to its $\theta = 90°$ position where the external

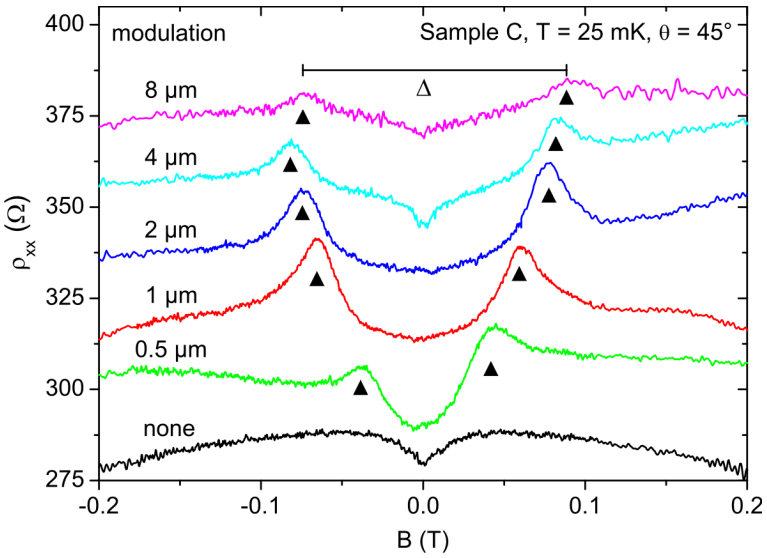

Figure 5.23: Sample C magnetoresistance traces for various modulation periods a at $\theta = 45°$ tilt. The shift of the spin blocking peaks (filled triangles) with increasing a is related to the anisotropy of the stray field. Peak separation is denoted by Δ. All curves are shifted for clarity, except the black one. Temperature $T = 25$ mK.

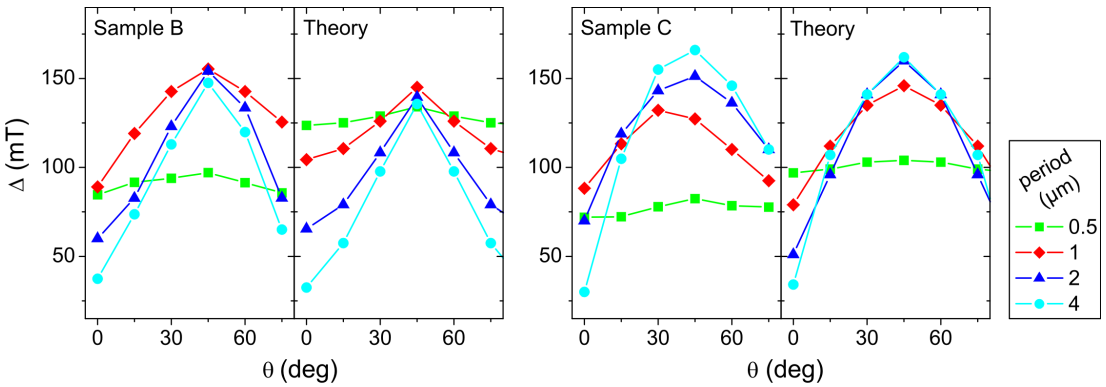

Figure 5.24: Resistance peak separation $\Delta = B_{C,+} - B_{C,-}$ in samples B and C compared to values obtained from ballistic theory and micromagnetic simulations for various tilt angles θ and modulation periods. The results reflect the anisotropy of the stray field. Experimental data are extracted from $T = 25$ mK measurements.

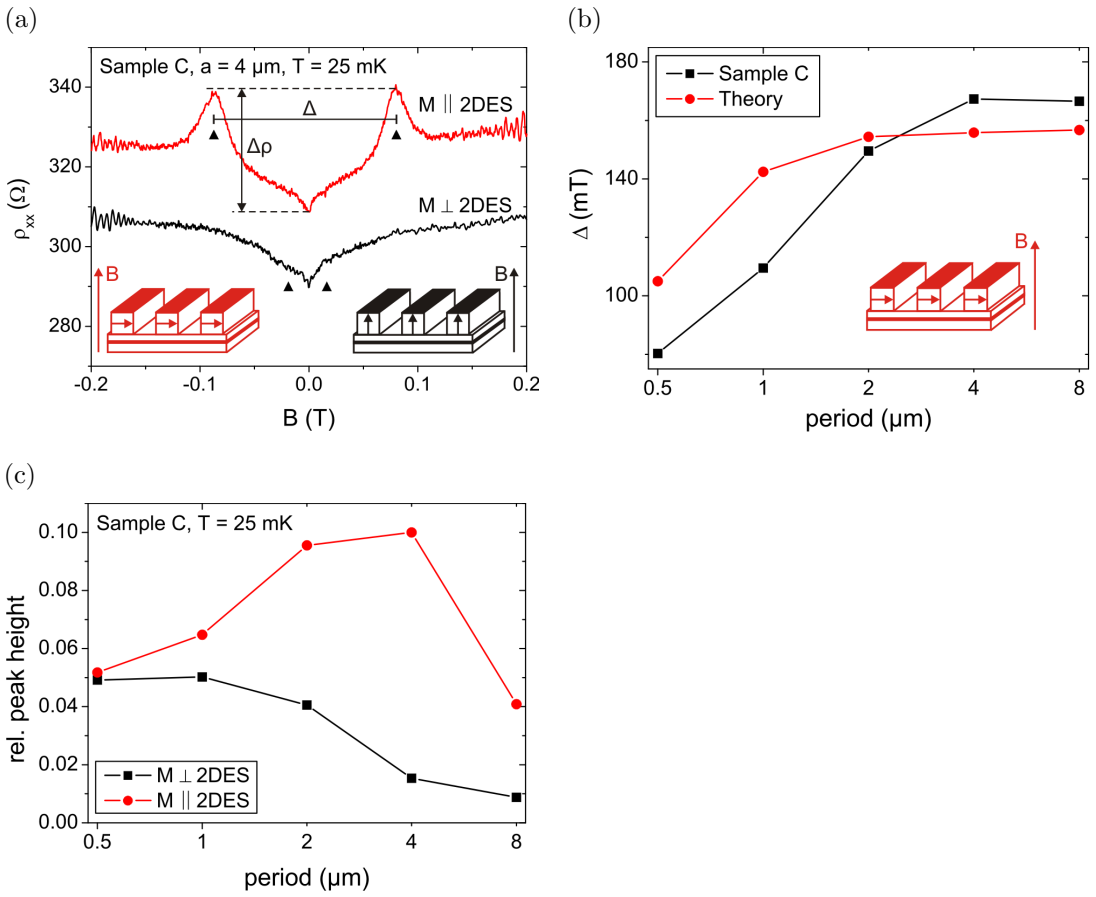

Figure 5.25: (a) Longitudinal resistance ρ_{xx} of sample C at $T = 25$ mK and $a = 4$ μm modulation. The traces are recorded at different magnetization directions of the stripes, either perpendicular or parallel to the 2DES while the external magnetic field always is perpendicular to it. Note the strong enhancement of the spin blocking peak height $\Delta\rho$ in the case of parallel stripe magnetization. Red trace shifted for clarity. (b) Resistance peak separation Δ in sample C for the configuration shown in the inset: stripe magnetization in the plane of the 2D electron gas and a perpendicular external magnetic field. The theoretical values are obtained within the magnetic dipole approximation. (c) Relative spin blocking peak height as function of modulation period a in sample C for perpendicular and parallel stripe magnetization at $T = 25$ mK. Peak heights are strongly enhanced in parallel magnetization configuration for $a > 1$ μm. Their 1 K background is subtracted.

magnetic field is parallel to the surface but perpendicular to the stripe axis. The field is then ramped up to 8 T to magnetize the stripes along the x direction and subsequently back to 0 T. Due to their large coercive field of about 1.2 T the stripes do not change their magnetization configuration and the sample can be tilted back to $\theta = 0°$. The grating is now magnetized parallel to the electron gas sheet while the external field points perpendicular to it (see fig. 5.25b, inset). For data acquisition the field is typically swept between +0.5 T and −0.5 T, well below the limit of 1.2 T.
The height of the spin blocking peaks as well as their separation Δ are found to be strongly enhanced for a stripe magnetization parallel instead of perpendicular to the 2DES plane, especially in the case of $a > 1$ μm (see fig. 5.25a and compare fig. 5.25b and $\theta = 0°$ data, sample C of fig. 5.24). Those effects are studied in detail by figs. 5.25b and 5.25c where the peak separation as well as their (mean) relative height $\Delta\rho/\rho$ is plotted as a function of modulation period. The relative peak height is given by

$$\frac{\Delta\rho}{\rho} = \frac{\Delta\rho_{25\text{ mK}} - \Delta\rho_{1\text{ K}}}{\rho_{xx}(B=0)}, \tag{5.17}$$

where $\Delta\rho = \rho_{xx}(B_{C,\pm}) - \rho_{xx}(B = 0)$ is the mean peak height at $B = B_{C,\pm}$. Since the samples under investigation typically display a small dip in longitudinal resistance even at elevated temperatures (see e.g. $T = 600$ mK trace in fig. 5.13), we subtract this 'background signal' from the measured peak heights at $T = 25$ mK. The background is estimated from the 1 K data where we assume the spin splitting to be so small that only spin-compensated bands exist below the Fermi energy. Above experiments again link the resistance peaks at $B_{C,\pm}$ to a reduced spin transmission through the devices.

5.3.5 Device Performance

In the ballistic model all spin-polarized transport modes are blocked at $B = B_s$ which increases the resistance of the sample. A single degeneracy point in the Zeeman bands is sufficient to block all spin transmission, hence the peak height $\Delta\rho/\rho$ is not expected to depend on the number of modulations. This is in line with measurements at different modulation periods a at a fixed device length of 50 μm, i.e. for a varying number of stripes (see fig. 5.23). The experimental data collected on sample C at 45° tilt (most pronounced spin blocking peaks at this angle) are summarized in fig. 5.26a. Peak heights are rather independent of the period of stripe modulation, except for the 8 μm case which is likely due to the highly anisotropic stray field at this large period. It indeed fluctuates rapidly between 10 mT and 90 mT (see fig. 5.26b) such that spins may not be able to follow this field everywhere in the sample. This constitutes a diabatic event and the spin state consequently is a superposition of local spin-up and -down states.

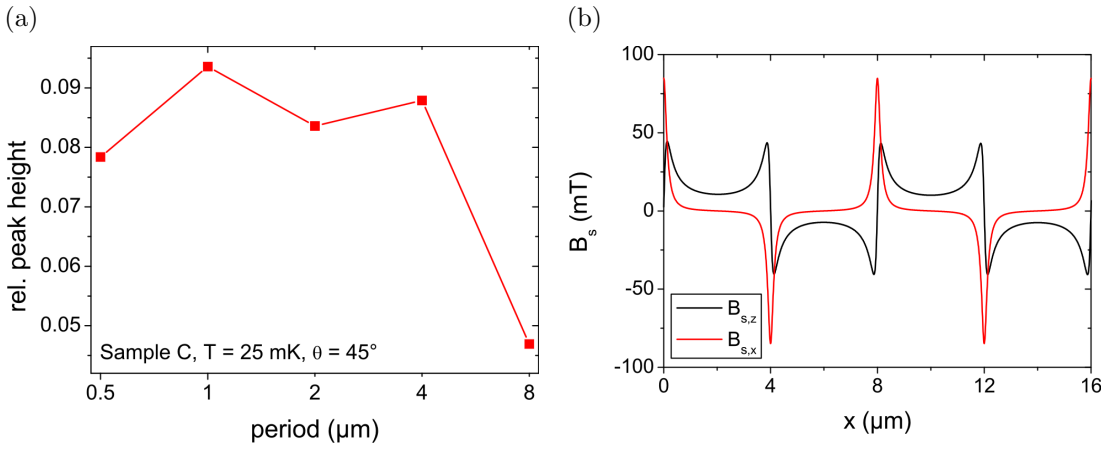

Figure 5.26: (a) Relative (mean) spin blocking peak heights extracted from fig. 5.23: Sample C, $T = 25$ mK and $\theta = 45°$. The peak heights are nearly independent of modulation period a. Only the case $a = 8$ μm shows reduced peaks, probably as a consequence of the highly anisotropic stray field. Due to a lack of high T data the 1 K background is not subtracted here; typical reductions are of the order of 3%. (b) Computed stray field profile of a 75 nm thick Dy grating of period $a = 8$ μm, as present 100 nm below the surface. The field is highly anisotropic and rapidly fluctuates between 10 mT and 90 mT.

Therefore spin starts to precess, a situation which is identical to a transition to the upper Zeeman band. If this transition leads to a state which is higher in energy than E_F, backscattering occurs and hence spin is blocked with a certain probability. This may happen independent of whether the external field is tuned to $B = B_s$ or not. When states are blocked due to the above process, fewer remain to undergo the spin blocking at $B = B_s$ and thus peaks become less pronounced. Similar results are obtained at $\theta = 0°$ (see fig. 5.25c, black data points) where again the peaks are diminished at highest modulation periods.
The effect of disorder on the height of the spin blocking peaks is studied in detail in fig. 5.27 where $\Delta\rho/\rho$ is plotted as a function of temperature. The ballistic model gives an estimate $E_Z(T, 2B_s)/(4E_F)$ for the relative magnetoresistance peak height (red line in fig. 5.27) assuming that the stray field contributes to the spin polarization of the leads (source and drain are partially covered by the stripes as shown in fig. 5.7). Consequently, the temperature scaling of the peaks is governed by the *s-d* exchange contribution to the CdMnTe g-factor, as was already discussed in chapter 5.2.2. In the presence of disorder however, diabatic transitions are perturbed and peak heights are hence reduced. But contrary to our numerical transport calculations, disorder is not found to strongly affect the measured peak heights in sample C: The experimental values are comparable to our disorder model at an electron mean free path of $l_{mfp} = 4$ μm (green data points in fig. 5.27). However, the peaks disappear in the calculations at $l_{mfp} = 0.65$ μm which is equal to the real mean free path in sample C. This can on the one hand be due to an insufficient disorder modeling and has to be further investigated. But the fact that

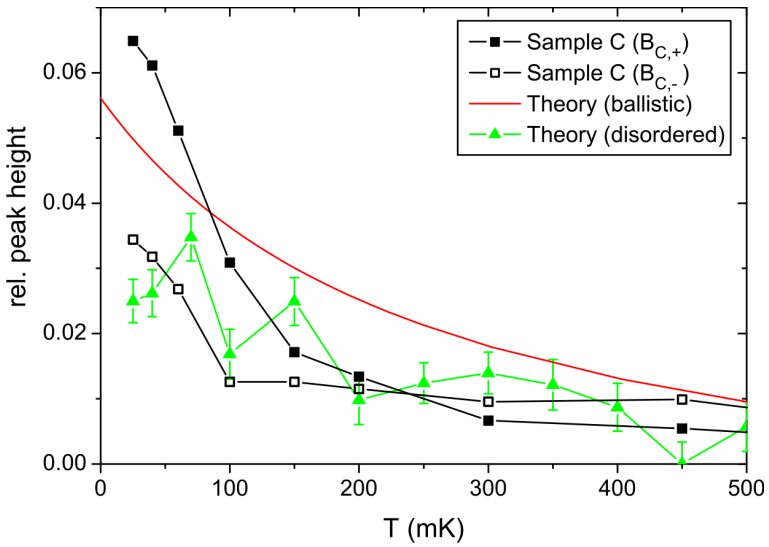

Figure 5.27: Relative resistance increase as a function of temperature in sample C with 1 micron period modulation (filled/open squares represent spin blocking peaks at $B_{C,+}$ and $B_{C,-}$, respectively). Theoretical data obtained from the ballistic model (solid red line) and from a model which includes disorder (green triangles) are shown in addition. In the latter case the transport mean free path is $l_{mfp} = 4$ μm and the device length is 18 μm. The corresponding reference values of the spin-compensated limit are estimated from the resistances at 1 K.

peak heights at lowest temperatures are higher than theoretically predicted might also be related to orbital effects. Those have been neglected in our transport calculations which only include the Zeeman energy. Preliminary studies (see supplement to ref. [141]) indicate that the combination of orbital and spin effects (Zeeman coupling) can contribute to a better than expected device performance. Nevertheless, experiments indicate that adiabatically transported spin is stable over device distances of 50 μm which are much longer than electron mean free paths in the samples (between 0.47 and 1.39 μm). Our findings can therefore be contrasted to Datta-Das spin transistor action which is totally disrupted if the mean free path is much shorter than the device length.

Chapter Summary

A simple ballistic model allows to explain the emergence of distinct resistance peaks in magnetically modulated CdMnTe QW structures. The induced helical pattern of spin polarization is maintained by keeping spin transport in the adiabatic regime where the stray field changes slowly on the time scale defined by Larmor precession and electron spins therefore align with it. By applying an external magnetic field spin transport is locally tuned from adiabatic to diabatic, hence making Landau-Zener transitions to higher energy states possible. This situation is related to a backreflection of charge carriers at these particular positions leading

to a reduced channel conductance. The studied CdMnTe-based devices therefore represent an alternative way to realize spin transistor action which employs the regulation of spin transport adiabaticity.
Based on the anisotropy of the real stray fields we provide additional experimental evidence that the observed magnetoresistance peaks are related to the proposed spin blocking mechanism. We find excellent agreement between measurements and theory, further supporting our claim that adiabatically transported spin is stable over device distances of 50 μm. Contrary to numerical calculations the spin blocking peak heights are not found to be strongly affected by disorder. Instead, experiments yield a better than expected device performance at lowest temperatures. These observations may be contrasted to Datta-Das spin transistor action which is disrupted upon the presence of disorder.

5.4 Additional Experiments

The scope of this chapter is on the one hand to briefly summarize additional experimental results obtained on dysprosium stripe arrays and on the other hand to study the performance of spin transistor devices equipped with iron gratings.

5.4.1 Random Stray Fields and Demagnetized Stripes

Magnetotransport influenced by random stray fields (achieved via a random spatial distribution of ferromagnetic stripes) has already been investigated in connection with magnetic commensurability effects in GaAs heterostructures [147]. Here we use an analog setup to probe for effects on our CdMnTe-based spin transistor prototypes.
A random stripe distribution is simply obtained by defining their positions along the transport direction (x axis) by a set of uniform random numbers (see fig. 5.28). This allows stripes to overlap and to form clusters resulting in an aperiodic and strongly fluctuating stray field profile. The mean period $\langle a \rangle$ of such randomly distributed stripes is defined by

$$\langle a \rangle = \frac{L_x}{N}, \tag{5.18}$$

where $L_x = 70$ μm is the range over which the N stripes of width $\langle a \rangle / 2$ are distributed.
Fig. 5.29 displays magnetotransport results obtained on sample A, equipped with random arrays of dysprosium stripes of periods $\langle a \rangle = 1$ μm and 2 μm. The corresponding data of unperturbed reference structures with identical period $a = \langle a \rangle$ are shown in black. In the presence of a randomly fluctuating field the spin blocking peaks are found to be strongly diminished for all periods investigated. Similar

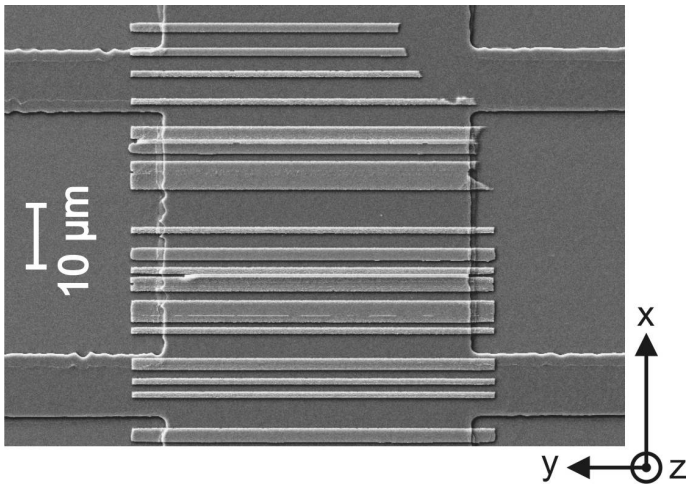

Figure 5.28: Electron micrograph showing a spin transistor with a grating of randomly distributed dysprosium stripes of mean period $\langle a \rangle = 2$ μm. The stripe positions along the x axis are defined by random numbers, hence allowing for overlapping and cluster formation.

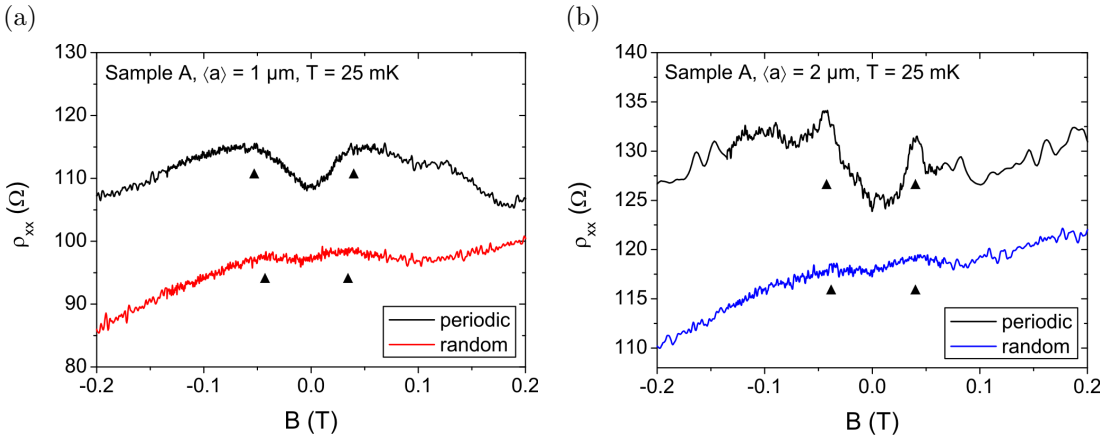

Figure 5.29: Longitudinal resistances ρ_{xx} collected on spin transistor devices with randomly distributed dysprosium stripes of mean period $\langle a \rangle = 1$ μm (a) and $\langle a \rangle = 2$ μm (b). Sample A, $T = 25$ mK. The corresponding reference traces in the case of unperturbed gratings of the same period are shown in black. Curves are shifted for clarity, except the lowest ones.

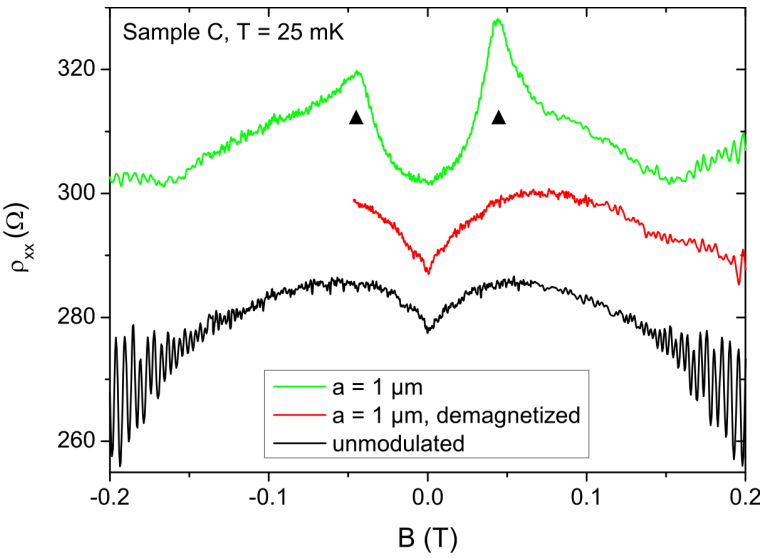

Figure 5.30: Longitudinal magnetoresistance ρ_{xx} of sample C spin transistor devices with dysprosium stripes of period $a = 1$ μm. The green and the red curve represent the two cases - perpendicularly magnetized stripes and demagnetized ones, respectively. Reference data of an unpatterned device is shown in addition. $T = 25$ mK. Traces are shifted for clarity, except the black one.

to the case of reduced peak heights at $a = 8$ μm (see section 5.3.5) rapid stray field fluctuations make diabatic transitions to the upper Zeeman band possible, even if $B \neq B_s$. This reduces the number of states to be blocked at $B = B_s$ which in turn results in diminished peaks.

Another type of experiment addresses the case of demagnetized (periodic) stripe gratings: By sweeping the external magnetic field around $B = 0$ T with decreasing amplitude, e.g. $+8$ T $\rightarrow -4$ T $\rightarrow +2$ T $\rightarrow \ldots \rightarrow 0$ T, one arrives at a situation where the stripe magnetization vanishes on average. Hence, the stray field is quenched and the stripes are not expected to affect magnetotransport any longer. Only strain related effects due to different thermal expansion coefficients of semiconductor and ferromagnet should persist. After the demagnetization process we therefore should come across a situation which is essentially identical to the one of an unpatterned reference structure. This prediction is indeed evidenced by fig. 5.30 depicting magnetotransport data collected on sample C for a (periodic) dysprosium stripe array of period $a = 1$ μm. The green trace is recorded after the usual pre-magnetization of the stripes in a field of 8 T strength, while the red one displays the case of zero stray field (the sweep is started from -50 mT after the demagnetization process). Since the latter curve very well coincides with the black one (unpatterned reference device) the following conclusions can be drawn: First, we can effectively demagnetize the dysprosium stripes and thus probe the zero stray field situation on the very same device without the need for

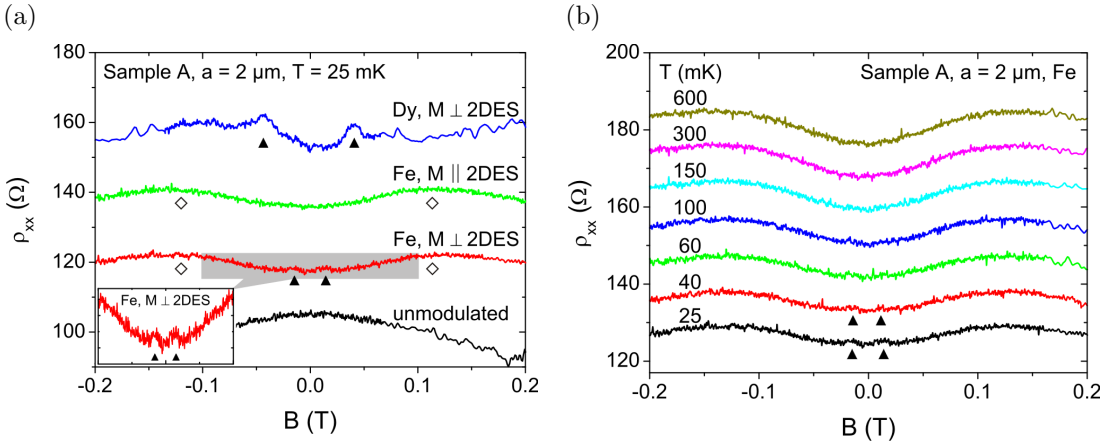

Figure 5.31: Spin transistor prototypes with iron stripe gratings. Sample A, $a = 2$ μm. Traces are shifted for clarity, except the lowest ones. (a) When replacing dysprosium with iron as a stripe material the spin blocking peaks (filled triangles) become strongly attenuated (perpendicular stripe magnetization, red trace) and are shifted to lower fields. In addition, a positive magnetoresistance around $B = 0$ T (open diamonds) develops. The situation however changes - i.e. the low-field ρ_{xx} peaks vanish - if the stripes are magnetized parallel to the 2DES plane (compare red and green traces and differences to fig. 5.25a). This observation rather suggests the absence of the spin-blocking mechanism. In all cases the external field is applied perpendicular to the sample, as depicted in the inset of fig. 5.25a. Temperature $T = 25$ mK. The inset enlarges the highlighted region where possible spin-blocking peaks emerge for a stripe magnetization perpendicular to the 2DES plane. (b) The presence of a helical spin polarization is also not clearly evidenced by the temperature dependence of the low-field longitudinal resistance ρ_{xx} either. Peaks seem to be quenched at $T > 60$ mK.

any reference. Second, no strain induced magnetoresistivity effects are present in our samples. This is in agreement with predictions based on the investigation of magnetic commensurability oscillations in our samples, where minima in ρ_{xx} are found to be close to the magnetic flatband positions (see section 5.2.1).

5.4.2 Iron Stripe Gratings

In a continuative experiment we have studied spin transistor performance when replacing dysprosium by iron as a stripe material. The results obtained on sample A with an iron grating of period $a = 2$ μm are summarized in fig. 5.31. In contrast to the case of dysprosium, magnetic modulation by iron stripes does not result in the formation of pronounced spin-blocking peaks. In perpendicular magnetic fields at $T = 25$ mK (see fig. 5.31a, red trace) we observe two extremely low peaks at roughly ± 17 mT (filled triangles) and a rather flat but extended positive magnetoresistance, saturating at values of about 120 mT (open diamonds). The first might indeed originate from spin transmission blocking as their position coincides well with the one derived from micromagnetic simulations ($B_{C,\pm} = \pm 19$ mT). For

the calculations we roughly estimate the remanence magnetization of the iron stripes to $M_R = 0.4 \cdot 10^6$ A/m, about one fourth of the material's bulk saturation magnetization value (a similar scaling is observed for the case of dysprosium stripes, see discussion in section 5.1).
Any relation between this tiny low-field ρ_{xx} texture (about 1 Ω peak height) and the presence of a helical spin polarization should be detectable when altering the magnetization direction of the ferromagnetic stripes. Similar to previous results on dysprosium gratings (see section 5.3.4 and fig. 5.25a) a drastic enhancement of the low-field features is expected if the stripe magnetization is aligned parallel to the 2DES plane. However, experiments contradict this behavior (fig. 5.31a, green trace), i.e. the spin-blocking peaks are vanished in the parallel field configuration. This rather suggests the absence of the blocking mechanism.
Even the temperature dependence of the longitudinal resistance (see fig. 5.31b) cannot help to clarify the origin of the (possible) peaks at ±17 mT. We find them to be diminished for $T > 60$ mK - in line with the observed strong attenuation of peak heights in dysprosium modulated devices at elevated temperatures. As the ρ_{xx} features are extremely weakly developed here, results however remain questionable.
The low spin blocking peaks - if present at all - consequently indicate the lack of a significant spin polarization in case of magnetic modulation by iron stripes. It is probably due the following reasons:

- In comparison to dysprosium, iron features a lower saturation magnetization of $M_s = 1.74 \cdot 10^6$ A/m (bulk) which causes reduced stray field amplitudes (estimated to about 19 mT in our samples). As a result spin polarization and hence peak heights are strongly reduced. The latter are expected to emerge at $B_{C,\pm} = \pm 19$ mT.
- Furthermore, iron exhibits a minor coercive field (0.1 to 100 mT) than dysprosium [148]. The stripe magnetization hence may more easily flipped when probing the resistance peaks in the vicinity of $B = 0$ T, again leading to a reduced spin polarization.

In a nutshell, the spin polarization induced by iron stripe gratings is too low to ensure proper spin transistor action in our CdMnTe devices. Future studies therefore should keep dysprosium as a stripe material, at least as long as experiments are performed at temperatures well below its Curie temperature. Only in case semiconductors with giant g-factors at elevated temperatures become accessible, one needs to search for a suitable ferromagnet to replace dysprosium.

Chapter Summary

The performance of spin transistor devices has been studied in case of stray fields which are generated either by stripes made of iron or by a disordered/perturbed

dysprosium grating. The latter utilizes randomly distributed stripes to create a strongly fluctuating stray field. Locally, spins cannot follow this field and hence adiabaticity is broken. As a consequence, there is a certain probability for spins to undergo a transition to the upper Zeeman band, even if the spin blocking condition $B = B_s$ is not fulfilled. These transitions reduce the number of states to be blocked at exactly $B = B_s$ thus causing reduced peak heights.
The spin blocking peaks are found to be extremely weak or even absent when using iron instead of dysprosium as a stripe material. We attribute this to the lower saturation magnetization and coercive field of iron which does not give rise to a sufficiently high spin polarization in our CdMnTe samples. For future experiments we hence recommend to employ dysprosium gratings, as long as large g-factors are accessible via low temperatures anyway.

5.5 Summary - Spin Transistor Action

We demonstrate an experimental setup based on a CdMnTe diluted magnetic semiconductor quantum well device where current is controlled by tuning adiabaticity of spin transport with a magnetic field. The degree of adiabaticity is monitored electrically in the conductance in contrast to interference measurements [149, 150] of geometrical (Berry) phases [151] associated with adiabatic spin evolution. Our proposed spin transistor devices consist of only three simple building blocks: a high-mobility 2DES with a giant Zeeman splitting, a grating of ferromagnetic stripes nanopatterned on top of the sample and a homogeneous magnetic field generated by a superconducting coil.
We find that device operation is robust against disorder and that current modulation is large in comparison to InAs based devices [152]. Our results thus demonstrate an alternative way to realize spin transistor action, distinct from the approach by Datta and Das which relies on spin precession in a gate-controlled spin-orbit field [128]. In contrast, stability is enhanced by transporting spins in the adiabatic regime in our devices while regulation of the degree of adiabaticity allows for switching between 'on' and 'off' states. In contrast to the Datta-Das concept our approach is exceptionally tolerant against disorder. Our proof of concept device shows significant source-drain resistance modulation of up to $\approx 10\%$ due to tunable spin transmission and this is expected to be drastically enhanced in materials with high spin polarization. Furthermore, the homogeneous magnetic field - provided here by coils - might be replaced with a magnetic gate which is switched by spin-torque [153]. This would make the device purely electrically controlled. As we use a paramagnetic material our device operates only at low temperatures. However, we stress that our design concepts are not restricted to a particular choice of materials, temperature, methods of spin injection, manipulation as well as detection. To transfer our concept to higher temperatures requires

employing exchange splitting or spin-orbit splitting rather than Zeeman splitting. Possible material systems in which exchange interaction can be tuned by means of an electric field involve e.g. magnetic semiconductors [154]. Our proposed ideas can therefore be used to design a class of highly efficient spintronics applications.

6 Conclusions

In this work we investigate spin effects on the magnetotransport properties of semimagnetic $Cd_{1-x}Mn_xTe$ two-dimensional electron systems. While the first part of this thesis is dedicated to the emergence of the fractional Quantum Hall effect (FQHE) in these quantum structures, the second part focuses on a novel approach to realize spin transistor action. We demonstrate a $Cd_{1-x}Mn_xTe$-based proof of concept device which shows significant source-drain resistance modulation of currently up to 10%.

Within the framework of this PhD we report on the very first observation of the FQHE in both, a non-magnetic CdTe and a semimagnetic $Cd_{1-x}Mn_xTe$ quantum well device. To our knowledge, this constitutes the first demonstration of this effect in the II-VI material family. Furthermore, our results reveal that the formation of fractional Quantum Hall (FQH) states is not inhibited by the presence of magnetic impurities in a quantum structure.
In the studied CdTe specimen we observe fully developed FQH states in the upper spin branch of the lowest Landau level (LL) at filling factors $\nu = 5/3$ and $4/3$. Transport experiments at mK temperatures reveal no significant changes in the associated energy gaps as the Zeeman splitting E_Z is increased by tilting the sample. Such behavior is expected in case of spin-polarized ground states which feature lowest energy excitations that do not involve a spin-flip. Based on the Composite Fermion (CF) approach to the FQHE we show that on the one hand the $\nu = 5/3$ and $4/3$ ground states are fully spin-polarized and that on the other hand the corresponding energy gaps are indeed independent of tilt angle. Our experimental findings are hence a direct consequence of the huge CdTe g-factor which is about 4 times larger than in GaAs. Observations in CdTe are thus contrary to GaAs, where increasing E_Z typically induces changes in the ground states' spin polarization that result in angular dependent energy gaps.
While the formation of FQH states originates from weak electron-electron interaction, the incorporation of magnetic ions, e.g. manganese, gives rise to strong s-d exchange coupling with the charge carriers. This raises the question whether magnetic impurities in a two-dimensional electron system are an obstacle to the emergence of the FQHE; at least, the FQHE has not been reported in a diluted magnetic semiconductor (DMS) so far. CdMnTe is an ideally suited material to search for FQH states in the presence of magnetic impurities, since manganese can easily be incorporated into CdTe-based quantum structures without significantly

degrading electron mobilities and quantum lifetimes. At mK temperatures our DMS specimen indeed features well developed fractional states in the lowest LL at fillings 5/3, 8/5, 7/5 and 4/3. We study the angular evolution of energy gaps associated with these states by activation measurements in tilted magnetic fields of up to 19 T. Tilting the sample is found to induce multiple gap openings and closings which are well explained within a CF-based model that we extend by *s-d* exchange interaction [1] to also cover the characteristics of DMSs. By comparing model and experiment we prove that the *s-d* exchange contribution to the spin splitting crucially affects the angular gap dependence in our DMS specimen. Our CF model allows to extract relevant system parameters, i.e. CF masses, exchange constants and the CF g-factor, which we find to be in a good agreement with previous experiments on GaAs and Si if considering the material characteristics and the quality of our sample.
Since CdMnTe allows to tune its Zeeman splitting to zero at nearly any desired magnetic field value (as a result of *s-d* exchange), it is a perfect system for the investigation of spin-related effects in the FQHE regime. This might for instance help to answer the outstanding question whether the $\nu = 5/2$ state - likely to emerge in CdMnTe with increasing sample quality - could form skyrmions for a vanishing E_Z. As a consequence of skyrmion formation the $\nu = 5/2$ ground state is supposed to turn from fully spin-polarized to unpolarized [40, 127].

Within the second part of this thesis we address an alternative route to realize efficient spin transistor action. Typically, spin transistor designs relying on spin-orbit interaction [128] principally suffer from low signal levels due to limitations in spin injection efficiency and fast spin decay [132]. Here we present an approach to realize spin transistor action in systems where spin information is protected by propagating it *adiabatically*. This is achieved by inducing tunable diabatic *Landau-Zener transitions* that lead to a backscattering of spins and hence allow controlling the transmission of spin-polarized charge carriers through the device, i.e. switching between 'on' and 'off' states. We demonstrate the validity of our approach in a $Cd_{1-x}Mn_xTe$ diluted magnetic semiconductor quantum well structure where efficient spin transport is observed over device distances of 50 μm. The spin backscattering rate is controlled by a combination of a static helical and a variable homogeneous magnetic field. In contrast to other spin transistor designs we find that our concept is exceptionally tolerant against disorder.
Our setup consists of three building blocks: a high-mobility $Cd_{1-x}Mn_xTe$-based 2DES featuring a giant Zeeman splitting, a grating of ferromagnetic stripes on top of the sample and a homogeneous external magnetic field. The ferromagnetic grating is made of 75 nm thick dysprosium stripes, patterned to periods a ranging from 0.5 μm to 8 μm. After pre-magnetization the stripes give rise to an approximately helical stray field in the 2DES plane (field strength $B_s \approx 50$ mT), as determined by SQUID experiments and micromagnetic simulations. Via the giant Zeeman coupling [1] (1 meV in the case of our samples at $B_s = 50$ mT

and $T = 25$ mK) the helical magnetic field translates to a helical pattern of spin polarization with a magnitude ranging between 8% and 15%.
In the presence of the helical stray field the magnetoresistance $\rho_{xx}(B)$ in the low-field limit displays the hallmark of spin transistor action: two distinct peaks at about ± 50 mT. In contrast, the latter do not appear in magnetically unmodulated reference samples where the helical spin polarization is absent. The peaks in modulated structures vanish rapidly with increasing temperature and are no longer recognizable above 1 K. This is in line with the expected T-dependence of the spin polarization of $Cd_{1-x}Mn_xTe$ since the dominant s-d exchange part in the g-factor contributes significantly only at low temperature. This behavior hence confirms a spin-related effect.
The resistance peaks originate from reduced spin transmission through the 2DES channel which we explain within a simple model: We show that in the moving electron's frame of reference the grating's stray field changes slowly on the time scale defined by Larmor precession. Consequently, spin transport in the absence of the external magnetic field is adiabatic and spins align with the local field. However, if the helical field component is equal in amplitude to the homogeneous component, diabatic Landau-Zener transitions to a spin eigenstate above the Fermi energy occur. This causes spin backscattering and an increased channel resistance.
As the actual stray field profile of the magnetized stripes slightly deviates from helical shape the position of the magnetoresistance peaks is dependent on the stripe periodicity as well as on the angle of stripe magnetization. We show that our experimental data coincide well with theoretical predictions, thus confirming again that the resistance peaks stem from spin transmission blocking. Our proof of concept device shows significant source-drain resistance modulation of up to 10% and this is expected to be drastically enhanced in materials with high spin polarization.
As we use a paramagnetic material our device operates only at low temperatures. However, we stress that the design concepts are not restricted to a particular choice of materials, temperature, methods of spin injection, manipulation as well as detection. To transfer our concept to higher temperatures requires employing exchange splitting or spin-orbit splitting rather than Zeeman splitting. Possible material systems in which exchange interaction can be tuned by means of an electric field involve e.g. magnetic semiconductors [154].

Appendix

Recipes

Mesa Etching

- Hallbars are defined by standard optical lithography.
- Reactive Ion Etching ($1.3 \cdot 10^{-5}$ mbar base pressure):
  - 5.5 min CH_4/H_2: Gas-flow 5/40 sccm, 50 mTorr chamber pressure, 150 W RF power.
  - 3 min O_2: Gas-flow 100 sccm, 100 mTorr chamber pressure, 50 W RF power.

Ferromagnetic Stripe Gratings

- Double-layer EBL resist:
  - Layer 1: PMMA 50k 9%, baking: 10 min, 90 °C.
  - Layer 2: PMMA 950k 2%, baking: 15 min, 90 °C.
- EBL: 15 kV acceleration voltage, area dose: $250 - 270$ $\mu C/cm^2$, development: 75 s IPA (in ultrasonic bath).
- Sputtering ($2 \cdot 10^{-10}$ mbar base pressure):
  - 75 nm dysprosium: 9 sccm Ar-flow, 50 W sputter power.
  - 6 nm aluminum: 6 sccm Ar-flow, 25 W sputter power.
- Lift-off in acetone.

Ohmic Contacts

- Scratch contact pads slightly with needle to break up oxide layer.
- Press freshly cut indium flakes on contact pads.
- Anneal approximately 5 s with soldering iron.

Appendix

Wafer Material

The samples investigated are quantum well structures based on the II-VI semiconductor $Cd_{1-x}Mn_xTe$. They were all grown in the lab of T. Wojtowicz (Polish Academy of Sciences) in Warsaw.

Table 6.1: List of all heterostructures utilized in this PhD. Here, d denotes the distance between 2DEG and sample surface and x the manganese concentration. The column 'digital' specifies the mode of manganese incorporation into the QW: digital vs. homogeneous alloy. Values of carrier density n_s and electron mobility μ are obtained after illuminating the sample with a yellow LED.

wafer no.	sample	QW (nm)	spacer (nm)	doping (nm)	cap (nm)	d (nm)	digital	x (%)	n_s (10^{11} cm^{-2})	μ (10^5 cm^2/Vs)
013108A	A	20	20	5	50	85	y	0.55	4.18	1.30
030607A	B	10	15	5	50	75	y	1.1	4.99	0.40
020508A	C	30	30	5	50	100	n	1.0	2.77	0.75
092106A	D	10	15	3	75	98	y	0.70	4.55	0.43
013008A	F1	20	20	5	50	85	-	0.0	4.53	2.60
101008A	F2	30	30	3	50	98	n	0.24	3.95	1.15

Bibliography

[1] J. Furdyna, *J. Appl. Phys.* **64**, R29 (1988).

[2] J. Kossut, *Acta Phys. Pol. A* **100**, 111 (2001).

[3] J. Kossut, J. Furdyna, *Diluted Magnetic Semiconductors*, volume 25 of *Semiconductors and Semimetals*, Academic Press, San Diego, 1987.

[4] T. Moss, editor, *Handbook of Semiconductors*, volume 3b, p. 1251, North Holland, Amsterdam, 1994.

[5] N. Szwacki, E. Przezdziecka, E. Dynowska, P. Boguslawski, J. Kossut, *Acta Phys. Pol. A* **106**, 233 (2004).

[6] S. Wei, A. Zunger, *Phys. Rev. B* **35**, 2340 (1987).

[7] A. Waag, H. Heinke, S. Scholl, C. Becker, G. Landwehr, *J. Cryst. Growth* **131**, 607 (1993).

[8] O. Madelung, U. Roessler, M. Schulz, *Landolt-Boernstein. New Series*, volume 41b, Springer, Berlin, 1999.

[9] B. Larson, K. Hass, H. Ehrenreich, A. Carlsson, *Phys. Rev. B* **37**, 4137 (1988).

[10] J. Spalek, A. Lewicki, Z. Tarnawski, J. Furdyna, R. Galazka, Z. Obuszko, *Phys. Rev. B* **33**, 3407 (1986).

[11] R. Triboulet, P. Siffert, editor, *CdTe and Related Compounds*, volume 1, p. 143, Elsevier, Amsterdam, 2010.

[12] J. Gaj, R. Planel, G. Fishman, *Solid State Commun.* **29**, 435 (1979).

[13] D. Ferrand, J. Cibert, A. Wasiela, C. Bourgognon, S. Tatarenko, G. Fishman, T. Andrearczyk, J. Jaroszyński, S. Koleśnik, T. Dietl, B. Barbara, D. Dufeu, *Phys. Rev. B* **63**, 085201 (2001).

[14] J. Gaj, W. Grieshaber, C. Bodin-Deshayes, J. Cibert, G. Feuillet, Y. Merle d'Aubigné, A. Wasiela, *Phys. Rev. B* **50**, 5512 (1994).

[15] Y. Shapira, S. Foner, D. Ridgley, K. Dwight, A. Wold, *Phys. Rev. B* **30**, 4021 (1984).

[16] J. Xia, W. Pan, C. Vicente, E. Adams, N. Sullivan, H. Stormer, D. Tsui, L. Pfeiffer, K. Baldwin, K. West, *Phys. Rev. Lett.* **93**, 176809 (2004).

[17] S. Datta, *Electronic Transport in Mesoscopic Systems*, Cambridge University Press, Cambridge, 2002.

[18] T. Ando, A. Fowler, F. Stern, *Rev. Mod. Phys.* **54**, 437 (1982).

[19] K. von Klitzing, G. Dorda, M. Pepper, *Phys. Rev. Lett.* **45**, 494 (1980).

[20] M. Herman, H. Sitter, *Molecular Beam Epitaxy: Fundamentals and current Status*, Springer, Berlin, 1996.

[21] R. Dingle, H. Störmer, A. Gossard, W. Wiegmann, *Appl. Phys. Lett.* **33**, 665 (1978).

[22] K. Novoselov, A. Geim, S. Morozov, D. Jiang, Y. Zhang, S. Dubonos, I. Grigorieva, A. Firsov, *Science* **306**, 666 (2004).

[23] J. Jaroszyński, T. Andrearczyk, G. Karczewski, J. Wróbel, T. Wojtowicz, E. Papis, E. Kamińska, A. Piotrowska, D. Popović, T. Dietl, *Phys. Rev. Lett.* **89**, 266802 (2002).

[24] H. Störmer, *Surf. Sci.* **132**, 519 (1983).

[25] A. Gold, *Phys. Rev. B* **38**, 10798 (1988).

[26] P. Coleridge, *Phys. Rev. B* **44**, 3793 (1991).

[27] S. Das Sarma, F. Stern, *Phys. Rev. B* **32**, 8442 (1985).

[28] P. Drude, *Annalen der Physik* **306**, 566 (1900).

[29] M. Tornow, *Magnetotransportuntersuchungen an periodisch strukturierten Elektronensystemen und Quantendrähten*, PhD thesis, MPI Festkörperforschung, Stuttgart, 1997.

[30] D. Tsui, H. Stormer, A. Gossard, *Phys. Rev. Lett.* **42**, 1559 (1982).

[31] S. Nelson, K. Ismail, J. Nocera, F. Fang, E. Mendez, J. Chu, B. Meyerson, *Appl. Phys. Lett.* **61**, 64 (1992).

[32] X. Du, I. Skachko, F. Duerr, A. Luican, E. Andrei, *Nature* **462**, 192 (2009).

[33] K. Bolotin, F. Ghahari, M. Shulman, H. Stormer, P. Kim, *Nature* **462**, 196 (2009).

[34] A. Tsukazaki, S. Akasaka, K. Nakahara, Y. Ohno, H. Ohno, D. Maryenko, A. Ohtomo, M. Kawasaki, *Nature Mater.* **9**, 889 (2010).

[35] O. Heinonen, *Composite Fermions: A Unified View of the Quantum Hall Regime*, World Scientific, Singapore, 1998.

[36] B. Piot, J. Kunc, M. Potemski, D. Maude, C. Betthausen, A. Vogl, D. Weiss, G. Karczewski, T. Wojtowicz, *Phys. Rev. B* **82**, 081307 (2010).

[37] C. Betthausen, P. Giudici, V. Kolkovsky, M. Wiater, G. Karczewski, B. Piot, J. Kunc, M. Potemski, T. Wojtowicz, D. Weiss, Fractional Quantum Hall Effect in $Cd_{1-x}Mn_xTe$: Composite Fermions in a Diluted Magnetic Semiconductor, in preparation, 2012.

[38] W. Pan, J. Xia, V. Shvarts, D. Adams, H. Stormer, D. Tsui, L. Pfeiffer, K. Baldwin, K. West, *Phys. Rev. Lett.* **83**, 3530 (1999).

[39] M. Stern, P. Plochocka, V. Umansky, D. Maude, M. Potemski, I. Bar-Joseph, *Phys. Rev. Lett.* **105**, 096801 (2010).

[40] M. Stern, B. Piot, Y. Vardi, V. Umansky, P. Plochocka, D. Maude, J. Bar-Joseph, *Phys. Rev. Lett.* **108**, 066810 (2012).

[41] L. Tiemann, G. Gamez, N. Kumada, K. Muraki, *Science* **335**, 828 (2012).

[42] R. Willett, L. Pfeiffer, K. West, *Proc. Natl. Acad. Sci. USA* **106**, 8853 (2009).

[43] R. Laughlin, *Phys. Rev. Lett.* **50**, 1395 (1983).

[44] F. Haldane, *Phys. Rev. Lett.* **51**, 605 (1983).

[45] B. Halperin, *Phys. Rev. Lett.* **52**, 1583 (1984).

[46] J. Jain, *Phys. Rev. Lett.* **63**, 199 (1989).

[47] A. Lopez, E. Fradkin, *Phys. Rev. B* **44**, 5246 (1991).

[48] B. Halperin, P. Lee, N. Nicholas, *Phys. Rev. B* **47**, 7312 (1993).

[49] T. Chakraborty, P. Pietiläinen, *The quantum Hall effects: Fractional and Integral*, Springer series in solid-state sciences, Springer, Berlin, 1995.

[50] Z. Ezawa, *Quantum Hall effects: Field theoretical approach and related topics*, World Scientific, Singapore, 2000.

[51] J. Jain, *Composite fermions*, Cambridge University Press, Cambridge, 2007.

[52] J. Eisenstein, H. Stormer, L. Pfeiffer, K. West, *Phys. Rev. Lett.* **62**, 1540 (1989).

[53] R. Du, A. Yeh, H. Stormer, D. Tsui, L. Pfeiffer, K. West, *Phys. Rev. Lett.* **75**, 3926 (1995).

[54] R. Du, A. Yeh, H. Stormer, D. Tsui, L. Pfeiffer, K. West, *Phys. Rev. B* **55**, R7351 (1997).

[55] R. Du, H. Stormer, D. Tsui, A. Yeh, L. Pfeiffer, K. West, *Phys. Rev. Lett.* **73**, 3274 (1994).

[56] J. Jaroszynski, T. Andrearczyk, G. Karczewski, J. Wrobel, T. Wojtowicz, E. Papis, E. Kaminska, A. Piotrowska, D. Popovic, T. Dietl, *Phys. Stat. Sol. B* **241**, 712 (2004).

[57] M. Wang, R. Campion, A. Rushforth, K. Edmonds, C. Foxon, B. Gallagher, *Appl. Phys. Lett.* **93**, 132103 (2008).

[58] E. De Poortere, E. Tutuc, S. Papadakis, M. Shayegan, *Science* **290**, 1546 (2000).

[59] F. Teran, M. Potemski, D. Maude, T. Andrearczyk, J. Jaroszynski, G. Karczewski, *Phys. Rev. Lett.* **88**, 186803 (2002).

[60] F. Teran, M. Potemski, D. Maude, Z. Wilamowski, A. Hassan, D. Plantier, J. Jaroszynski, T. Wojtowicz, G. Karczewski, *Physica E* **17**, 335 (2003).

[61] R. Winkler, J. Kotthaus, K. Ploog, *Phys. Rev. Lett.* **62**, 1177 (1989).

[62] R. Gerhardts, D. Weiss, K. v. Klitzing, *Phys. Rev. Lett.* **62**, 1173 (1989).

[63] C. Mitzkus, *Transportuntersuchungen an dichtemodulierten zweidimensionalen Elektronensystemen*, PhD thesis, University of Regensburg, 2005.

[64] P. Ye, D. Weiss, R. Gerhardts, M. Seeger, K. v. Klitzing, K. Eberl, H. Nickel, *Phys. Rev. Lett.* **74**, 3013 (1995).

[65] P. Beton, P. Main, M. Davison, M. Dellow, R. Taylor, E. Alves, L. Eaves, S. Beaumont, C. Wilkinson, *Phys. Rev. B* **42**, 9689 (1990).

[66] C. Beenakker, *Phys. Rev. Lett.* **62**, 2020 (1989).

[67] C. Zhang, R. Gerhardts, *Phys. Rev. B* **41**, 12850 (1990).

[68] D. Xue, G. Xiao, *Phys. Rev. B* **45**, 5986 (1992).

[69] F. Peeters, P. Vasilopoulos, *Phys. Rev. B* **47**, 1466 (1993).

[70] C. Albrecht, *Quantenmechanische Transporteffekte in kurzperiodischen lateralen Übergittern*, PhD thesis, MPI Festkörperforschung, Stuttgart, 2000.

[71] P. Beton, E. Alves, P. Main, L. Eaves, M. Dellow, M. Henini, O. Hughes, S. Beaumont, C. Wilkinson, *Phys. Rev. B* **42**, 9229 (1990).

[72] G. Karczewski, J. Jaroszynski, A. Barcz, M. Kutrowski, T. Wojtowicz, J. Kossut, *J. Cryst. Growth* **184/185**, 814 (1998).

[73] F. Bassani, S. Tatarenko, K. Saminadayar, N. Magnea, R. Cox, A. Tardot, C. Grattepain, *J. Appl. Phys.* **72**, 2927 (1992).

[74] F. Fischer, A. Waag, G. Bilger, T. Litz, S. Scholl, M. Schmitt, G. Landwehr, *J. Cryst. Growth* **141**, 93 (1994).

[75] S. Wei, S. Zhang, *Phys. Rev. B* **66**, 155211 (2002).

[76] N. Giles, J. Lee, T. Myers, Z. Yu, B. Wagner, R. Benz, C. Summers, *J. Electron. Mater.* **24**, 691 (1995).

[77] D. Ferrand, A. Wasiela, S. Tatarenko, J. Cibert, G. Richter, P. Grabs, G. Schmidt, L. Molenkamp, T. Dietl, *Solid State Commun.* **119**, 237 (2001).

[78] D. Awschalom, N. Samarth, *J. Magn. Magn. Mater.* **200**, 130 (1999).

[79] S. Crooker, D. Tulchinsky, J. Levy, D. Awschalom, R. Garcia, N. Samarth, *Phys. Rev. Lett.* **75**, 505 (1995).

[80] A. Gossard, R. Miller, W. Wiegmann, *Surf. Sci.* **174**, 131 (1986).

[81] T. Wojtowicz, M. Kutrowski, G. Cywinski, G. Karczewski, E. Janik, E. Dynowska, J. Kossut, R. Fiederling, A. Pfeuffer-Jeschke, W. Ossau, *J. Cryst. Growth* **184/185**, 936 (1998).

[82] T. Wojtowicz, M. Kutrowski, M. Surma, K. Kopalko, G. Karczewski, J. Kossut, M. Godlewski, P. Kossacki, Nguyen The Khoi, *Appl. Phys. Lett.* **68**, 3326 (1996).

[83] W. Menz, P. Bley, *Mikrosystemtechnnik für Ingenieure*, VCH, Weinheim, 1993.

[84] J. Vossen, W. Kern, *Thin film processes*, Academic Press, San Diego, 1978.

[85] D. Widmann, H. Mader, H. Friedrich, *Technologie hochintegrierter Schaltungen*, Springer, Berlin, 1996.

[86] J. Biberger, *Transportphänomene in mesoskopischen 2DEG-Strukturen unter dem Einfuss inhomogener Streufelder von Nanomagneten*, PhD thesis, University of Regensburg, 2007.

[87] M. Illing, G. Bacher, A. Forchel, A. Waag, T. Litz, G. Landwehr, *J. Cryst. Growth* **138**, 638 (1994).

[88] M. Foad, C. Wilson, C. Dunscomb, R. Williams, *Appl. Phys. Lett.* **60**, 2531 (1992).

[89] M. Foad, M. Watt, A. Smart, C. Sotomayro Torres, C. Wilkinson, W. Kuhn, H. Wagner, S. Bauer, H. Leiderer, W. Gebhardt, *Semicond. Sci. Technol.* **6**, A115 (1991).

[90] J. Lodermeyer, M. Multerer, M. Zistler, S. Jordan, H. Gores, W. Kipferl, E. Diaconu, M. Sperl, G. Bayreuther, *J. Electrochem. Soc.* **153**, C242 (2006).

[91] R. Popovic, *Solid State Electron.* **21**, 1133 (1978).

[92] V. Rideout, *Solid State Electron.* **18**, 541 (1975).

[93] W. Schottky, *Z. Phys.* **113**, 367 (1939).

[94] I. Dharmadasa, W. Herrenden-Harker, R. Williams, *Appl. Phys. Lett.* **48**, 1802 (1986).

[95] C. Mead, W. Spitzer, *Phys. Rev.* **134**, A713 (1964).

[96] J. Bardeen, *Phys. Rev.* **71**, 717 (1947).

[97] I. Dharmadasa, A. McLean, M. Patterson, R. Williams, *Semicond. Sci. Technol.* **2**, 404 (1987).

[98] Y. Wu, C. Becker, A. Waag, R. Schmiedl, S. Einfeldt, G. Landwehr, *J. Appl. Phys.* **73**, 7385 (1993).

[99] R. Braithwaite, C. Scott, J. Mullin, *Solid State Electron.* **23**, 1091 (1980).

[100] D. Brun-Le Cunff, B. Daudin, J. Rouvière, *Appl. Phys. Lett.* **69**, 514 (1996).

[101] C. Betthausen, *Transportexperimente an semimagnetischen CdMnTe/ CdMgTe-Heterostrukturen*, Diploma thesis, University of Regensburg, 2007.

[102] H. London, G. Clarke, E. Mendoza, *Phys. Rev.* **128**, 1992 (1962).

[103] C. Enns, S. Hunklinger, *Tieftemperaturphysik*, Springer, Berlin, 2000.

[104] F. Pobell, *Matter and Methods at Low Temperatures*, Springer, Berlin, 1996.

[105] Stanford Research Systems, About Lock-In Amplifers. Application Note #3, http://www.thinksrs.com.

[106] J. Scofield, *Am. J. Phys.* **62**, 129 (1994).

[107] H. Ott, *Noise Reduction Techniques in Electronic Systems*, Wiley, New York, 1988.

[108] F. Wellstood, C. Urbina, J. Clarke, *Phys. Rev. B* **49**, 5942 (1994).

[109] K. Wagner, *Transportuntersuchungen von Quanteninterferenzeffekten in ferromagnetischen (Ga,Mn)As Nanostrukturen*, PhD thesis, University of Regensburg, 2007.

[110] R. Clark, S. Haynes, A. Suckling, J. Mallett, P. Wright, J. Harris, C. Foxon, *Phys. Rev. Lett.* **62**, 1536 (1989).

[111] L. Engel, S. Hwang, T. Sajoto, D. Tsui, M. Shayegan, *Phys. Rev. B* **45**, 3418 (1992).

[112] W. Kang, J. Young, S. Hannahs, E. Palm, K. Campman, A. Gossard, *Phys. Rev. B* **56**, R12776 (1997).

[113] A. Davies, R. Newbury, M. Pepper, J. Frost, D. Ritchie, G. Jones, *Phys. Rev. B* **44**, 13128 (1991).

[114] K. Lai, W. Pan, D. Tsui, Y. Xie, *Phys. Rev. B* **69**, 125337 (2004).

[115] P. Coleridge, R. Stoner, R. Fletcher, *Phys. Rev. B* **39**, 1120 (1989).

[116] A. Usher, R. Nicholas, J. Harris, C. Foxon, *Phys. Rev. B* **41**, 1129 (1990).

[117] K. Park, J. Jain, *Phys. Rev. Lett.* **80**, 4237 (1998).

[118] D. Leadley, R. Nicholas, C. Foxon, J. Harris, *Phys. Rev. Lett.* **72**, 1906 (1994).

[119] F. Fischer, M. Grayson, *J. Appl. Phys.* **98**, 013710 (2005).

[120] W. Pan, H. Stormer, D. Tsui, L. Pfeiffer, K. Baldwin, K. West, *Phys. Rev. B* **61**, R5101 (2000).

[121] F. Zhang, S. Das Sarma, *Phys. Rev. B* **33**, 2903 (1986).

[122] R. Morf, N. d'Ambrumenil, S. Das Sarma, *Phys. Rev. B* **66**, 075408 (2002).

[123] C. Dean, B. Piot, P. Hayden, S. Das Sarma, G. Gervais, L. Pfeiffer, K. West, *Phys. Rev. Lett.* **100**, 146803 (2008).

[124] A. Wójs, J. Quinn, *Phys. Rev. B* **74**, 235319 (2006).

[125] K. Park, J. Jain, *Phys. Rev. Lett.* **81**, 4200 (1998).

[126] R. Du, H. Stormer, D. Tsui, L. Pfeiffer, K. West, *Phys. Rev. Lett.* **70**, 2944 (1993).

[127] A. Wójs, G. Möller, S. Simon, N. Cooper, *Phys. Rev. Lett.* **104**, 086801 (2010).

[128] S. Datta, B. Das, *Appl. Phys. Lett.* **56**, 665 (1990).

[129] J. Raabe, D. Weiss, V. Umanski, *Phys. B* **256-258**, 405 (1998).

[130] J. Schnakenberg, *Elektrodynamik*, Wiley, Weinheim, 2003.

[131] http://www.hsrc.hiroshima-u.ac.jp.

[132] H. Koo, J. Kwon, J. Eom, J. Chang, S. Han, M. Johnson, *Science* **325**, 1515 (2009).

[133] D. Wasik, K. Kudyk, M. Baj, J. Jaroszyński, G. Karczewski, T. Wojtowicz, A. Barcz, J. Kossut, *Phys. Rev. B* **59**, 12917 (1999).

[134] M. Born, V. Fock, *Z. Phys. A: Hadrons Nucl.* **51**, 165 (1928).

[135] http://www.en.wikipedia.org/wiki/Adiabatic_theorem.

[136] J. Rubbmark, M. Kash, M. Littman, D. Kleppner, *Phys. Rev. A* **23**, 3107 (1981).

[137] C. Zener, *Proc. R. Soc. London A* **137**, 696 (1932).

[138] M. Popp, D. Frustaglia, K. Richter, *Phys. Rev. B* **68**, 041303 (2003).

[139] B. Bernevig, J. Orenstein, S. Zhang, *Phys. Rev. Lett.* **97**, 236601 (2006).

[140] J. Koralek, C. Weber, J. Orenstein, B. Bernevig, S. Zhang, S. Mack, D. Awschalom, *Nature* **458**, 610 (2009).

[141] C. Betthausen, T. Dollinger, H. Saarikoski, V. Kolkovsky, G. Karczewski, T. Wojtowicz, K. Richter, D. Weiss, Spin transistor action via tunable Landau-Zener transitions, *Science*, accepted, 2012.

[142] R. Landauer, *IBM J. Res. Develop.* **1**, 223 (1957).

[143] M. Buttiker, Y. Imry, R. Landauer, S. Pinhas, *Phys. Rev. B* **31**, 6207 (1985).

[144] M. Wimmer, K. Richter, *J. Comput. Phys.* **228**, 8548 (2009).

[145] T. Ando, *Phys. Rev. B* **44**, 8017 (1991).

[146] J. Davis, P. Pechukas, *J. Chem. Phys.* **64**, 3129 (1975).

[147] P. Ye, *Electrons in a Periodic Magnetic Field*, PhD thesis, MPI Festkörperforschung, Stuttgart, 1996.

[148] C. Kittel, *Rev. Mod. Phys.* **21**, 541 (1949).

[149] M. König, A. Tschetschetkin, E. Hankiewicz, J. Sinova, V. Hock, V. Daumer, M. Schäfer, C. Becker, H. Buhmann, L. Molenkamp, *Phys. Rev. Lett.* **96**, 076804 (2006).

[150] T. Koga, Y. Sekine, J. Nitta, *Phys. Rev. B* **74**, 041302 (2006).

[151] M. Berry, *Proc. R. Soc. London A* **392**, 45 (1984).

[152] H. Koo, H. Yi, J. Ko, J. Chang, S. Han, D. Jung, S. Huh, J. Eom, *Appl. Phys. Lett.* **90**, 022101 (2007).

[153] S. Mangin, D. Ravelosona, J. Katine, M. Carey, B. Terris, E. Fullerton, *Nature Mat.* **5**, 210 (2006).

[154] H. Ohno, D. Chiba, F. Matsukura, T. Omiya, E. Abe, T. Dietl, Y. Ohno, K. Ohtani, *Nature* **408**, 944 (2000).

List of Publications

- B. Piot, J. Kunc, M. Potemski, D. Maude, C. Betthausen, A. Vogl, D. Weiss, G. Karczewski, T. Wojtowicz: **Fractional quantum Hall effect in CdTe.** *Phys. Rev. B* **82**, 081307 (2010).
- C. Betthausen, T. Dollinger, H. Saarikoski, V. Kolkovsky, G. Karczewski, T. Wojtowicz, K. Richter, D. Weiss: **Spin transistor action via tunable Landau-Zener transitions.** *Science*, accepted (2012).
- C. Betthausen, P. Giudici, V. Kolkovsky, M. Wiater, G. Karczewski, B. Piot, J. Kunc, M. Potemski, T. Wojtowicz, D. Weiss: **Fractional Quantum Hall Effect in $\mathbf{Cd_{1-x}Mn_xTe}$: Composite Fermions in a Diluted Magnetic Semiconductor.** *In preparation* (2012).

Acknowledgements

It is a pleasure to thank all the people who made this thesis possible. In particular, I would like to express my deep and sincere gratitude to...

My supervisor Prof. Dieter Weiss for giving me the opportunity to work on this extremely interesting topic. Thank you for your ongoing interest in my work, stimulating ideas at the right time and your generous funding.

Prof. Tomasz Wojtowicz who provided the high quality CdMnTe samples used in this PhD. Thank you for your patience in answering all my questions concerning growth, processing, contacts, etc.!

Prof. Klaus Richter, Dr. Henri Saarikoski and Tobias Dollinger for their interest in my experiments on magnetically modulated structures and for successfully developing a theoretical description. I am especially grateful to Henri and Tobias who explained all the ideas behind their model to me.

Prof. Arkadiusz Wójs for stimulating discussions concerning our FQHE measurements and an interesting lecture on the $\nu = 5/2$ state.

Dr. Paula Giudici who very much helped with experiments in the FQH regime and later data interpretation.

The secretaries of our chair, Claudia Rahm and Elke Haushalter for assisting in many different ways, in particular in case of any (annoying) paperwork.

Our technicians Cornelia Linz, Uli Gürster and Michael Weigl who helped with all problems inside and outside the cleanroom.

Dr. Henri Saarikoski, Dr. Paula Giudici, Silvia Minke, Andreas Rudolph and Christoph Preis for proofreading the manuscript.

My parents who supported me in any kind of situation throughout my entire education.

My wife Anita for her understanding and patience.